FUNDAMENTAL UNDERSTANDING OF SCRATCH AND MAR BEHAVIOR OF POLYMERS

A Dissertation

by

MAROUEN HAMDI

Submitted to the Office of Graduate and Professional Studies of
Texas A&M University
in partial fulfillment of the requirements for the degree of

DOCTOR OF PHILOSOPHY

Chair of Committee,	Hung-Jue Sue
Committee Members,	Harry A. Hogan
	Steve Suh
	Joshua Yuan
Head of Department,	Andreas A. Polycarpou

December 2016

Major Subject: Mechanical Engineering

ABSTRACT

Scratch behavior on polymeric films was investigated. The effect of film orientation and architecture on scratch resistance was determined. Film orientation was obtained by uniaxial stretching and its architecture was modified by the addition of ethylene comonomers. Model polypropylene (PP) and polyamide (PA) systems were employed to study the effect of laminate structure on scratch resistance. Also, mar behavior on bulk polymeric materials was investigated. The impact of brightness, transparency, and color as well as surface friction and texture on mar visibility resistance was determined. These studies were conducted based on fundamental, experimental, numerical, psychophysical, and statistical approaches. Experimental tests were conducted with accordance to ASTM/ISO standard. They were complemented by numerical simulations performed using a sophisticated FEM model. The psychophysical approach is performed through human observation tests to validate the experimental findings. The obtained data was analyzed using multidimensional scaling (MDS) statistical approach.

Scratch analysis demonstrates that scratch resistance is improved with higher film orientation and lower ethylene content. The FEM analysis shows that this improvement is associated with surface-to-interface shift of stress concentration. It is also found using the parametric analysis that scratch resistance is mainly improved due to higher film hardening coefficient and yield stress, but is insensitive to film modulus. It is also found that PP/PA has better scratch performance than PA/PP. This is mainly due to PP/PA low surface friction and graded structure, where upper PP layer absorbs scratch energy and lower PA layer protects the interface from high stress built-up. Mar analysis demonstrates that mar visibility resistance decreases with green, dark, smooth, and high-friction surfaces. Also, MDS results show that brightness, transparency, and color have respectively considerable, moderate, and insignificant effect on mar perception. Experimental findings indicate that mar visibility resistance can be quantified using the slope variation of mar contrast curve. FEM stress analysis shows that stress concentration is generated at the mar edge, then propagates towards inner mar area repetitively, reflecting stick-slip oscillations observed in experimental mar tests.

The results found in these research studies serve as a practical tool to effectively design polymeric systems with appealing scratch and mar performance.

DEDICATION

To my father who made tremendous sacrifices

To my mother who, unconditionally, loves and prays

ACKNOWLEDGEMENTS

I would like to deeply thank my committee chair, Professor Hung-Jue Sue, for giving me the opportunity to be a member of his research group. I am grateful for his overwhelming encouragement, guidance, and support. Also, I would like to thank my committee members, Prof. Harry A. Hogan, Prof. Steve Suh, and Prof. Joshua Yuan.

I also acknowledge the financial contribution of Texas A&M Scratch Behavior Consortium members, the assistance of Texas A&M Supercomputing Facility, and the technical support of Surface Machine System team. I thank SABIC, Advanced Composites, and Japan Polypropylene companies for generously providing the model systems needed for our experimental studies. Particularly, I am sincerely thankful to Dr. Drew Manica for his constructive discussions and continuous support that made him not just a coworker but also a friend.

I want to recognize the assistance of my friends and colleagues at the Polymer Technology Center who made my journey a fulfilling learning and life experience. Also, I deeply thank my community in Bryan/College Station, all the strangers I have come to call family, for making me thrive to become a better person.

Finally, and most importantly, I want to express my deepest gratitude to my parents. To my father, Mokhtar, and my mother, Souad, the farmers who made tremendous sacrifices so my siblings and I could become the accomplished and successful human beings that we are.

NOMENCLATURE

ATR	Attenuated Total Reflectance
ASV	Automated Scratch Visibility [software]
COF	Coefficient of Friction
CPU	Central Processing Unit
DGF	Density Graded Foams
E	Young's modulus
FEM	Finite Element Method
FTIR	Fourier-Transform Infrared
GM	Graded Materials
h	Hardening slope
INDSCAL	Individual Differences Scaling
L	Applied Load
MD	Machine Direction
MDS	Multidimensional Scaling
PA	Polyamide
PC	Polycarbonate
PP	Polypropylene
$r_{optimal}$	Optimal exponent
s	Softening slope
SCOF	Scratch Coefficient of Friction

TD	Transverse Direction
VLSCM	Violet Laser Scanning Confocal Microscope
w	MDS weight
ν	Poisson's ratio
ρ	Density
μ	Friction
σ_y	Yield stress
σ_F	Frictional stress
σ_N^T	Tensile stress
σ_{pp}^{max}	Maximum principal stress
ε	Strain
ε_{pp}^{max}	Maximum principal plastic strain
ε_{avr}^{max}	Average maximum principal plastic strain

TABLE OF CONTENTS

Page

ABSTRACT ii

DEDICATION iv

ACKNOWLEDGEMENTS v

NOMENCLATURE vi

LIST OF FIGURES xi

LIST OF TABLES xvi

CHAPTER I INTRODUCTION 1
- I.1. Background 1
- I.2. Research Significance and Objectives 3
- I.3. Report Layout 4

CHAPTER II LITERATURE REVIEW AND RESEARCH STRATEGY 5
- II.1. Literature Review 5
  - II.1.1. Scratch Standard and FEM Model 5
    - II.1.1.1. ASTM/ISO scratch standard 5
    - II.1.1.2. FEM model 6
  - II.1.2. Key Findings 9
    - II.1.2.1. Analysis of scratch behavior 9
    - II.1.2.2. Analysis of mar behavior 14
    - II.1.2.3. Scratch and mar visibility resistance 17
- II.2. Research Strategy 18

CHAPTER III SCRATCH BEHAVIOR ON POLYMERIC FILMS 20
- III.1. Experimental 21
  - III.1.1. Model Systems 21
  - III.1.2. Measurements of Film Properties 21

III.1.3. Characterization of the Mechanical Properties 23
III.2. FEM Modeling 23
III.3. Results and Discussion 24
III.3.1. Characterization of the Model Systems 24
III.3.2. Scratch Resistance 28
III.3.2.1. Effect of film orientation 31
III.3.2.2. Comparison between MD and TD 31
III.3.2.3. Effect of ethylene content 34
III.3.3. FEM Parametric Analysis 35
III.3.3.1. Constitutive parameters 35
III.3.3.2. Effect of film modulus 37
III.3.3.3. Effect of film yield stress 40
III.3.3.4. Effect of film strain hardening 43
III.4. Conclusions 45

CHAPTER IV SCRATCH BEHAVIOR ON POLYMERIC LAMINATES 47
IV.1. Experimental 48
IV.2. FEM Modeling 48
IV.3. Results and Discussion 49
IV.3.1. Surface and Subsurface Analysis 49
IV.3.1.1. Surface analysis 49
IV.3.1.2. Subsurface analysis 55
IV.3.2. Graded Materials (GMs) 60
IV.3.2.1. Background and case study 60
IV.3.2.2. Elastically GMs 62
IV.3.2.3. Plastically GMs 64
IV.3.2.4. Density-graded foams (DGFs) 65
IV.3.3. FEM Modeling 65
IV.3.3.1. Stress analysis near surface 66
IV.3.3.2. Subsurface analysis 70
IV.4. Conclusion 76

CHAPTER V EFFECT OF PERCEPTUAL PROPERTIES ON MAR RESISTANCE . 78
V.1. Experimental 78
V.2. Psychophysical 81
V.2.1. Subjects 81
V.2.2. Test Condition 81
V.2.3. Pairwise Comparison Test 82
V.2.4. Software 83
V.3. Results and Discussion 83
V.3.1. Optimal Minkowski Exponent 83
V.3.2. Shepard Diagram 85

V.3.3. Scree Plot ... 86
V.3.4. Overall Weights of MDS Dimensions ... 87
V.3.5. Subject Spaces ... 88
V.3.6. MDS Space Representation ... 90
V.3.7. Dimensions ... 91
V.3.7.1. First dimension ... 92
V.3.7.2. Second dimension ... 93
V.3.7.3. Third dimension ... 94
V.4. Conclusion ... 95

CHAPTER VI EXPERIMENTAL AND FEM ANALYSIS OF MAR BEHAVIOR ... 97
VI.1. Experimental ... 97
VI.1.1. Model Systems ... 97
VI.1.2. Mar Visualization ... 98
VI.1.3. FTIR-ATR Characterization ... 99
VI.2. Results and Discussion ... 99
VI.2.1. Consistency of the New Method ... 99
VI.2.2. Slip Agent Effect ... 100
VI.2.2.1. Surface composition ... 102
VI.2.2.2. Frictional behavior ... 103
VI.2.3. Proposed Parameter for Mar Visibility Quantification ... 106
VI.2.4. Texture Effect ... 107
VI.3. FEM Analysis ... 109
VI.3.1. FEM Model ... 109
VI.3.2. Constitutive Parameters ... 111
VI.3.3. Conversion Analysis ... 111
VI.3.4. Stress Analysis ... 114
VI.3.5. Parametric Analysis ... 115
VI.3.5.1. Effect of COF on mar behavior ... 115
VI.3.5.2. Effect of Young’s modulus on mar behavior ... 117
VI.3.5.3. Effect of yield stress on mar behavior ... 118
VI.3.5.4. Effect of hardening slope on mar behavior ... 119
VI.3.5.5. Effect of softening slope on mar behavior ... 119
VI.4. Conclusion ... 120

CHAPTER VII CONCLUSIONS AND FUTURE RESEARCH PLANS ... 122
VII.1. Summary of the Present Research ... 122
VII.1.1. Scratch Behavior on Polymeric Films and Laminates ... 122
VII.1.2. Mar Behavior on Polymeric Materials ... 123
VII.2. Future Research Directions ... 125
VII.2.1. FEM Model ... 125
VII.2.2. Scratch Behavior on Polymeric Laminates ... 125

    VII.2.3. Mar Behavior on Polymeric Films and Laminates 126
    VII.2.4. Towards a Standardized Mar Test 126

REFERENCES 127

APPENDIX THEORETICAL BACKGROUND OF MDS 150
  A.1. Introduction 150
  A.2. Basic Concepts 150
    A.2.1. MDS Space 150
    A.2.2. Metric and Ordinal MDS 151
    A.2.3. Stress Function 151
    A.2.4. Dimensionality and Scree Plots 152
    A.2.5. Minkowski R-Metrics 153
    A.2.6. Weighted Euclidean Model 153

LIST OF FIGURES

Page

Figure II-1. The FEM model and its boundary conditions are shown [45]........................7

Figure II-2. Features of scratch damage on TPO sample (a) transition from whitening to fish-scaling (b) developed fish-scaling (c) material removal [41]. 9

Figure II-3. SEM micrographs of well-developed crack (high resolution on the right) for a) nano-sized ASA system, b) nano-sized ABS system, and c) micron-sized ASA system. (Scratch direction: from left to right) [46].........11

Figure II-4. Maximum principal stress field at normal load of 45 N (top view) for (left) acrylic–steel and (right) polyurethane–polypropylene coating systems [9]..13

Figure II-5. Elcometer 1730 Car Wash Simulator. 14

Figure II-6. Scratch transitions showing pre-scratch mar damage [34]. 15

Figure II-7. Correlation between mar resistance and SCOF [58]...................................16

Figure II-8. Flow chart of the research strategy. 19

Figure III-1. Modeled film-backing structure and refined mesh in the scratch area........24

Figure III-2. Effect of the ethylene content on the constitutive behavior of films with (a) 4x (b) 5x and (c) 6x stretch ratios...29

Figure III-3. Orientation effect on the constitutive behavior of (a) PP (b) P3E and (c) P5E films. 29

Figure III-4. Resistance of the films to (a) whitening and (b) puncture damages in MD..31

Figure III-5. Scratch resistance of the model systems in TD. 33

Figure III-6. Difference in scratch resistance between MD and TD in terms of film orientation. 34

Figure III-7. Constitutive parameters considered in the FEM parametric analysis. 36

Figure III-8. Scratch depth (D) and height (H) obtained using the FEM model.............37

Figure III-9. Effect of film tensile modulus on scratch height (H) and depth (D). 38

Figure III-10. Longitudinal (upper) and top (bottom) views of von Mises stress distribution (in Pa) beneath the scratch tip for the examined moduli values (L=16 N). 39

Figure III-11. Effect of film yield stress on scratch height (H) and depth (D). 40

Figure III-12. Longitudinal (upper) and top (bottom) views of von Mises stress distribution (in Pa) beneath the scratch tip for examined yield stress values (L=16 N). 41

Figure III-13. Zoomed area A for a yield stress of (a) 30 MPa and (b) 70 MPa. 42

Figure III-14. Effect of film strain hardening slope on scratch height (H) and depth (D) 43

Figure III-15. Longitudinal (upper) and top (bottom) views of von Mises stress distribution (in Pa) beneath the scratch tip for different hardening slope values (L=16N). 44

Figure IV-1. Typical piecewise linear stress–strain curve used for FEM modeling [9] 49

Figure IV-2. COF measurements of PA and PP surfaces. 50

Figure IV-3. Scratch features on (a) PA [L=30 N] (b) PP [L=30 N] (c) PA/PP [L=30 N] (d) PP/PA [L=30 N] (e) PP/PA [L=70 N]. 52

Figure IV-4. Stick-slip and tearing onset loads of the studied films and laminates. 54

Figure IV-5. SCOF of (a) PA and PA/PP (b) PP and PP/PA (c) PA/PP and PP/PA [L=30N]. 56

Figure IV-6. Transitional region of PP film: (a) surface section (b) corresponding longitudinal subsurface section (b-1) and (b-2) zoomed subsurface sections. 57

Figure IV-7. (a) Transitional region on PA/PP (b) Stick-slip region on PA/PP (c) Transitional region on PP/PA (d) Stick-slip region on PP/PA. 58

Figure IV-8. (a) Transitional region on PA/PP (b) Stick-slip region on PA/PP (c) Transitional region on PP/PA (d) Stick-slip region on PP/PA (e) Tearing region on PP/PA. 59

Figure IV-9. Cross-section images of the transitional region on (a) PA/PP (b) PP/PA....60

Figure IV-10. Gradients in the graded structure of PP/PA laminate on Al backing.......62

Figure IV-11. Peak frictional (σF) and tensile normal (σNT) stress values of (blue) PA/PP and (red) PP/PA laminates (a) on the surface and (b) at the laminate-backing interface....66

Figure IV-12. Scratch width (W), height (H), and depth (D) on PA/PP (red) and PP/PA (blue) laminates....68

Figure IV-13. (a) εppmax (b) σppmax and (c) σN distributions on the surface of PA/PP and PP/PA laminates (L=15 N)....69

Figure IV-14. von Mises stress beneath the scratch tip (a) PA/PP [L = 7 N] (b) PP/PA [L = 7 N] (c) PA/PP [L = 15 N] (d) PP/PA [L = 15 N] (e) PA/PP [L = 15 N] (f) PP/PA [L = 15 N]....72

Figure IV-15. von Mises stress distribution beneath the scratch tip on (a) PP [L = 7 N] (b) PP/PA [L = 7 N] (c) PP [L = 12 N] (d) PP/PA [L = 12 N]....74

Figure IV-16. σppmax distribution at the laminate-backing interface (L=15 N)....75

Figure IV-17. Top view of interlayer σppmax distribution beneath the scratch tip (L=15 N)....75

Figure V-1. Red and transparency model systems used for the present study....79

Figure V-2. UV-Vis transmittance spectra of transparency samples....80

Figure V-3. Experimental conditions for mar MDS psychophysical test....82

Figure V-4. The change in Kruskal stress over Minkowski exponent for two-to-six dimensional spaces....84

Figure V-5. A representative empirical Shepard diagram....86

Figure V-6. (a) Typical and (b) Empirical scree plots....87

Figure V-7. Subject space of two-dimensional MDS configuration....89

Figure V-8. Subject space of three-dimensional MDS configuration....90

Figure V-9. MDS spaces obtained using INDSCAL weighted Euclidian distance model (a) Two-dimensional (b) Three-dimensional....91

Figure VI-1. Schematic of the standardized light box used for scratch and mar observation..98

Figure VI-2. Mar visibility onset load of some model systems, comparison of psychophysical test with new and conventional methodologies. 100

Figure VI-3. Mar visibility onset load of colored samples (a) neat and (b) modified. 101

Figure VI-4. Mean contrast curves of mar damage on neat (dashed) and modified (continuous) samples. The color of the curve reflects the color of the sample. 102

Figure VI-5. Infrared spectra of (a) neat samples, (b) modified samples, and (c) damaged modified samples on the end of the mar region.........................104

Figure VI-6. (a) Typical patterns of mar test loads on neat and modified surfaces: (blue) normal (red) tangential. (b) LSCM of mar damage features on neat sample at 5 mm, 40 mm, and 75 mm locations. White and yellow arrows refer to microcracks and periodic stick-slip patterns, respectively. 105

Figure VI-7. (a) Mean contrast curves of mar damage on smooth (continuous) and textured (dashed) surfaces in Systems A (red) and System B (blue). (b) Representative mar images...108

Figure VI-8. FEM model...110

Figure VI-9. (a) Mesh A (b) Mesh E...112

Figure VI-10. Scratch depth profiles and CPU time for meshes A – E at the end of the mar process. 113

Figure VI-11. Mar-induced σppmax at mar loads of (a) 20 N (b) 33.33 N (c) 40 N (d) 46.66 N (e) 80 N (g) 100 N. Tip position and test direction are indicated by black and yellow arrows, respectively. 115

Figure VI-12. von Mises stress distribution (a) longitudinal view [L=67 N] (b) surface view [L=100 N]..116

Figure VI-13. Effect of surface COF on (a) εppmax (b) εavrmax [L = 100 N]. 117

Figure VI-14. Effect of Young’s modulus on (a) εppmax (b) εavrmax [L = 100 N]. 118

Figure VI-15. Effect of yield stress on (a) εppmax (b) εavrmax [L = 100 N].............118

Figure VI-16. Effect of strain hardening slope on (a) εppmax (b) εavrmax [L = 100 N]. 119

Figure VI-17. Effect of softening slope on (a) εppmax (b) εavrmax [L = 100 N]. 120

LIST OF TABLES

Page

Table III-1. Model systems used in the study. 26

Table III-2. Tensile and physical properties of the modeled aluminum and PP 26

Table III-3. Thickness, roughness, and COF of the model systems.................................27

Table III-4. Mechanical properties measurements provided by the suppliers. 28

Table IV-1. Constitutive parameters introduced to the FEM model................................49

Table V-1. Optimal Minkowski exponent and Kruskal stress values per dimension $\boldsymbol{m}$..85

Table V-2. Overall dimensions weights in two and three-dimensional MDS spaces. 88

Table VI-1 $\Delta Slope\ in\ (kN)-1$ of neat and modified samples. 107

Table VI-2. Constitutive parameters introduced in the FEM model.............................111

Table VI-3. Mesh designs considered for the convergence study.................................112

CHAPTER I

INTRODUCTION

I.1.BACKGROUND

Polymeric materials are known for the versatility of their composition and the adjustability of their structure. Their properties can be tailored to design products with unique functionalities such as toughness and weatherability. They are also known to have good aesthetic properties. Their perceptual attributes, such as brightness, transparency, and color can be easily modified. This makes them extensively used in a wide range of industries such as automotive, packaging, electronics, and optics [1, 2]. However, their aesthetic and functional properties can be considerably affected by different surface damages. Particularly, scratch is one of the most commonly encountered mechanical damages on polymeric surfaces [3-5]. This created an urgent need to quantify and improve the scratch resistance of these materials. As will be presented in the literature review, extensive studies were conducted to investigate the scratch performance of polymeric materials using fundamental, experimental, and numerical methods. The majority of these studies were performed on bulk polymeric systems. Other few studies focused on polymeric coatings mainly to determine their adhesion and delamination resistance [6-9]. However, little has been done to examine the intrinsic scratch behavior of free-standing polymeric films and laminates.

Polymeric films are widely used in a variety of applications ranging from automotive, household goods, furniture, and packaging [10, 11]. This is due to their good overall physical and mechanical properties, recyclability, and low cost. In particular, the characteristic properties of different films can be combined in the form of polymeric laminates to achieve high value-added applications and meet specific industrial requirements. For instance, polymeric laminates serve as packaging materials due to their efficient barrier properties [12]. In electronics, they are utilized to make capacitor films [13], polyelectrolyte multilayers (PEMs), and polymer light emitting diodes (PLEDs) [14]. In the biomedical industry, they are used to produce biodegradable polymeric multilayer capsules (PMLCs) for drug delivery [15], functionalized biomaterials [16], and antimicrobial packaging to target particular microorganisms and control microbial contamination [17]. Thanks to their good optical properties, they are utilized as anti-reflective coatings [18], backlighting illumination structures [19], and multilayered microspheres with radial refractive index variation [20]. Also, they can be used for other industrial applications such as flame retardants [21], sound absorbents [22], solar energy protector [23], photonic devices [24], and labels [25]. However, for many of these applications, the scratch resistance of polymeric films and laminates is still deficient [26]. Despite their extensive use, and their high susceptibility to scratch damage, limited efforts have been dedicated to study scratch behavior on polymeric films and laminates.

Mar is another surface damage with a significant impact on the aesthetic properties of polymeric products. For instance, it affects the high optical quality of clear-coated surfaces frequently utilized in different automotive components. Up to recently, the terms “scratch” and mar” were exchanged carelessly in some studies as if they refer to the same damage [27]. However, scratch consists in medium to severe damage, while mar refers to shallow and faint surface damage [28, 29]. In many studies, automated car washing is considered as the “*standard source”* of mar damage [28, 30-32]. Yet this damage can be encountered in many other fields where the applied stress is low such as packaging, label, and polishing industries. Mar behavior has been rarely investigated in the literature. It was examined in previous studies as a subtle pre-scratch damage [33, 34]. However, its sensitivity to both low stress and surface properties makes the study of this faint damage more complex and challenging than scratch. Therefore, it should be investigated separately to obtain more consistent results.

I.2.RESEARCH SIGNIFICANCE AND OBJECTIVES

Mar and scratch performances are one of the most important criteria for many polymeric products. As highlighted above, the studies conducted on scratch behavior were extensive on bulk materials but limited on films and laminates. Therefore, characterizing scratch behavior on these systems frequently employed in the industry has significant advantages. Also, due to the rising expectations of consumers and the increasing use of colored surfaces, more and more attention is dedicated to mar which affects significantly the aesthetic properties [32]. This subtle damage is highly under-investigated because of its complex behavior. Therefore, characterizing its performance has considerable impact on many industrial applications. The ultimate objective of this research endeavor is to contribute to the understanding of scratch and mar behavior on polymers. This facilitates the design of polymers with better scratch and mar resistance.

I.3.REPORT LAYOUT

Chapter II presents a review of the previous studies conducted on scratch and mar damages on polymeric systems: ASTM/ISO scratch standard and FEM model employed in these studies are first presented, followed by a discussion of the key findings. The same experimental standard and numerical model were also employed in our studies. Then, the strategy followed in this research endeavor is highlighted after the literature review.

The studies dedicated to understand scratch behavior on polymeric films and laminates are presented in Chapter III and IV. In Chapter III, we investigate the effects of molecular architecture, modified through the incorporation of ethylene comonomer, and orientation, modified through uniaxial stretching, on the scratch resistance of polypropylene-based model films. In Chapter IV, we examine the scratch behavior of polymeric laminates with different structural, surface, and mechanical properties.

Chapter V and VI focus on mar behavior on bulk polymeric materials. In Chapter V, the effect of the major surface perceptual properties, namely brightness, transparency, and color on mar visibility resistance is investigated. In Chapter VI, we determine the impact of surface friction and texture on mar behavior. Surface friction was modified by adding fatty amide slip agent, and texture effect is studied by comparing mar on smooth and textured samples. For more mechanistic characterization, an FEM stress analysis of mar damage is also presented in this chapter.

The last chapter summarizes the major findings and discusses new research avenues and approaches to gain better insights on scratch and mar behavior on polymers.

CHAPTER II

LITERATURE REVIEW AND RESEARCH STRATEGY

In this chapter, the extensive studies conducted to qualitatively and quantitatively characterize scratch and mar behavior on polymeric systems are reviewed. The frequently employed scratch standard and FEM model are highlighted, and the key findings are discussed. Then, the research strategy and methodologies are presented.

II.1.LITERATURE REVIEW

II.1.1.Scratch Standard and FEM Model

II.1.1.1.ASTM/ISO scratch standard

Scratch behavior was previously studied using nanoindentation test [35]. However, this test is not realistic enough to simulate most scratch damages in real case scenarios. Other studies investigated scratch behavior on a macroscopic scale by applying a constant scratch load. For example, five-finger scratch test based on Ford lab method is accepted by many industrial companies especially in the automotive field [36]. However, this test does not accurately determine the load value associated with scratch resistance and provides a load range instead.

For more consistent analysis, a standardized scratch test, namely ASTM D7027-05/ISO 19252:08 standard, was defined [37, 38]. This test is frequently employed in academic and industrial applications [39, 40]. It consists in applying a linearly increasing load [40] using a custom-built scratch machine shown in [39]. The applied scratch load should be high enough to obtain different scratch transitions. Also, it can be modified depending on the test parameters and the examined model systems. The scratch distance and speed are usually equal to 100 mm and 100 mm/s. This speed is recommended to simulate abrupt and rapid scratch damages created on car coatings by sharp tools (knife, key ...). Yet it can be changed depending on the studied application. The most commonly used scratch tip consists in a spherical stainless steel tip with a diameter of 1 mm. Before conducting scratch tests, the samples are cleaned with air pressure to preserve their surface quality. Also, several tests are carried out on each system for more normalized results.

Previous studies employed high-resolution KEYENCE VK-9700K violet laser scanning confocal microscope (VLSCM) to visualize scratch and mar deformation features [40]. The microscope has a height resolution of ~1 nm, and a laser wavelength of 408 nm. The optical images can be obtained using VK Analyzer software provided with the microscope. Before each observation, it is crucial to confirm the absence of artifacts and verify the smoothness of the samples. In the case of thin polymeric films, sectioned film samples were first placed in a sample holder and secured in epoxy, followed by room temperature curing for 24 h. To achieve the 0.4 μm average smoothness required for VLSCM observation, the samples were polished using a sandpaper and a solution of 0.3 μm alumina oxide on a nylon cloth [41, 42]. The same experimental tests described in this section have been performed in our research analysis.

II.1.1.2.FEM model

To gain a more mechanistic understanding of scratch behavior, FEM analysis was previously conducted using the commercial finite element package ABAQUS® [9, 40, 43, 44]. Figure II-1 shows the dimensions and boundary conditions of the FEM model [44]. The computational time was significantly reduced by considering the model y-z plane and simulating only half of the model (x < 0). Also, the clamping boundary condition at the boundaries (y = 0) and (y = 20) were simulated by restraining the nodes in all directions. The rigid substrate (z = 0) and the symmetry plane (x = 0) were simulated by preventing the model translation in z and x directions, respectively. Also, the scratch tip was modeled as a rigid spherical body with a diameter of 1 mm.

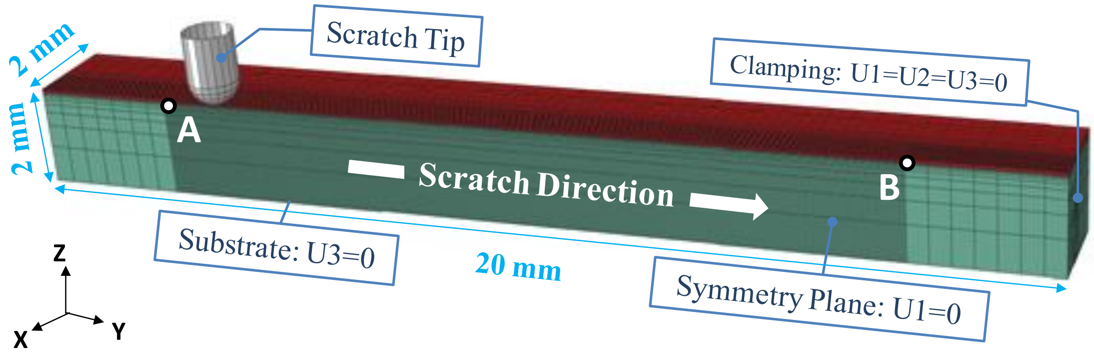

Figure II-1. The FEM model and its boundary conditions are shown. Reprinted from Tribology International, 103, Hamdi, M., M. Puopolo, H. Pham, and H.-J. Sue, Experimental and FEM analysis of scratch behavior on polypropylene thin films: Effect of film orientation and ethylene monomer content, 412–422. Copyright (2016), with permission from Elsevier [44].

With regards to the model meshing, eight-node 3D linear brick elements (C3D8R) with three nodal displacement degrees of freedom and reduced integration were considered. These elements were chosen because they do not have the inherent contact problems of quadratic elements [43]. Also, they show a faster convergence than the tetrahedral elements with respect to mesh refinement. For a better computational performance, a refined mesh was employed near the contact area. It would be computationally expensive to use this fine mesh for the entire specimen. Therefore, fine meshes were considered only beneath the scratch tip across a critical distance between point A and point B as shown in Figure II-1. The total number of nodes across this distance is usually 512. Preliminary simulations showed that this number is sufficient to obtain consistent and accurate results. Also, dynamic stress analysis and adaptive remeshing provided by ABAQUS were considered in all previous studies to preserve the mesh quality and avoid excessive distortion of the elements [43].

Using this FEM model, scratch tests were modeled in all studies with accordance to the ASTM/ISO standard described previously [37, 38]. Because only half of the model is simulated, the modeled load is always half of that applied experimentally [9, 40]. Three major steps were considered in the FEM model to simulate the experimental scratch test: The first step is the indention test where the rigid tip moves down with an applied load of 0.5 N and maintains contact with the surface of the modeled system. Then the scratch process takes place and the tip slides with a linearly increasing load. The scratch distance and speed are usually 12 mm and 10 m/s, respectively. Finally, the tip stops at the scratch end and moves upward allowing for material elastic recovery. For simplification purposes, elements separation and removal after damage, heat generation, and time-dependent response were not considered in all the reviewed FEM studies. This FEM was modified and employed in our studies for numerical simulation.

II.1.2.Key Findings

II.1.2.1.Analysis of scratch behavior

As the applied scratch load increases, different scratch features appear on the studied polymeric systems [40]. Depending on the material properties and test conditions, these features can be either brittle such as *cracking* and *crazing* damages, or ductile such as *ironing* and *fish-scaling* damages [40]. For instance, in Figure II-2, whitening damage appears at low applied loads. This damage is caused by either the increase in surface roughness or the formation of light scattering centers, such as voiding, cracking, crazing, etc. At higher scratch loads, fish-scaling damage appears in the form of periodic concave features pointing toward the scratch direction. Figure II-2a shows the transition from whitening to fish-scaling damage, while Figure II-2b presents developed fish-scaling patterns. Finally, at sufficiently high scratch loads, plowing damage takes place and the material is removed from the surface of the sample.

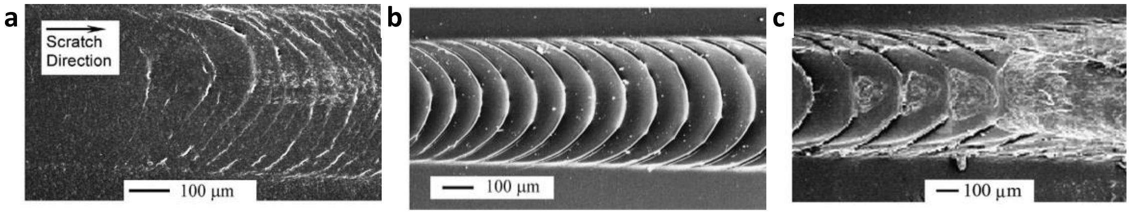

Figure II-2. Features of scratch damage on TPO sample (a) transition from whitening to fish-scaling (b) developed fish-scaling (c) material removal. Reprinted from Polymer, 50/16, Jiang, H., R. Browning, and H.-J. Sue, Understanding of scratch-induced damage mechanisms in polymers, 4056-4065. Copyright (2009), with permission from Elsevier [40].

Previous studies investigated the impact of different parameters on the scratch behavior of polymeric systems. The impact of additives and fillers on scratch features was investigated [45-48]. It found that talc fillers have benign effects on the mechanical properties of polymeric matrix, but they decrease its scratch resistance [48]. This limitation was overcome by treating the talc-modified surfaces or adding slip agents to the blend [47]. Slip agents are polymer additives derived from fatty acids. The thermo-mechanical properties of these molecules allow them to migrate toward the surface during the blending process and form a waxy thin layer. One of the major purposes of this process, known as *blooming*, is to decrease the surface COF. As a result, scratch resistance is significantly improved and scratch features are eliminated or at least delayed [46]. Another study investigated the effect of the size and type of reinforcing rubber particles [45]. Results show that micron-sized rubber particles lead to better scratch resistance compared to nano-sized particles. Figure II-3 presents the crack damage formed on the scratch path of polymers with micron and nano-sized rubber particles. It is shown that the severe mico-cracks obtained in the case of nano-particles (Figure II-3a and Figure II-3b) are considerably suppressed in the case of micron-particles (Figure II-3c). This change in cracking patterns is caused by the change in fracture modes after the addition of particles with different sizes.

The effect of other parameters on the scratch resistance of polymers was also determined. Jiang et al. showed that scratch resistance is improved with higher surface roughness [49]. It is also demonstrated that better scratch resistance is obtained with higher molecular weight and higher surface crystallinity [26, 50]. The impact of other parameters such as testing rate [51] and humidity [52] was also determined. Results show that, when the mechanical testing rate increases, soft polymer systems behave more rigidly and experience significant mechanical embrittlement [51]. Also, during the first few days in a humid environment, moisture exposure causes plasticization and scratch resistance decreases, leading to weaker surface. When saturation is reached, water molecules gather on the surface to impart a degree of lubrication improving scratch resistance [52].

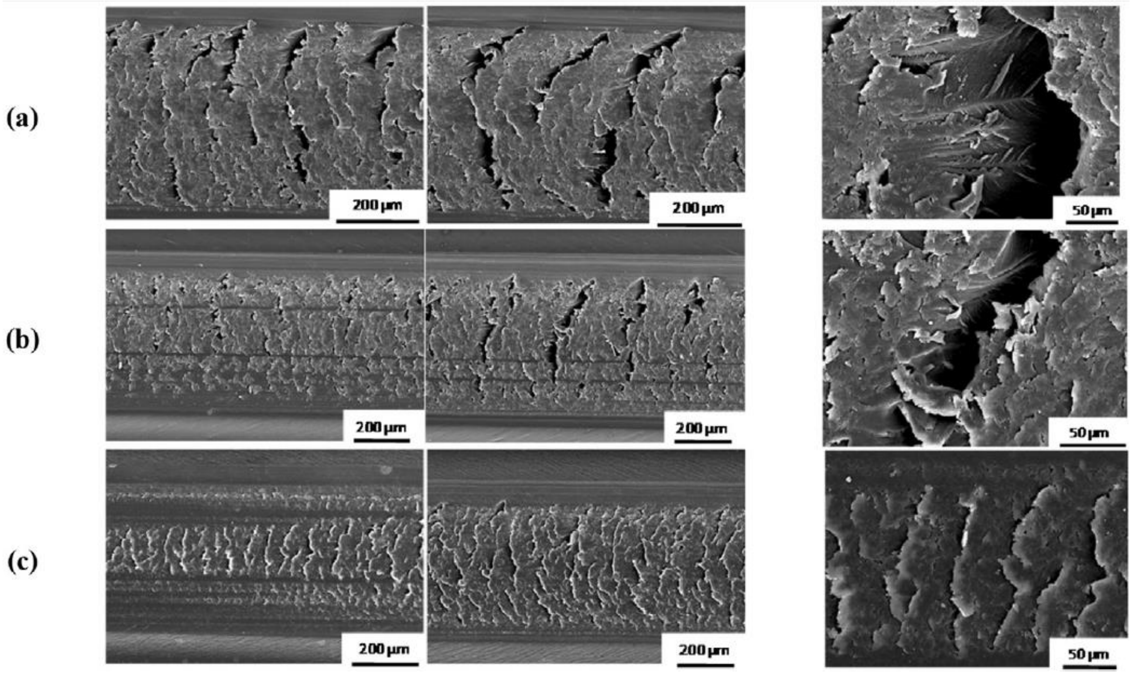

Figure II-3. SEM micrographs of well-developed crack (high resolution on the right) for a) nano-sized ASA system, b) nano-sized ABS system, and c) micron-sized ASA system. (Scratch direction: from left to right). Reprinted from Polymer, 63, Hossain, M.M., et al, Rubber particle size and type effects on scratch behavior of styrenic-based copolymers, 71-81. Copyright (2015), with permission from Elsevier [45].

These experimental studies contributed significantly to the understanding of scratch-induced damage in polymers. However, more fundamental insight on scratch behavior was gained using numerical analysis. Several studies utilized the FEM model described previously to provide a mechanistic explanation of scratch damage [9, 40, 53, 54]. Jiang et al. used the FEM model to characterize the stress field developed during the scratch test [40]. They found that material characteristics and complex surface stress states can be semi-quantitatively utilized to account for the observed scratch mechanisms. One of the most significant benefits of this FEM modeling is the ability to conduct a parametric analysis to separately determine the effect of each physical and constitutive parameters ceteris paribus [53, 54]. It is found that yield stress, coefficient of adhesive friction, and strain at stress recovery are the most important parameters that affect scratch visibility resistance. Another study used this FEM model to examine the scratch behavior of polymeric coatings on hard and soft substrates [9]. Figure II-4 shows maximum principal stress distribution beneath the scratch tip for acrylic–steel and polyurethane–polypropylene coating systems. It is found that the coating-substrate structure tremendously change the surface stress distribution, thus scratch behavior. In the case of soft substrate on hard coating (acrylic–steel), stress concentration areas are located at the rear side of scratch path (Area A) and in front of the scratch tip (Area B). These areas indicate the onset of crack damage during the scratch test. However, in the case of a hard coating on a soft substrate (polyurethane–polypropylene), the stress peaks are gradually developed behind the scratch tip as the normal load increases [9].

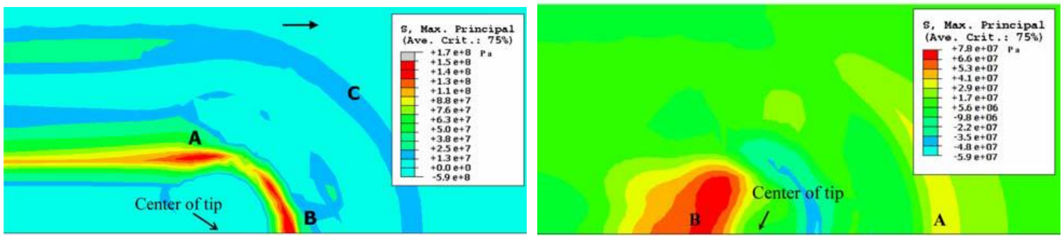

Figure II-4. Maximum principal stress field at normal load of 45 N (top view) for (left) acrylic–steel and (right) polyurethane–polypropylene coating systems. Reprinted from Tribology Letters, 37(2), Jiang, H., et al., Mechanical modeling of scratch behavior of polymeric coatings on hard and soft substrates, 159-167. Copyright (2010), with permission from Springer [9].

The studies presented previously were conducted on bulk polymeric materials. Limited research efforts were dedicated to the intrinsic scratch behavior of free-standing polymeric films and laminates. Ni and Faou observed scratch damage on a few polymeric laminates [55]. Based on the previous scratch ASTM/ISO standard, Hare et al. developed a new experimental method to evaluate the mechanical integrity of food packaging films and investigate the effect of film orientation and testing rate of scratch performance [56]. The method consists in a customized vacuum fixture that applies atmospheric air pressure to draw a vacuum beneath the film and secure it to the backing material. Thus, more intimate contact between the film and the backing is obtained and extraneous movements are minimized. This technique was later employed to study the scratch performance of commercialized polymeric laminates [41]. It is demonstrated that a vacuum pressure of 85 kPa is sufficient to obtain consistent results [41, 56]. This pressure will be considered in our analysis of scratch behavior on polymeric films and laminates. The impact of processing method on the laminate resistance to scratch damage was also studied [42].

Results show that extrusion laminated films have better scratch performances than adhesive laminated films.

The experimental studies discussed above shed some light on the scratch behavior on polymeric films and laminates. They demonstrated the ability of the experimental test to provide a layer-level analysis of scratch resistance. However, much more experimental and numerical studies are still needed to have a better insight and, ultimately, design polymeric laminates with improved scratch performance.

II.1.2.2.Analysis of mar behavior

A few experimental tests were previously employed to study mar damage. Laboratory car wash Amtec test is a realistic test designed to simulate mar damage caused by automated car wash machines following E DIN 55668 standard (Figure II-5) [30].

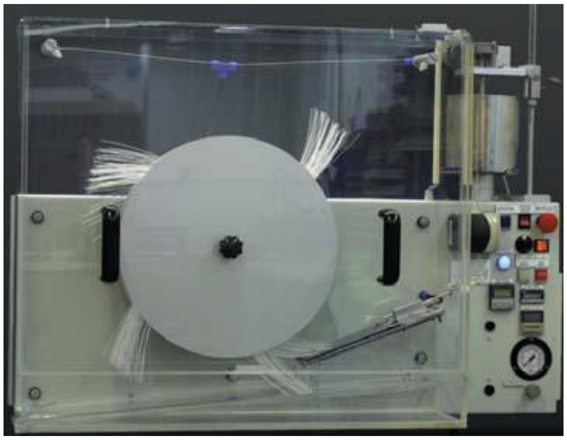

Figure II-5. Elcometer 1730 Car Wash Simulator.

Mar was also investigated using nanoindentation tests [28, 29]. Although the obtained scratch and mar damages have similar dimensions to those encountered in the field, the speed in these tests is limited by the data-taking rate of the indenter and cannot exceed 20 mm/s [28]. Also, micro- and nanoscratch tests were unable to provide a quantitative characterization of mar resistance. More sophisticated mar tests were performed based on the ASTM/ISO standard described previously [33, 34]. In these studies, mar was considered as the subtle pre-scratch darkening damage at low applied loads (Zone 1 in Figure II-6). To decrease the induced stress and generate more consistent mar damage, alternative mar tips with wider area were utilized such as the self-aligned stainless steel barrel tip [57] and the squared flat tip [58].

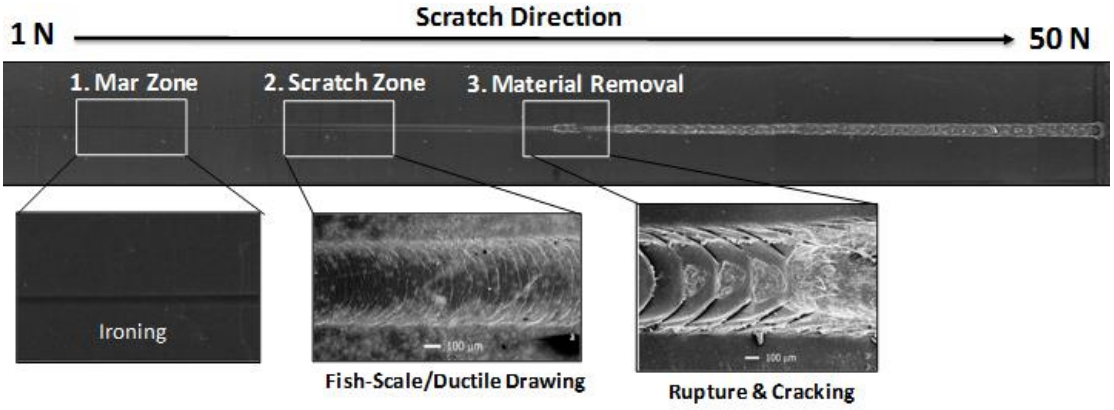

Figure II-6. Scratch transitions showing pre-scratch mar damage [34].

Previous studies tried to qualitatively characterize mar resistance through the polymer mechanical, optical, and topographical properties. Mechanical characterization was performed using scratch coefficient of friction (SCOF) which is the ratio of the tangential load to the normal load [57]. Figure II-7 presents the correlation found previously between mar resistance and SCOF. It is shown that polymer surface with higher SCOF tend to have poor mar resistance. The optical and topographical characterization of mar resistance were conducted based on gloss and roughness measurements, respectively [49, 58]. Based on these studies, a contrast-based evaluation of mar was introduced [57]. It is demonstrated that mar resistance can be quantified using the contrast between mar area and the background of the sample.

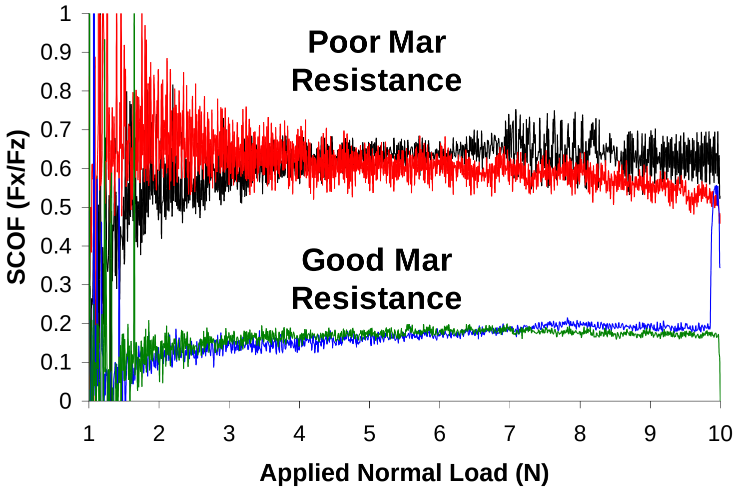

Figure II-7. Correlation between mar resistance and SCOF. Reprinted from Tribology International, 44/9, Browning, R., et al., Contrast-based evaluation of mar resistance of thermoplastic olefins, 1024-1031. Copyright (2011), with permission from Elsevier [57].

Mar quantification is still an ongoing effort. Since this faint damage is more dependent on surface properties, perceptual properties like brightness and color are expected to have a significant impact on its visibility resistance. Yet, to the best of our knowledge, the impact of these properties has not been studied previously.

II.1.2.3.Scratch and mar visibility resistance

Scratch and mar affect significantly the aesthetic properties of polymers. Previous studies investigated scratch and mar visibility resistance of these materials [57, 59, 60]. It was claimed that the hue-saturation-intensity (HSI) space combination can be used to quantify scratch visibility resistance [59]. However, these parameters, referred to by the authors as *Scratch Visibility Index* (SVI), were not consistent enough to quantify the perception of scratch damage on surface with different perceptual properties. Instead, Rangarajan et al. were able to accurately determine scratch visibility resistance using the contrast-based approach described previously [60]. A different study assessed this approach and demonstrated its reliability [57]. Based on these results, *Automatic Scratch Visibility* (ASV©) software was designed and commercialized by Surface Machine Systems (SMS) Company to consistently determine scratch visibility onset in polymers [61]. Three parameters are considered in ASV software: (1) The scratch should have at least 3% contrast against the background, (2) its feature size needs to be larger than 90 μm, and (3) its span within twice the diameter of the scratch tip should be continuous for at least 90% [62]. ASV visualization is conducted at least 24 hours after performing scratch and mar tests to account for the viscoelastic recovery. ASV results are often consistent with the psychophysical tests, i.e. the human observation tests. Based on the ASTM standard and ASV software, Jiang et al. used light scattering theories to establish a correlation between scratch perception and scratch dimensions, namely height and depth

[61]. It is suggested that higher dimensions correspond to lower visibility resistance. All the previous ASV studies are based on a scanner technique. Previous validation tests showed that higher resolution is needed to reliably capture scratch and especially mar damages on surfaces with different perceptual properties. Therefore, an alternative experimental setup should be considered to reliably quantify scratch and mar visibility.

II.2.RESEARCH STRATEGY

A flow chart of the current research study is presented in Figure II-8. The main objectives consist in (1) investigating scratch behavior on polymeric films and laminates and (2) studying mar behavior on bulk polymeric materials. To fulfill this purpose, the impact of mechanical (modulus, yield stress, and strain hardening coefficient), surface (COF, SCOF), and perceptual (brightness, transparency, and color) properties on scratch and mar behavior was determined through a variety of methods and techniques.

All the properties previously mentioned were studied based on fundamental, experimental, and psychophysical approaches. To investigate mechanical and surface properties, these approaches were supported with a numerical FEM analysis. Also, a statistical analysis was performed to study the perceptual properties. Experimental approach is mainly based on the standardized ASTM/ISO scratch test as well as other microscopic and spectroscopic techniques. The numerical simulation was conducted by modifying the sophisticated FEM model discussed previously. The psychophysical tests consist in human observation tests to validate the experimental findings. Up to 20 subjects were involved in mar observation tests. Finally, the statistical approach consists in conducting a multidimensional scaling (MDS) study to analyze mar observation results.

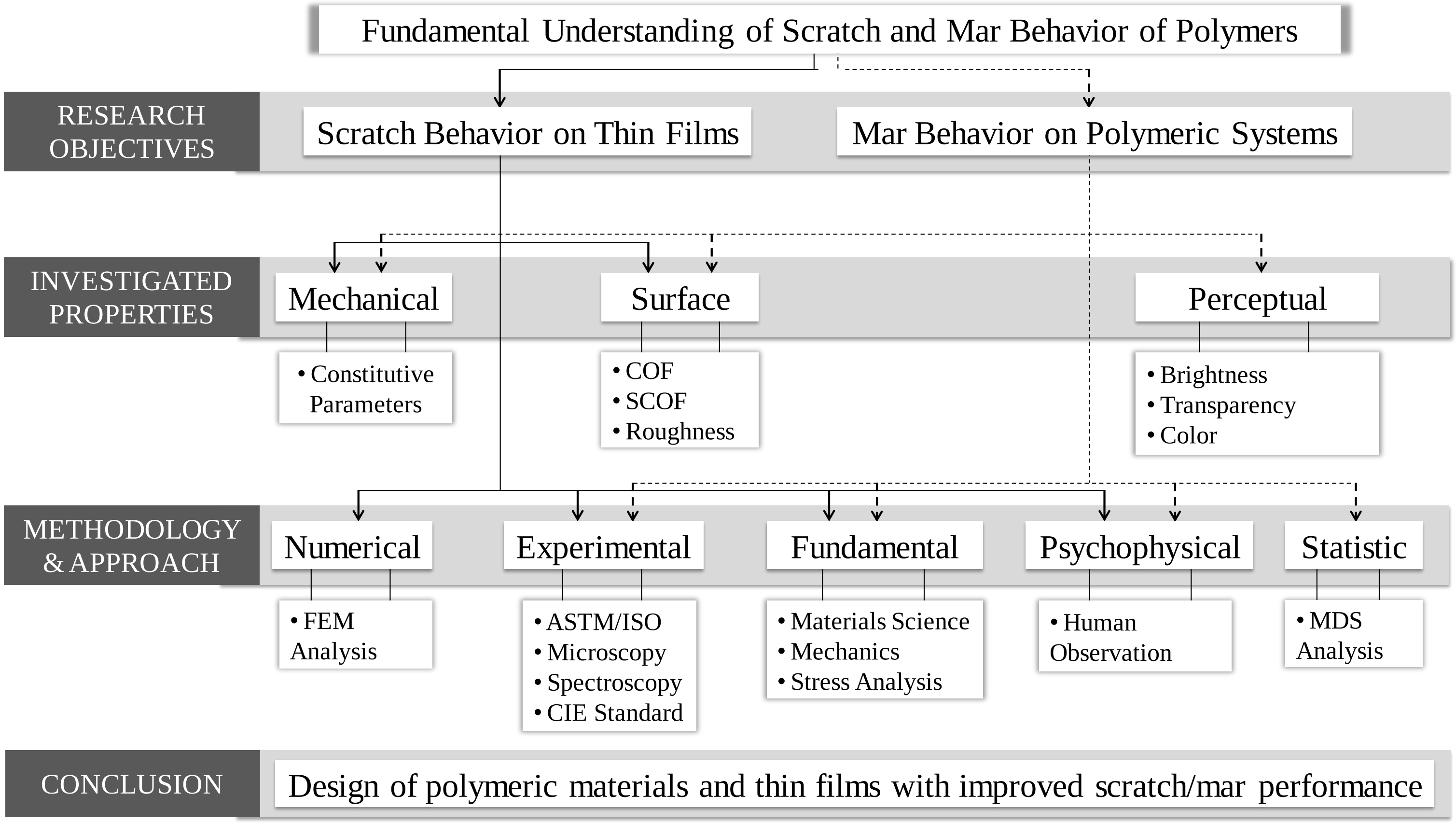

Figure II-8. Flow chart of the research strategy.

CHAPTER III

SCRATCH BEHAVIOR ON POLYMERIC FILMS *

One of the common approaches frequently utilized to enhance the mechanical performance of polymeric films is achieving a desired level of orientation through stretching. Uniaxially and biaxially stretched polypropylene (PP) films constitute over 60% of the manufactured films worldwide and over 6 million tons per annum [63]. They can be oriented through biaxial stretching, in both machine direction (MD) and transverse direction (TD), or only uniaxial stretching in MD. Also, orientation can be made by changing some processing parameters like air cooling conditions, chill roll temperature, and draw ratio [64]. Previous experimental studies showed that uniaxial orientation of PP films decreases their ductility [65] and increases their stiffness [66-68], yield stress [65, 67, 68], and ultimate tensile strength [65-68]. Also, orientation affects thermal [67, 69], barrier [67, 68], and optical [67, 68] properties of polymeric films. Another approach frequently used to change the properties of PP films is introducing comonomers, such as ethylene, during reactor polymerization. The incorporation of ethylene monomers in PP systems significantly decreases the level of its crystallinity because the comonomer site is a defect and cannot be incorporated into the crystal structure [70, 71].

---

* Part of this chapter was reprinted from Tribology International, 106, Hamdi, M., Puopolo, M., Pham, H., and Sue, H-J, Experimental and FEM analysis of scratch behavior on polypropylene thin films: Effect of film orientation and ethylene monomer content, 412-422. Copyright (2016), with permission from Elsevier.

Using the standardized ASTM/ISO scratch test and the FEM model presented previously, the impact of film orientation and comonomer addition on the scratch performance of model PP-based polymeric films has been investigated.

III.1.EXPERIMENTAL

III.1.1.Model Systems

Table III-1 summarizes the model systems used in this study. They consist in single layer cast films with significantly high level of transparency. Three commercialized model PP systems were employed to investigate the effect of ethylene content on scratch resistance. They consist of isotactic PP homopolymer and two random PP copolymers with ethylene contents of 3 wt% and 5 wt%, respectively. The ethylene content was determined by the manufacturer during the processing of the model systems. For each type, four levels of uniaxial orientation in MD were performed to determine the orientation effect. The employed stretch ratios are 1x, 4x, 5x, and 6x, respectively, where the symbol 'x' represents the multiple amount of stretching in MD, i.e. 1x = 100 % and 2x = 200 % etc. The degree of film orientation was also performed and reported by the manufacturer. The film designation is indicated in Table III-1 and will be respected in this chapter. Furthermore, to have a better insight on the processing of the films, the melt flow rate (MFR), density, supplier, and grade of PP used for each film are indicated in the table. The films were kindly provided by Avery Dennison Company.

III.1.2.Measurements of Film Properties

Thickness plays a major role in the structure and the mechanical integrity of polymeric thin films [72]. Also, surface roughness and friction between the scratch tip and the model systems affect the scratch behavior of polymers [49, 73]. Moreover, a good film adhesion to the backing is crucial to have consistent results. A considerable difference in one of these parameters, namely thickness, roughness, friction, and adhesion, may affect our results and lead to the misinterpretation of our findings. For instance, the difference in scratch behavior between two films can be caused by the difference in their thickness values, and not necessarily the difference in their orientation or ethylene content. Therefore, measurements were conducted to verify the consistency of these parameters amongst the films. Hence, the effects of orientation and ethylene addition can be accurately studied.

To precisely perform the thickness measurements, a digital gauge manufactured by Mitutoyo with an accuracy of 1 μm was employed. It is designed to apply an insignificant, but consistent force on the films to avoid affecting their thickness measurements. As for roughness, high-resolution KEYENCE VK-9700K violet laser scanning confocal microscope (VLSCM) was employed to measure this parameter. In scientific measurements, root mean square roughness (R_q) is frequently used for fine surfaces because it is more sensitive to peaks and valleys than arithmetic average roughness (R_a). Therefore, we consider using this parameter in our measurements for accuracy purposes. Also, to obtain more normalized results, five roughness measurements, each over an area of 50 x 50 μm^2, were conducted for each film. The surface coefficient of friction COF (μ) was determined using a squared flat smooth stainless steel tip with dimensions of 10 mm x 10 mm. The tip was installed on the scratch machine described in Chapter II. Then, low constant normal load of 5 N was applied over a distance of 100 mm at a speed of 100 mm/s to measure the surface friction. Finally, a vacuum pressure of 85 kPa was maintained between the examined films and the aluminum backing to obtain good film-substrate adhesion as indicated previously [41, 56].

III.1.3.Characterization of the Mechanical Properties

Uniaxial tensile tests were conducted in accordance with ASTM D1708-13 standard [74]. This standard is employed to compare the tensile strength and elongation properties of the model systems. The tests were performed in MD at a constant crosshead speed of 2.5 mm/min under ambient temperature using a load frame equipped with a 2.5 kN load cell. The specimens were cut in a dog-bone shape using a punch and their dimensions were measured using a micrometer caliper. The narrow section has a length of 22 mm and a width of 5 mm. Also, a sand paper between the grip and the samples was utilized to avoid their sliding. Finally, the scratch tests were conducted on the films with respect to the ASTM/ISO standard as described in the literature review.

III.2.FEM MODELING

The scratch test on the polymeric films is simulated based on the FEM model described in the literature review. This model was modified to consider the film-substrate structure and test conditions (Figure III-1). Figure III-1 also shows the refined mesh in the area beneath the scratch tip. For more realistic results, the properties of the aluminum backing and PP film were initially introduced in the FEM model in accordance to the literature [75-77]. Their constitutive behavior was simulated as piecewise linear elastic–plastic stress–strain curves as demonstrated in [40].

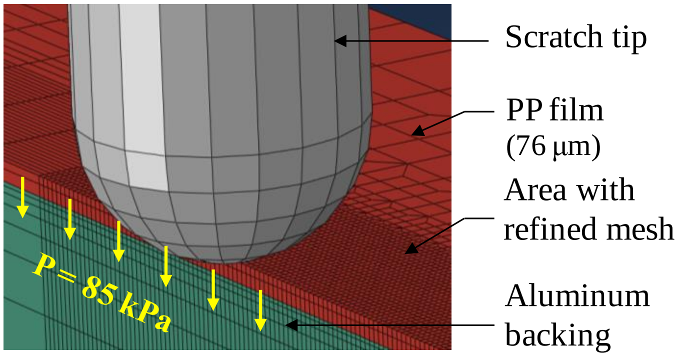

Figure III-1. Modeled film-backing structure and refined mesh in the scratch area.

The main constitutive parameters are modulus (E), yield stress (σ_y), softening slope (s), and hardening slope (h). The values of these parameters, as well as Poisson's ratio (ν) and density (ρ), of the modeled materials are summarized in Table III-2. The corresponding references for adopting these values are also indicated in this table. Then, the constitutive parameters of PP film were modified accordingly to perform the parametric analysis as will be described later. When a parameter is changed, the remaining parameters are fixed and equal to the values shown in Table III-2. For simplification purposes, the anisotropy of the films will not be considered in the FEM model, and all the films are assumed to be isotropic in the parametric analysis.

III.3.RESULTS AND DISCUSSION

III.3.1.Characterization of the Model Systems

Experimental measurements of thickness, roughness, and friction of the experimental model systems are presented in Table III-3. It is demonstrated in the table that the unoriented films, PP-1, P3E-1, and P5E-1, have considerably higher thickness values than the remaining films. Also, the roughness of PP-1 and P5E-1 is significantly higher than the average value of the other films. Therefore, PP-1, P3E-1, and P5E-1 will not be included in our analysis. All the remaining films have similar values of thickness, roughness, friction, and adhesion to the backing material. They will be considered to determine the effects of film orientation and ethylene content on scratch resistance. After validating the consistency of the thickness, roughness, friction, and adhesion across the studied films, we consider now determining the effects of film orientation and comonomer addition on its mechanical properties. The tensile stress-strain curves of the model films are presented in Figure III-2 and Figure III-3. In Figure III-3, the impact of film orientation on the constitutive behavior of PP (Figure III-3a), P3E (Figure III-3b), and P5E (Figure III-3c) is presented. Results show that for each film, higher orientation leads to an increase in modulus, yield stress, and ultimate strength and a decrease in film ductility. These results are in good agreement with previous studies found in the literature about the effect of the orientation of PP films on its modulus [66-68, 78, 79], yield stress [65, 67, 68], strength [65-68], and ductility [65]. For instance, Moseley and Ward were able to relate the orientation of amorphous polymers to Young's modulus (E) and find the relation presented in Equation 1 [78, 79], where E_u refers to the modulus value before orientation, E_{max} refers to the modulus value after the prescribed orientation is achieved, Δn is the orientation birefringence, and Δn_{max} is the maximum orientation birefringence. Equation 1 shows that Young's modulus increases with higher molecular orientation.

$$1-\frac{E_u}{E}=\frac{\Delta n}{\Delta n_{max}}\left(1-\frac{E_u}{E_{max}}\right) \qquad (1)$$

Table III-1. Model systems used in the study.

Composition	PP Homopolymer				Random Copolymer (3wt% ethylene)				Random Copolymer (5wt% ethylene)			
Stretch ratio	1x	4x	5x	6x	1x	4x	5x	6x	1x	4x	5x	6x
Designation	PP-1	PP-4	PP-5	PP-6	P3E-1	P3E-4	P3E-5	P3E-6	P5E-1	P5E-4	P5E-5	P5E-6
MFR (g/10min)	4.2				1.9				5			
ρ (g/cm^3)	0.9				0.9				0.9			
Supplier/ Grade	Flint Hill Resources / FHR P4-050F				Flint Hill Resources / FHR-43S2A				Braskem / DS6D81			

Table III-2. Tensile and physical properties of the modeled aluminum and PP

	E (GPa)	ν	σ_y (MPa)	s (MPa)	h (MPa)	ρ (g/cm^3)	References
Al	70	0.33	276	-	320	2.7	[75]
PP	1.5	0.4	30	-100	50	0.905	[76, 77]

Table III-3. Thickness, roughness, and COF of the model systems.

	PP Homopolymer				Random Copolymer (3wt %)				Random Copolymer (5wt %)			
Film	PP-1	PP-4	PP-5	PP-6	P3E-1	P3E-4	P3E-5	P3E-6	P5E-1	P5E-4	P5E-5	P5E-6
Thickness (μm)	**254**	76	76	76	**178**	76	76	76	**254**	76	76	76
R_q (nm)	**192**	78	91	79	91	109	110	110	**182**	71	83	91
(Std. Dev)	**(12)**	(10)	(14)	(11)	(7)	(20)	(19)	(18)	**(20)**	(9)	(7)	(14)
μ	0.34	0.33	0.38	0.31	0.36	0.30	0.31	0.29	0.47	0.38	0.40	0.38

Similarly, the effect of ethylene comonomer content on the constitutive behavior of the films is shown in Figure III-2. Our results demonstrate that, for a given orientation, the ultimate strength decrease with increasing amount of ethylene content. This result is in good agreement with results found elsewhere [80]. It is also consistent with measurements performed by the suppliers according to similar ASTM standards Table III-4. As shown in Figure III-2, although ethylene addition improved the impact strength of PP films, it caused a decrease in film strength and flexural modulus. Consequently, the main constitutive properties affected by film orientation and ethylene addition are modulus, yield stress, ultimate strength, and ductility. The effect of these properties on scratch behavior will be investigated later in the parametric FEM analysis.

Table III-4. Mechanical properties measurements provided by the suppliers.

	PP	P3E	P5E
Tensile Yield Stress (MPa)	39	26.2	19
Flexural Modulus (1% secant) (MPa)	1520	835	550
Notched Izod Impact Strength @ 23° (J/m)	40	--	91

III.3.1.Scratch Resistance

We consider now investigating the scratch behavior of the examined model systems. Whitening and puncture damages are the main scratch features on thin polymeric films. In fact, they lead to scratch visibility and ultimate failure, respectively.

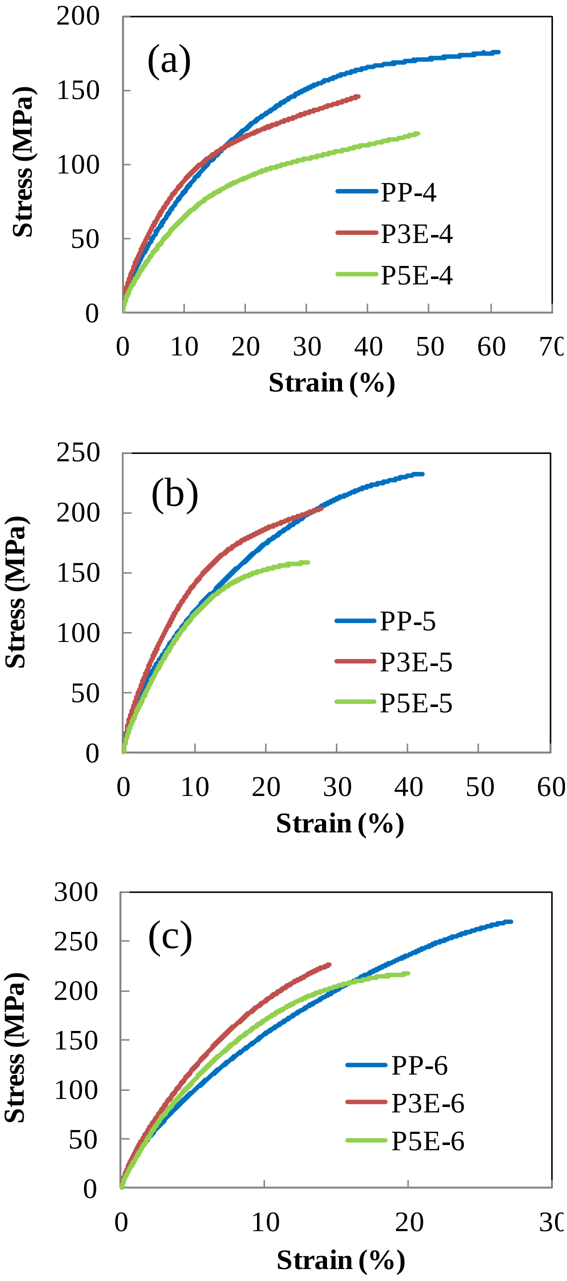

Figure III-2. Effect of the ethylene content on the constitutive behavior of films with (a) 4x (b) 5x and (c) 6x stretch ratios.

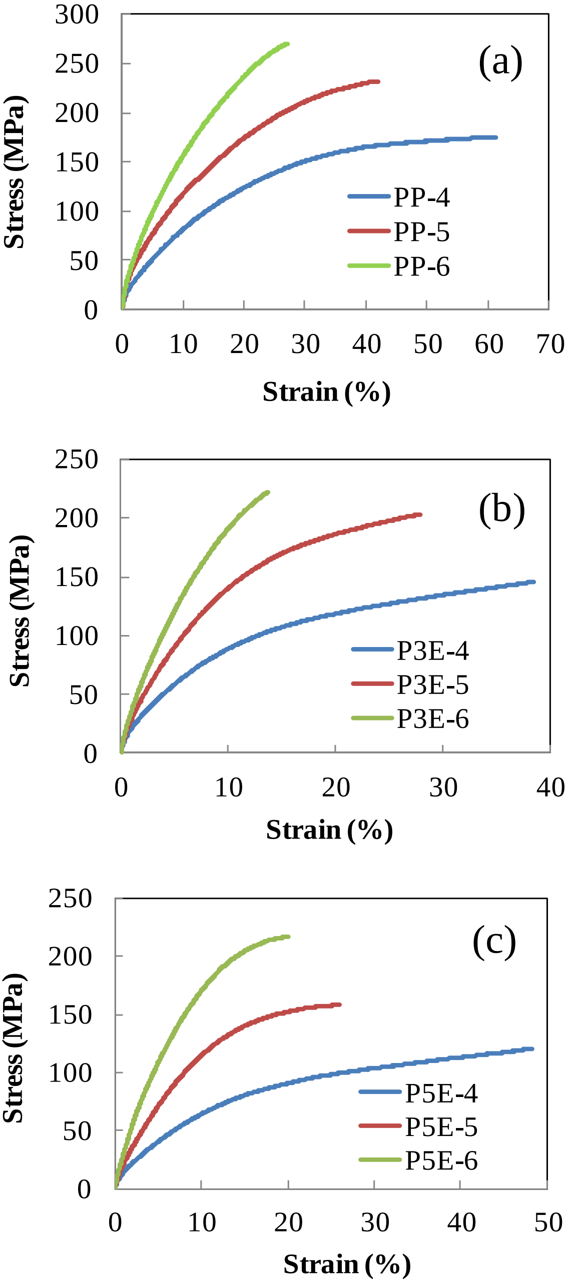

Figure III-3. Orientation effect on the constitutive behavior of (a) PP (b) P3E and (c) P5E films.

Whitening and puncture resistances in MD are presented in Figure III-4. Whitening resistance (puncture resistance) corresponds to the normal load required for the onset of whitening damage (puncture damage). A higher load refers to a better resistance to the corresponding damage. To determine the corresponding loads of the onset of whitening or puncture damages, the point at which the studied damage (whether whitening or puncture) appears was determined visually. Then, its corresponding distance was accurately measured using an electronic digital vernier caliper gauge micrometer ruler. After finding the damage position, the corresponding load is determined using the output datasheet of the scratch test obtained from the scratch machine.

The low standard deviation in Figure III-4 demonstrates the self-consistency of the experimental approach. Figure III-4a shows that whitening damage occurs at the very beginning of the scratch path where the normal load is quite low and do not exceed 6 N. It is also observed that the difference in whitening loads between the samples does not exceed 2 N which is considerably insignificant, given the scratch load of 45 N. This suggests that the impact of film orientation and composition on whitening resistance is insignificant. However, Figure III-4b shows that puncture onset loads are significantly higher and reach higher than 50 N. Also, the difference between the studied films in puncture resistance is important and can reach up to 30 N. Consequently, we will focus on puncture resistance and we will refer to this parameter as scratch resistance for the rest of the chapter as was done previously [41, 56].

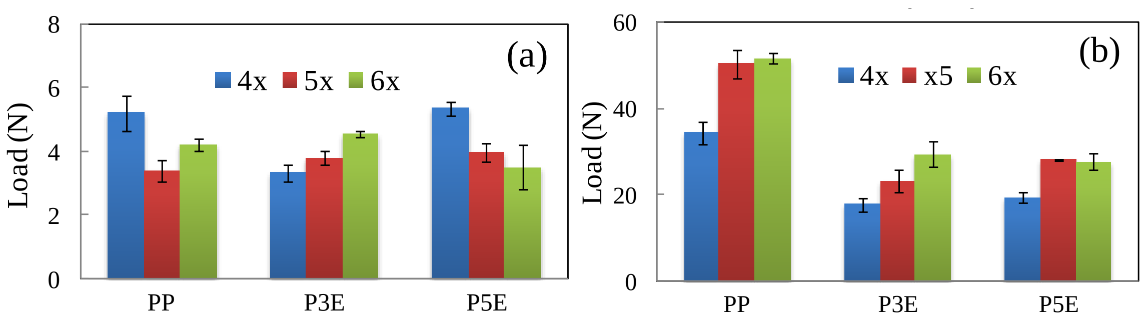

Figure III-4. Resistance of the films to (a) whitening and (b) puncture damages in MD.

III.3.1.1.Effect of film orientation

Figure III-4b demonstrates that for each film type, the scratch resistance in MD improves with increasing orientation. This result is explained by the improvement of the mechanical properties of the films after orientation. In fact, as discussed earlier our tensile results show that the film modulus, yield stress, and ultimate strength improve with higher orientation (Figure III-3). However, the improvement of scratch resistance in MD after orientation may not necessarily occur in TD. This can be validated by comparing the scratch behavior of the films in the two directions.

III.3.1.2.Comparison between MD and TD

It is observed that, for all oriented films, when scratch is conducted in MD, puncture damage is localized and has the same direction as the scratch damage. However, when scratch is performed in TD, puncture occurs in a coarse fashion and the surrounding area affected by the scratch damage is much wider. This observation encouraged us to compare the scratch resistance of the model films in the two directions.

Figure III-5 below illustrates the scratch resistance of the studied films in TD. Again, the low standard deviations demonstrate the self-consistency of the results and the reliability of the experimental approach. The orientation effect found previously in MD does not appear in TD. In fact, the scratch resistance of the films in TD did not improve with higher film orientation. Also, the comparison between Figure III-4b and Figure III-5 demonstrates that scratch resistance in MD is higher than that in TD for each of the studied films. This result is consistent with previous investigations on the impact of the orientation on the mechanical properties of PP films. It was found that MD-oriented PP films have better tensile properties [64] and impact strength [67] in MD than in TD. Particularly, Shinozaki and Groves showed that tensile yield stress of oriented PP films has the highest value when the test direction is similar to the orientation direction, steadily decreases when the angle between the two directions increases, and reaches a minimum value when the two directions are perpendicular [81]. Similar observation was also made for other films like PET [82] and different types of PE [83]. All these studies show that uniaxial orientation is performed to mainly improve the mechanical performances of the films in the same direction. This explains why the scratch resistance of our MD-oriented model systems is higher in MD than in TD.

We consider now determining the orientation effect on the difference in scratch resistance between MD and TD, namely $\Delta \mathrm{R}_{\mathrm{Scratch}}$ defined in Equation 2. $\mathrm{R}_{\mathrm{Scratch}}$ (MD) and $\mathrm{R}_{\mathrm{Scratch}}$ (TD) are the scratch resistance in MD and TD, consecutively:

$$\Delta \mathrm{R}_{\mathrm{Scratch}}(\%) = \frac{\mathrm{R}_{\mathrm{Scratch}}(\mathrm{MD}) - \mathrm{R}_{\mathrm{Scratch}}(\mathrm{TD})}{\mathrm{R}_{\mathrm{Scratch}}(\mathrm{MD})} \text{ x } 100 \qquad (2)$$

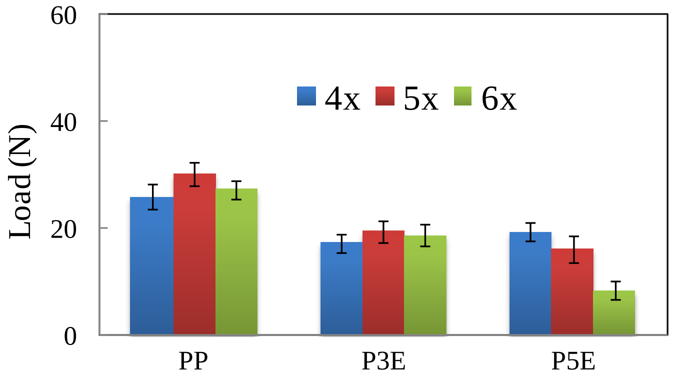

Figure III-5. Scratch resistance of the model systems in TD.

Results are presented in Figure III-6 in terms of the film stretch ratio. The positive slopes of the curves in the figure indicate that for each film type, when the film orientation increases, $\Delta R_{Scratch}$ increases. In other words, higher orientation leads to higher gap between the scratch resistance in MD and that in TD. This result is in agreement with a previous study on MD-oriented PP films where the difference in impact strength between MD and TD is more significant with increasing orientation [67]. This is explained by the increasing anisotropy between MD and TD in film structure with higher orientation, which increases the anisotropy in tensile properties and scratch resistance. It is also observed in Figure III-6 that $\Delta R_{Scratch}$ curves of P3E and P5E have higher slopes than that of neat PP. This result indicates that the change in $\Delta R_{Scratch}$ from one orientation to another is enhanced by the incorporation of ethylene comonomer.

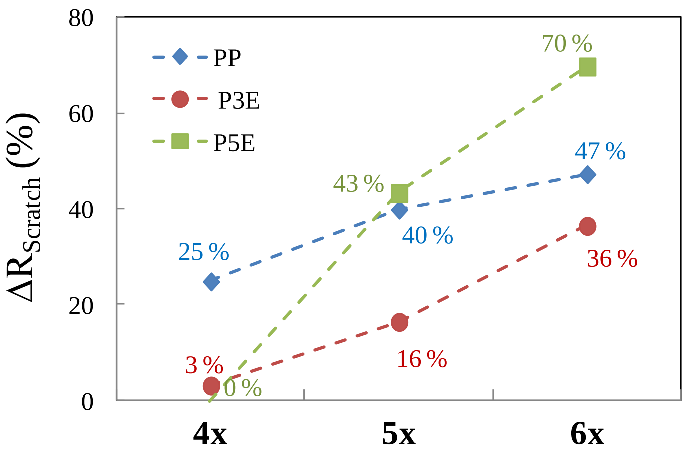

Figure III-6. Difference in scratch resistance between MD and TD in terms of film orientation.

The comparison between scratch behaviors in MD and TD shows that higher scratch resistance and less severe scratch are obtained in MD. This is explained by the improvement of film tensile properties in this direction. Furthermore, the difference in scratch resistance between the two directions is increased with higher film orientation, especially when ethylene comonomer content is high. This observation leads us to the analysis of the impact of ethylene content on the scratch resistance of the films.

III.3.1.3.Effect of ethylene content

In Figure III-4b, the scratch resistance of PP homopolymer in MD is clearly higher than that of the random copolymers. No significant change in scratch resistance is observed between P3E and P5E. This observation is consistent for all the three studied orientation levels. It is explained by the decrease in film tensile properties after the addition of ethylene comonomers (Figure III-2 and Table III-4) thus decreasing the film scratch resistance in MD, and increasing the gap between MD and TD resistance values.

III.3.2.FEM Parametric Analysis

The experimental results above demonstrate the improvement of scratch resistance with higher film orientation and lower ethylene content. A correlation was made between this change in scratch resistance and the general impact of orientation and ethylene addition on the constitutive parameters of the films. However, to have a better understanding, the direct effect of each of these constitutive parameters, ceteris paribus, on the film scratch resistance should be assessed. This can be best performed by conducting a parametric analysis using FEM modeling.

III.3.2.1.Constitutive parameters

Based on our tensile results, the major constitutive parameters significantly affected by film orientation and ethylene content are modulus, yield stress, ultimate strength, and ductility. These parameters will be studied using our FEM model. However, since elements separation and removal after damage are not considered in our numerical simulation, ductility will not be considered. Hence, post-yielding behavior and particularly ultimate strength will be investigated by studying strain hardening effect.

The piecewise linear elastic–plastic stress–strain curves introduced to the FEM model for the parametric analysis are shown in Figure III-7. The black curve in the figure reflects the initial PP constitutive parameters shown in Table III-2. The values used to determine the modulus effect are 550 MPa, 820 MPa, and 1.50 GPa (blue curves). Similarly, those employed to study the yield stress effect are 30 MPa, 50 MPa, and 70

MPa, respectively (green curves). Finally, three constant hardening slopes, 50 MPa, 70 MPa, and 90 MPa, were considered to determine the strain hardening effect (red curves).

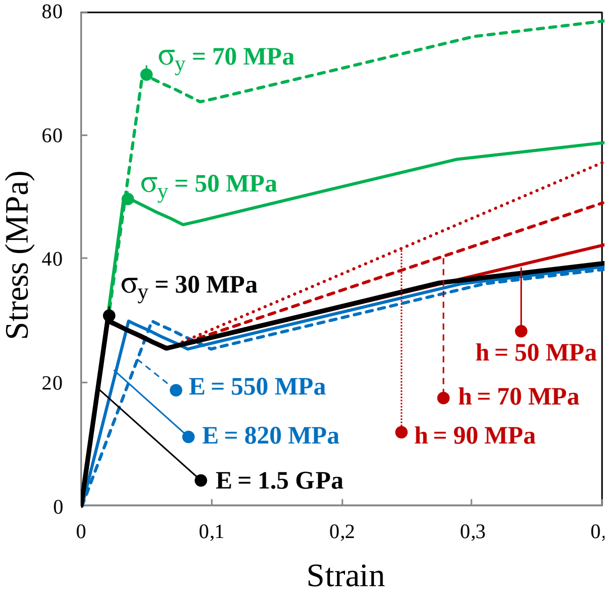

Figure III-7. Constitutive parameters considered in the FEM parametric analysis.

Scratch resistance is determined through scratch dimensions, namely height and depth [54]. Higher scratch deformation corresponds to lower scratch resistance. These dimensions can be easily obtained in the FEM model for each scratch position as illustrated in Figure III-8. All the scratch dimensions reported in this section are obtained at the end of scratch test, i.e., when the normal load is equal to 20 N. For each of the parameter considered, we will determine its effect on scratch resistance and stress distribution at the interface and on the film surface. Then, the numerical results will be correlated with our experimental findings.

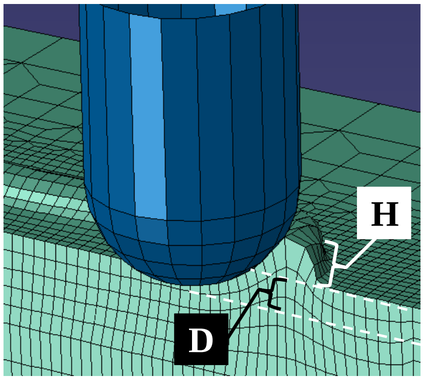

Figure III-8. Scratch depth (D) and height (H) obtained using the FEM model.

III.3.2.2.Effect of film modulus

Figure III-9 presents the impact of the Young's modulus of the film on scratch dimensions. It shows that scratch depth and height increase with higher modulus values. Hence, the scratch resistance of the films decreases with higher modulus. To have a better insight on modulus effect, the stress distribution on the film surface and across the film-backing interface is examined. Figure III-10 presents instantaneous von Mises stress distribution beneath and behind the scratch tip for the three moduli values when the applied load is 16 N. The longitudinal views, showing the stress distribution across the system depth, are presented in the upper part of the figure. The top views, showing the stress distribution on the film surface, are presented in the lower part of the figure. For a better visualization, the undeformed shape of the films is considered and the scratch tip is removed from the top views. Also, the dashed line in the longitudinal view indicates the interface between the film and the aluminum backing.

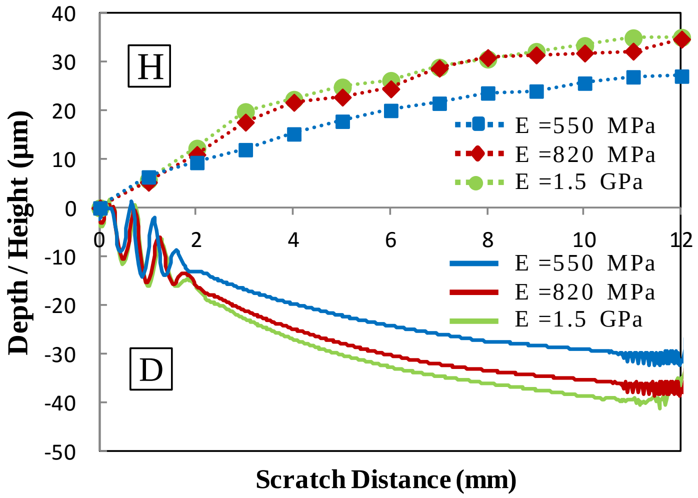

Figure III-9. Effect of film tensile modulus on scratch height (H) and depth (D).

The longitudinal view demonstrates that the interfacial stress increases in area and in magnitude with increasing modulus value. Using mode II stress intensity factor, a previous study showed that interfacial shear stress increases with increasing film stiffness [84]. Similarly, a theoretical expression of interfacial shear stress (τ) between a thin elastic film and relatively thick elastic substrate was determined (Equation 3), where r, E_f, $h_f, \nu_f, and\ \varepsilon_m$ correspond to the polar coordinate, film Young's modulus, film thickness, film Poisson's ratio, and nonuniform misfit strain, respectively [85]:

$$\tau = -\frac{E_f\, h_f}{1-\nu_f}\,\frac{d\varepsilon_m}{dr} \qquad (3)$$

This expression clearly shows that the magnitude of the interfacial shear stress is proportional to the film modulus. Although a different stress component is employed in our analysis (von Mises stress), these results are consistent with our findings in demonstrating that interfacial stress increases with higher modulus.

Also, the top views show more pronounced stress concentration on the film surface when E = 550 MPa. Thus, the increase in film modulus is associated with the shift of the stress concentration from the film surface toward the film-substrate interface. It is also associated with the decrease of the scratch resistance (Figure III-9). Therefore, it is concluded that the decrease of film scratch resistance is correlated with the shift of stress concentration from the surface to the interface. This is explained by significant interfacial stress role in creating interfacial damages (fracture, delamination ...) initiating usually at the interface [84-87]. This observation will be verified for other sets of parametric studies.

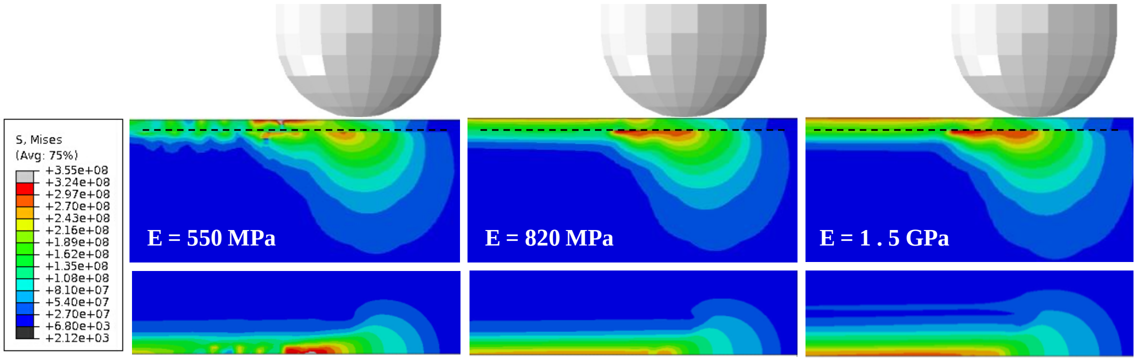

Figure III-10. Longitudinal (upper) and top (bottom) views of von Mises stress distribution (in Pa) beneath the scratch tip for the examined moduli values (L=16 N).

The experimental findings of this study show that both the modulus and the scratch resistance of the films increase with higher orientation. This may intuitively lead to the conclusion that scratch resistance improves with higher modulus. However, the FEM analysis demonstrates that scratch resistance decreases with higher modulus. This is explained by the increase of interfacial stress with higher modulus values. Therefore, other constitutive parameters, also affected by film orientation and ethylene content, are most likely to be responsible for improving the scratch resistance of the studied films.

III.3.2.3.Effect of film yield stress

The effect of film yield stress on scratch deformation is shown in Figure III-11. Higher yield stress corresponds to lower scratch depth and height. This demonstrates that higher yield stress leads to a better scratch resistance.

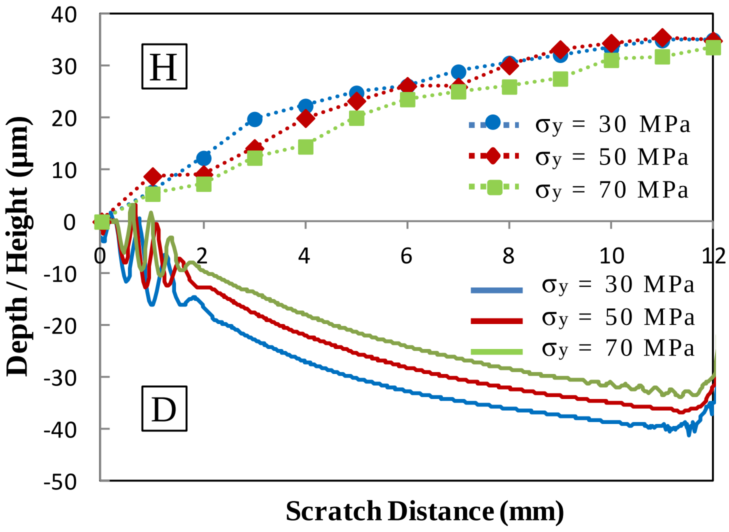

Figure III-11. Effect of film yield stress on scratch height (H) and depth (D).

Similar to modulus analysis, the yield stress effect on von Mises stress distribution is presented in Figure III-12. The longitudinal views show that interfacial stress slightly decreases with higher yield stress.

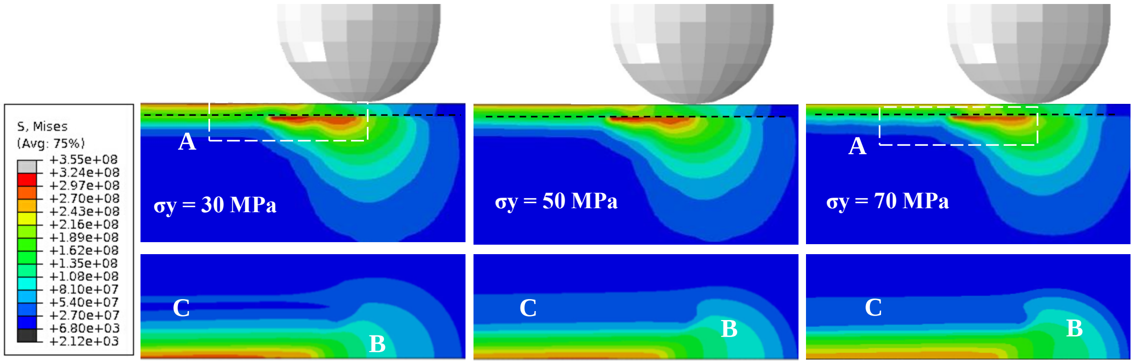

Figure III-12. Longitudinal (upper) and top (bottom) views of von Mises stress distribution (in Pa) beneath the scratch tip for examined yield stress values (L=16 N).

For a better visualization, the area A is zoomed for $\sigma_y = 30\ MPa$ and $\sigma_y = 70\ MPa$ and shown in Figure III-13. This figure better demonstrates the slight decrease of the stress distribution across the interface beneath and behind the scratch tip for higher yield stress (black arrows). The top views in Figure III-12 show that for higher yield stress values, the stress distribution is slightly higher beneath the scratch tip (Zone B) and more continuous at the edge of the scratch path (Zone C). Therefore, it is observed that lower yield stress corresponds to slightly shifting the stress distribution from the surface to the interface. Also, scratch resistance decreases with lower yield stress (Figure III-11). Therefore, the parametric analysis also suggests that the decrease of the scratch resistance is associated with stress distribution shift from the film surface to the film-backing interface. This is consistent with previous modulus effect study.

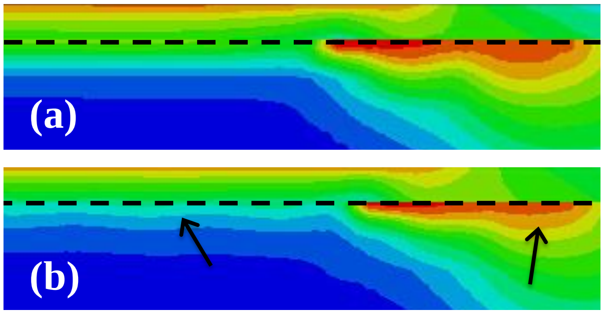

Figure III-13. Zoomed area A for a yield stress of (a) 30 MPa and (b) 70 MPa.

We consider now comparing the FEM results with experimental findings. According to our tensile tests, higher yield stress is obtained for higher film orientation and lower ethylene content. The scratch tests also showed that scratch resistance improved with higher film orientation and lower ethylene content. Therefore, this observation suggests that yield stress is responsible for improving the scratch resistance of the films. This observation is supported with our FEM simulation which demonstrates that scratch resistance improves with higher yield stress values. This improvement is associated with shifting the stress distribution from the interface towards the surface. We consider now investigating the effect of the main post-yielding constitutive parameter in polymeric materials, namely, strain hardening.

III.3.2.4.Effect of film strain hardening

The effect of strain hardening slope on scratch dimensions is presented in Figure III-14. As clearly shown in the figure, lower scratch depth and height are obtained for higher hardening slope. Therefore, the FEM results demonstrate that films with more significant strain hardening have better scratch resistance.

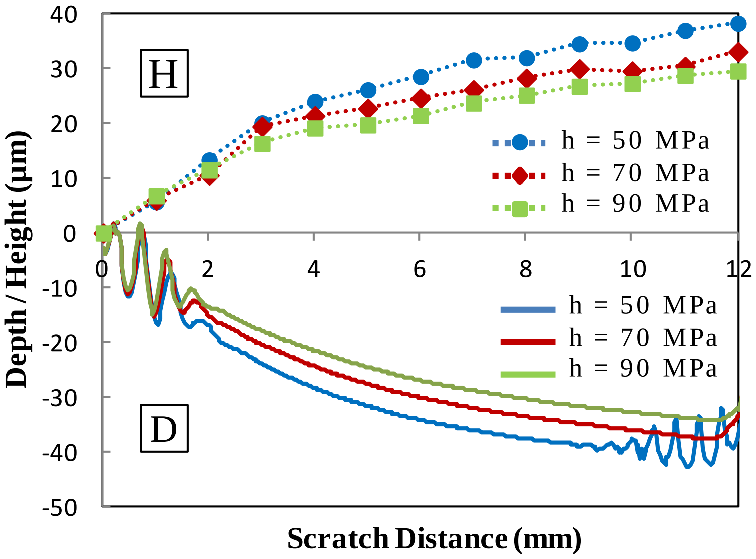

Figure III-14. Effect of film strain hardening slope on scratch height (H) and depth (D).

Similarly, the effect of hardening slope on interfacial and surface stress distributions is presented in Figure III-15. It is clearly shown in the figure that the stress concentration on the surface increases while that at the interface decreases with higher hardening slopes. Also, scratch resistance improves with higher hardening slopes (Figure III-14). Therefore, the correlation found previously between the improvement of scratch resistance and the shift of stress concentration from the film-backing interface to the film surface holds also for the strain hardening analysis.

We consider now comparing this result with the experimental findings. Our experimental tensile and scratch tests demonstrate that both ultimate strength and scratch resistance increase with higher orientation and lower ethylene content. This suggests that ultimate strength plays an important role in improving the scratch resistance of the films. This result was validated by our parametric FEM analysis where scratch resistance improves with higher strain hardening, thus higher ultimate strength.

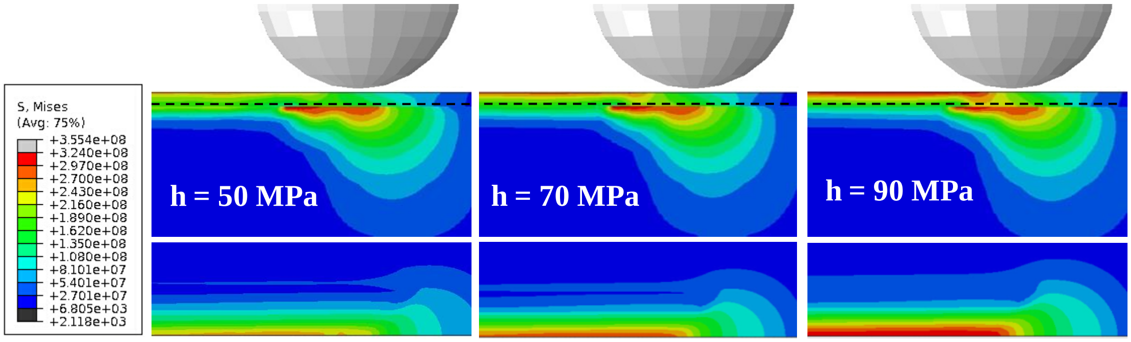

Figure III-15. Longitudinal (upper) and top (bottom) views of von Mises stress distribution (in Pa) beneath the scratch tip for different hardening slope values (L=16N).

It has been recognized that normalized dimensionless parameters are of good choice to investigate effect of material parameters on properties. For instance, the ratio H^3/E^2 is employed to correlate hardness to mechanical properties and compare hardness tests to mechanical counterparts (tensile, scratch...) [88, 89]. However, these normalization choices can sometimes be quite arbitrary and might not bear physical relevance to each other. In this study, we found it to be more direct to investigate the impact of each material parameter on scratch behavior separately instead of normalizing them into dimensionless parameters.

This chapter aims at investigating the effect of orientation and ethylene content on the scratch behavior of PP thin films. The experimental tests show that scratch resistance is improved and scratch damage is more localized when the scratch direction is the same as the molecular orientation direction. Therefore, while using oriented PP films for industrial applications, it is recommended to align the film orientation with the expected scratch direction. Also, scratch resistance is improved with higher orientation and lower ethylene content. The tensile tests demonstrate that the tensile properties affected by orientation and ethylene addition are modulus, yield stress, ultimate strength, and ductility. To accurately determine which of the constitutive parameters is responsible for improving scratch resistance, a numerical parametric analysis was performed using a sophisticated FEM simulation. Results demonstrate that yield stress and strain hardening are the most influential constitutive parameters. Better scratch resistance is obtained with higher yield stress and higher hardening slope. Also, the FEM simulation shows that the improvement in scratch resistance is associated with the shift of stress concentration from the film-substrate interface toward the film surface.

III.4.CONCLUSIONS

In this chapter, the impact of orientation and ethylene comonomer content on the scratch resistance of PP films was investigated. The present study demonstrates that scratch resistance improves with higher film orientation and lower ethylene content. A correlation was found between the effect of film orientation and ethylene addition on the tensile properties, and their effect on scratch resistance. Results show that higher film orientation and lower ethylene content correspond to higher modulus, yield stress and ultimate strength. These improvements in the tensile performance of the films lead to the enhancement of their scratch resistance. Also, a comparison was made between scratch behavior in MD and TD. Results show that higher scratch resistance and less severe puncture are obtained in MD. This is explained by the improvement of the tensile properties of the oriented films in this direction. Also, this difference in scratch resistance between MD and TD is magnified by higher orientation, especially when ethylene comonomer amount is increased. This is explained by the role of orientation in increasing the film anisotropy. To accurately determine which tensile property is responsible for improving scratch behavior, a parametric analysis was conducted using the FEM model. Results show that the improvement of scratch resistance is associated with the shifting the stress concentration from the film-backing interface to the film surface. Also, it is demonstrated that scratch resistance is insensitive to film modulus. Instead, it is improved with higher yield stress and higher strain hardening.

After investigating scratch behavior on single polymeric films in this chapter, we consider determining the scratch performance of multilayered films or laminates frequently used in the industry. In the next chapter, we examine the scratch behavior of these systems and we determine the effect of their structure, surface, and mechanical properties.

CHAPTER IV

SCRATCH BEHAVIOR ON POLYMERIC LAMINATES

As presented in the introduction, polymeric laminates are extensively used in a wide variety of industrial value-added applications ranging from packaging [12] to electronics [13], biomedical [15], optical [18], flame retardants [21], sound absorbents [22], solar energy [23], and labels [25]. These applications are achieved by combining films with different characteristic properties to address specific industrial requirements.

Previous studies demonstrated the good barrier properties of polyamide (PA) films to oxygen [90], malodor gases [91, 92], and fuel vapor [93]. This makes them suitable for several applications such as packaging and transporting conduits for liquid fluids like alcohols and refrigerating fluids [93, 94]. Also, they have good performance at high temperature which makes them one of few polymers used to restore food while cooking and roasting [95]. However, one of their limitations is their poor moisture barrier properties [91]. This is not the case for hydrophobic PP films [96]. These films have characteristic barrier properties [97], and enhanced mechanical and thermal properties such as stiffness, strength, hardness, and temperature resistance [11, 98]. The good properties of PP and PA films are combined to manufacture PP/PA laminates, employed in many industrial applications like food packaging and photovoltaic modules [23].

In this chapter, we consider investigating scratch behavior on model polymeric laminates based on PA and PP systems. The scratch behavior on these systems was examined and the effect of film structure, surface, and mechanical properties is determined.

IV.1.EXPERIMENTAL

The model systems consist in PP film having a thickness of 65 μm, PA film with a thickness of 15 μm, and PP/PA and PA/PP laminates with a thickness of 80 μm. They were provided by Chengdu Xinhengtai Packaging Materials (China) and Unitika Group (Japan). Scratch tests were conducted to the films with accordance to the ASTM/ISO scratch standard described previously. The features of scratch damage were observed using VLSCM microscope presented in the introduction.

IV.2.FEM MODELING

The FEM model used previously in Chapter III was slightly modified to study scratch behavior on polymeric laminates. Representative constitutive and physical parameters of the studied materials were introduced. The constitutive behavior of the different materials is approximated by a piecewise linear stress-strain curve (Figure IV-1).

The main constitutive parameters are Young's modulus (E), yield stress (σ_y), softening slope (s), and hardening slope (h). The values of these parameters, as well as Poisson's ratio (ν) and density (ρ), are presented in Table IV-1 and supported with references from the literature. It is observed that the softening slopes of PA and PP are similar and take place over a short strain (ε) range (0.03 and 0.07, consecutively). Thus, this parameter will not be considered later in the comparison between PA and PP results.

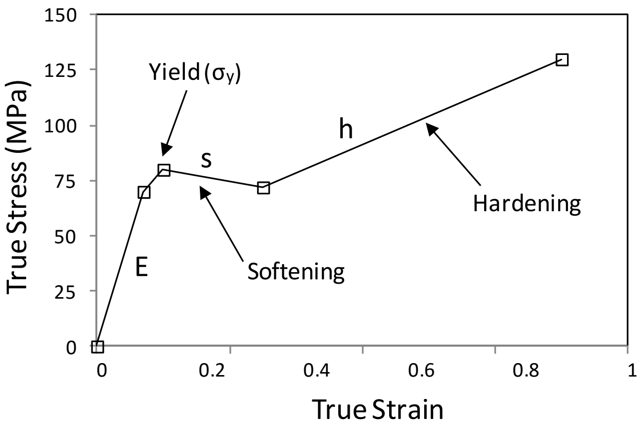

Figure IV-1. Typical piecewise linear stress–strain curve used for FEM modeling [9].

Table IV-1. Constitutive parameters introduced to the FEM model.

	E (GPa)	N	σy (MPa)	s (MPa)	h (MPa)	ρ (g/cm^3)	References
PP	1.65	0.42	35	-150	55, 200 **	0.9	[9, 53, 76, 99]
PA	2.82	0.35	70	-170	-20, 0 *	1.14	[100, 101]
Al	70	0.33	270	0	0	2.7	[75, 102-104]

* hardening slope changes at ε=0.24
** hardening slope changes at ε=1.03

IV.3.RESULTS AND DISCUSSION

IV.3.1.Surface and Subsurface Analysis

IV.3.1.1.Surface analysis

Figure IV-2 presents experimental COF measurements of PA and PP surfaces. They have values of 0.11 and 0.06, respectively. These values are low compared to bulk materials which might be due to processing-induced molecular orientation on the film surfaces. However, PA films still have higher COF than PP films. This difference in surface friction is expected to affect the scratch behavior of the studied model systems.

VLSCM visualizations of scratch damage features on the studied films and laminates are presented in Figure IV-3. The black scale bar below each scratch damage indicates scratch distance and direction. Also, representative transitional regions and their corresponding loads are highlighted in the figure. The maximum applied normal load in Figure IV-3a-d is 30 N and that in Figure IV-3e is 70 N. As shown in the figure, the observed scratch damage features include ironing, stick-slip, and tearing damages.

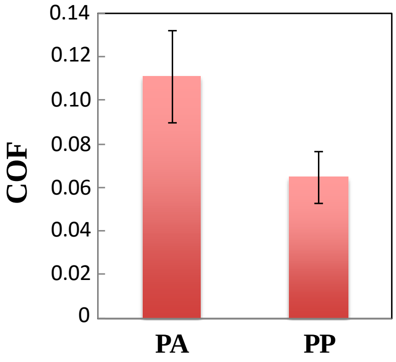

Figure IV-2. COF measurements of PA and PP surfaces.

Ironing usually involves a subtle compressive plastic deformation leading to groove formation and leads to a change in surface roughness at the beginning of scratch test. Usually, this faint damage affects the aesthetic properties of the films without a significant impact on their functional and structural integrity. Then, as the applied scratch load increases, a different repetitive sliding damage, namely stick-slip, takes place. Due to material deformation in front of the scratch tip and thus the increase in the frictional force, the tip sticks to the film surface (stick phase). Then, when the frictional and material resistance is lower than the imposed strain energy on the scratch tip, a sudden break occurs followed by a rapid slip motion (slip phase) [105]. Recently, Jiang and coworkers investigated the effect of stick-slip motion on the scratch performance of PP [106]. This phenomenon is responsible for the observed scratch visibility in PP. The transitional region in Figure IV-3 corresponds to the damage evolution between ironing and stick-slip, while the stick-slip region corresponds to an area with well-developed stick-slip damage. Finally, at sufficiently high loads, the ultimate failure of the films corresponds to tearing damage. The point at which the first puncture occurs is determined visually, and confirmed using the optical microscope. As shown in the figure, only ironing damage is observed on PP/PA laminates when the maximum applied normal load is 30 N (Figure IV-3d). Therefore, the load was increased to 70 N to obtain stick-slip and tearing damages on this laminate (Figure IV-3e).

The most detrimental damages in scratch are stick-slip and tearing damages. Figure IV-4 summarizes the onset loads of these damages for the four model systems. In this figure, higher load indicates a better resistance to the corresponding damage. It is found that PA films have the lowest stick-slip and tearing resistance with onset loads of 8.7 N and 13 N, respectively. The resistance to both damages is higher in PP film with stick-slip and tearing loads of 13.5 N and 30 N, respectively. This difference between PA and PP films is better observed in Figure IV-3a and Figure IV-3b where scratch damage quickly changed from ironing to stick-slip motion in PA.

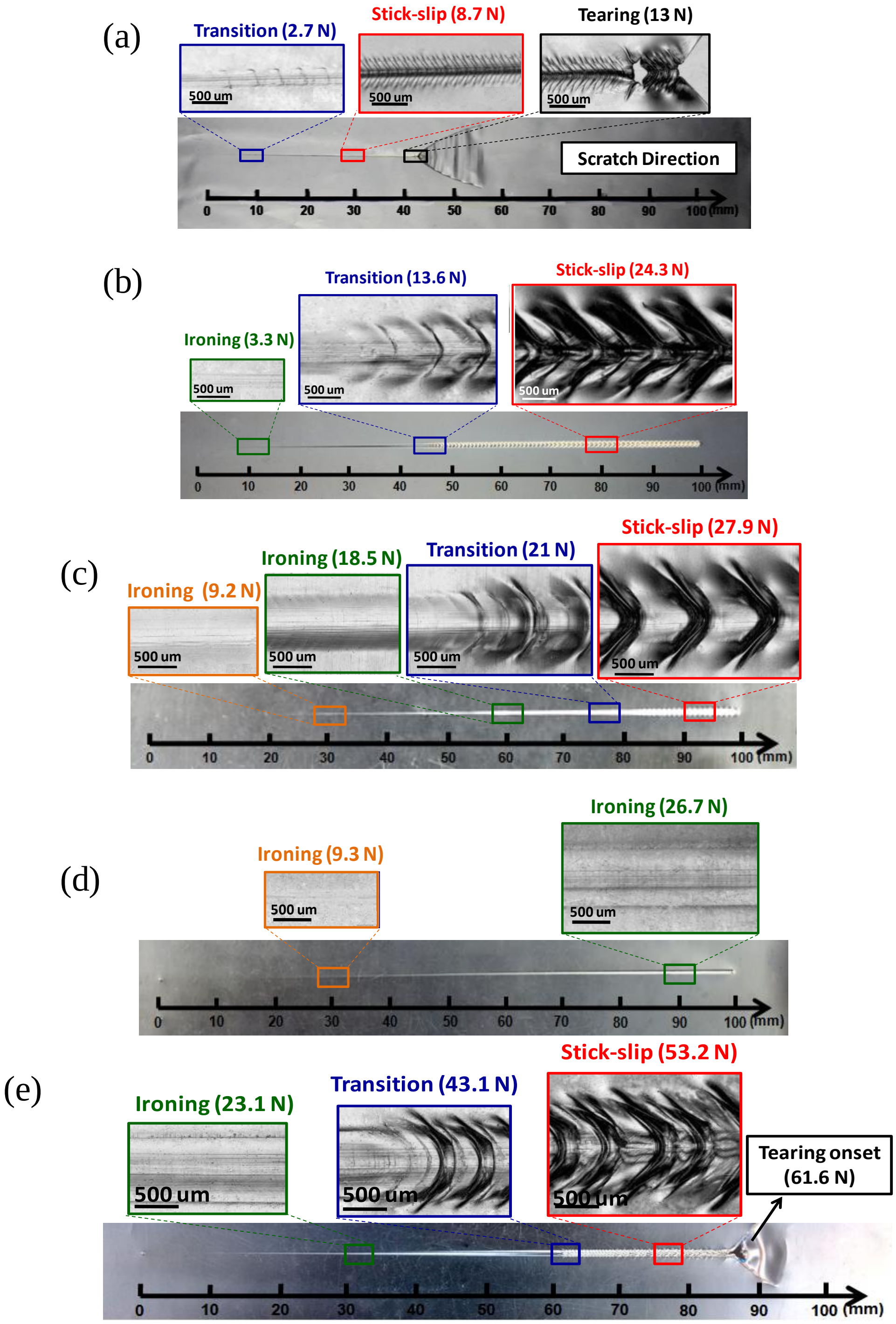

Figure IV-3. Scratch features on (a) PA [L=30 N] (b) PP [L=30 N] (c) PA/PP [L=30 N] (d) PP/PA [L=30 N] (e) PP/PA [L=70 N].

Also, the figures show that the adjacent stick patterns are more distant from each other in the case of PP films, reflecting a better scratch performance [105]. However, it is crucial to consider that PA films are much thinner than PP films [μ (PA) = 15 μm, μ (PP) = 65 μm]. This significantly affects the difference in their scratch resistance, and therefore a straightforward comparison between the two films cannot be made. This limitation is avoided in PA/PP and PP/PA laminates which both have the same thickness of 80 μm.

Figure IV-4 shows that both laminates have considerably higher stick-slip and tearing resistance than individual PA and PP films. Particularly, loads as high as 43 N and 62 N are required to cause stick-slip and tearing damages on PP/PA laminate. This indicates that PP/PA has better scratch performance than PA/PP laminate. In fact, the comparison between Figure IV-3c and Figure IV-3d shows that for the same applied load of 30 N, well-developed stick-slip patterns were obtained for PA/PP laminates, while only ironing damage occurred on PP/PA laminate. The low scratch resistance of PA/PP laminate is partially caused by the higher friction of PA surface compared to PP surface (Figure IV-2). This effect was demonstrated previously where higher surface friction caused lower scratch resistance [49, 105].

As will be shown later, a characteristic feature of stick-slip patterns in scratch damage is material folding in front of the scratch tip during the stick motion. Thus, the frictional load increases significantly. However, this phenomenon is not considered in the measurement of surface COF where flat tip is used and low normal load is applied. Therefore, *scratch coefficient of friction* (SCOF) is another tribological parameter that can be determined to consider both intrinsic surface friction and large-scale material deformation. It is defined as the ratio of the tangential load to the normal load at a certain scratch position. Figure IV-5 presents a comparison between the SCOF values of PA and PA/PP (Figure IV-5a), PP and PP/PA (Figure IV-5b), and PA/PP and PP/PA (Figure IV-5c) across the scratch distance. In this figure, three curves are presented for each system, and the maximum applied scratch load is 30 N. The considerably high fluctuations at the beginning of each curve are due to the inertia effect after the sudden speed change of the scratch tip from 0 to 100 mm/s. Figure IV-5a shows that PA and PA/PP systems have similar SCOF values at the beginning of scratch test. The stick-slip transition of thin PA film did not change considerably its SCOF value. However, after PA tearing, the scratch tip is in direct contact with the aluminum backing and its SCOF changes significantly. Usually, stick-slip oscillations affect the SCOF curve by increasing its value and causing severe fluctuations which is the case of PA/PP after stick-slip onset.

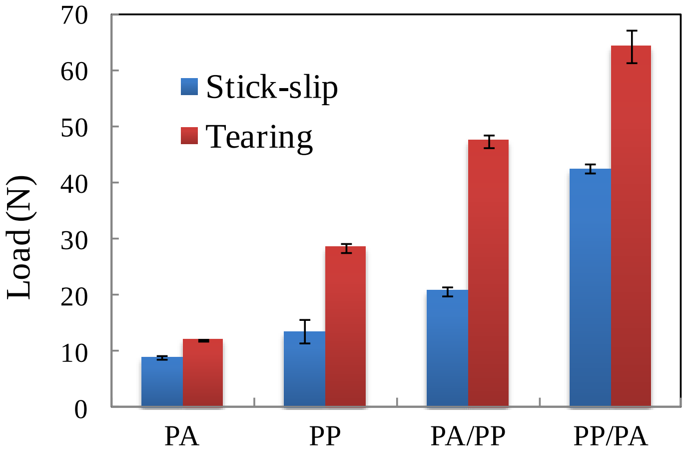

Figure IV-4. Stick-slip and tearing onset loads of the studied films and laminates.

Similarly, the SCOF curves of PP films coincide with those of PP/PA laminate at the beginning of scratch test (Figure IV-5b). After the onset of stick-slip damage in PP films, their SCOF increases slightly. It is observed that the increase of surface SCOF after the onset of stick-slip behavior is proportional to the thickness of the films. This is explained by the fact that for thicker systems, more material can be folded in front of the scratch tip which increases the tangential load and hence the SCOF. In Figure IV-5c, the SCOF of PA/PP is clearly higher than that of PP/PA since the beginning of scratch test. This result is explained by the high COF of PA surfaces compared to that of PP surfaces (Figure IV-2). This difference in SCOF is more pronounced after the onset of stick-slip motion in PA/PP. Unlike PA/PP, no severe fluctuations are observed in the SCOF curve of PP/PA. This indicates the absence of stick-slip oscillations on this laminate up to 30 N.

IV.3.1.2.Subsurface analysis

Longitudinal and cross-sectional images were taken using VLSCM to examine subsurface damages. In Figure IV-6, the ability of PP film to fold during stick-slip damage at the transitional region is presented. The figure shows that material folding is significant since the beginning of stick-slip damage. In fact, at the third stick pattern, the height of the dragged material is already over 400 μm (Figure IV-6b-2). Although not shown here, stick-slip patterns are considerably lower in the transitional region of PA films. This difference is explained by the high thickness and the low yield stress of PP films compared to PA films (Table IV-1). An advantage of the scratch tests carried out on polymeric laminates is the ability to learn about the associated damage at a film layer level. This allows us to determine how each layer contributes to the resistance of scratch damage.

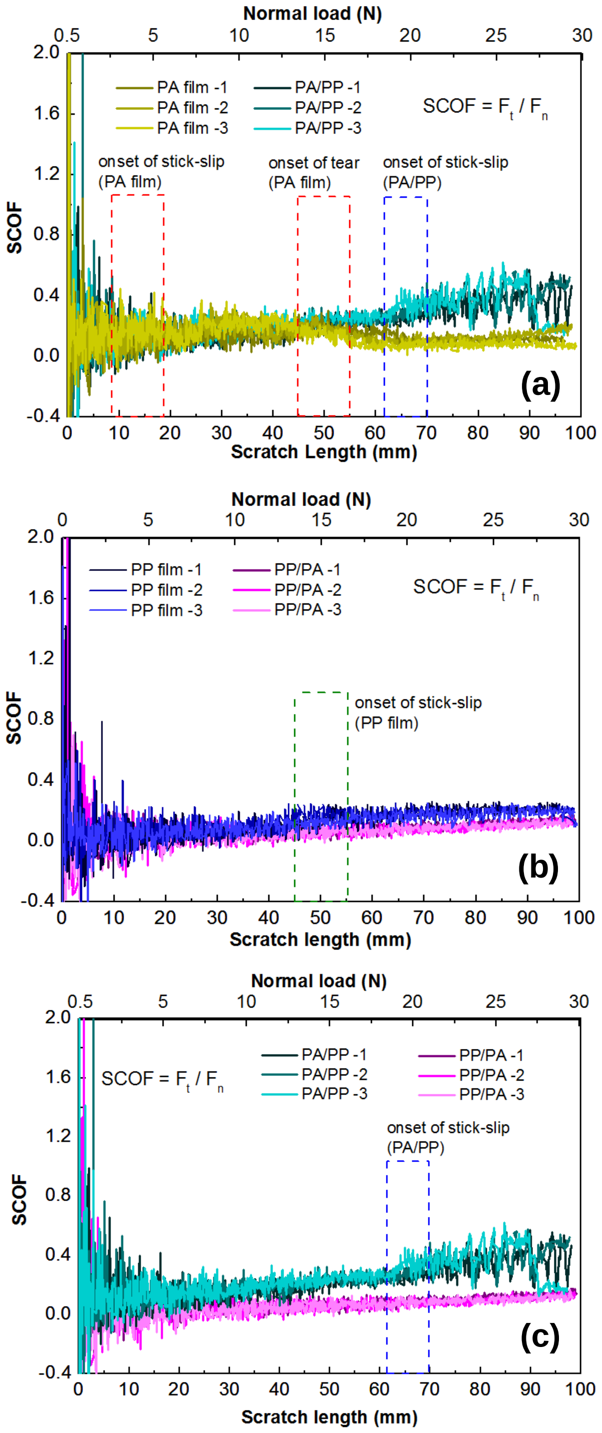

Figure IV-5. SCOF of (a) PA and PA/PP (b) PP and PP/PA (c) PA/PP and PP/PA [L=30N].

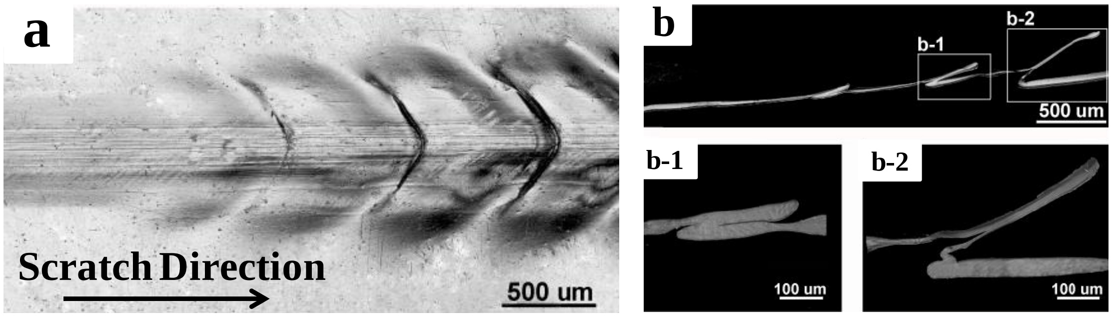

Figure IV-6. Transitional region of PP film: (a) surface section (b) corresponding longitudinal subsurface section (b-1) and (b-2) zoomed subsurface sections.

In Figure IV-7, a comparison between PA/PP (Figure IV-7a-b) and PP/PA (Figure IV-7c-d) laminates is shown. For each laminate, both transitional region and developed stick-slip region are presented. Also, for each image, the surface view is shown on the top and its corresponding longitudinal subsurface view is shown on the bottom. Longitudinal views demonstrate that stick-slip patterns are associated with laminate tearing and detachment from the aluminum backing beneath the scratch tip (Zone I), followed by laminate dragging and folding in front of the scratch tip (Zone II). The two zones first appear in transitional regions, then become more significant with well-developed stick-slip patterns. It is observed in the longitudinal views that Zone I and Zone II are significant and well-developed in the case of PA/PP (Figure IV-7a-b), but confined and suppressed in the case of PP/PA (Figure IV-7c-d). The difference in Zone II between the two laminates is consistent with that in SCOF (Figure IV-5c): PA/PP laminate, with higher material folding, has higher SCOF. This is explained by the high COF of PA surface (Figure IV-2).

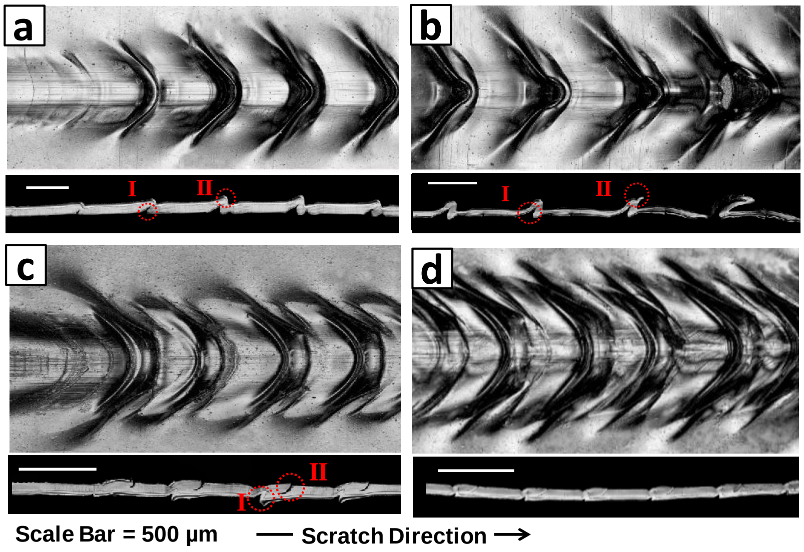

Figure IV-7. (a) Transitional region on PA/PP (b) Stick-slip region on PA/PP (c) Transitional region on PP/PA (d) Stick-slip region on PP/PA.

For a better visualization, we consider tracking the formation of stick-slip patterns in different scratch regions. Figure IV-8 shows longitudinal microscopic images of scratch deformation regions on PA/PP (Figure IV-8a-b) and PP/PA (Figure IV-8c-e) laminates. Similarly, Zone I, Zone II, and Zone III in this figure correspond to material tearing and detachment from the Al backing, material dragging and folding in front of the scratch tip, and interlayer damage, respectively. The difference in material folding (Zone II) between the two laminates is even clearer in this figure. It is observed by comparing Figure IV-8-a to Figure IV-8-c, and Figure IV-8-b to Figure IV-8-d. The tearing damage of PP/PA laminate shown in Figure IV-8-e demonstrates that PA layer is completely damaged before PP layer (Zone III). This is due to high interface and interlayer stresses as will be better explained later in the FEM analysis.

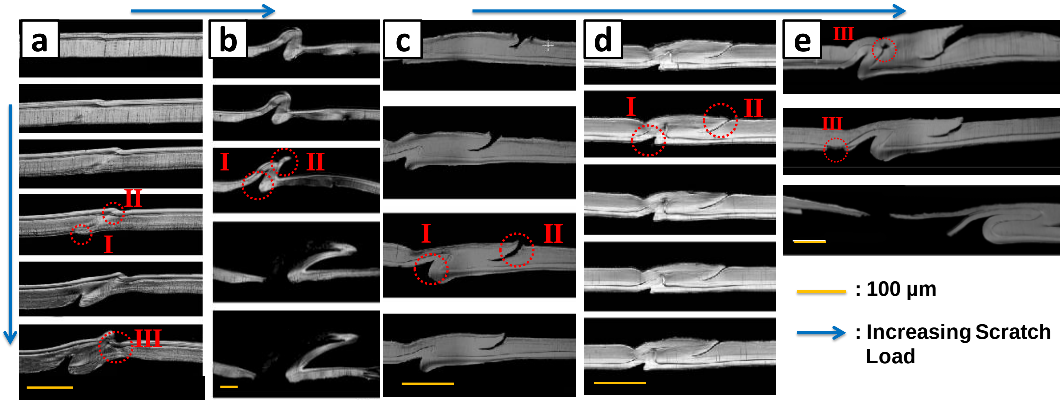

Figure IV-8. (a) Transitional region on PA/PP (b) Stick-slip region on PA/PP (c) Transitional region on PP/PA (d) Stick-slip region on PP/PA (e) Tearing region on PP/PA.

After examining surface and longitudinal views of the scratch damage, better insight is gained on scratch-induced deformation by observing its cross-sectional views. Figure IV-9 presents the cross-sectional views of PA/PP and PP/PA laminates at the transitional region. It shows the increase of scratch width along the first stick-slip patterns. It is observed that the scratch in PP/PA (Figure IV-9b) is wider than that in PA/PP (Figure IV-9a) at the transitional region. Also, more material is folded on the side of the scratch tip (Zone IV) in the case of PP/PA laminate than the case of PA/PP laminate. Our previous results show that material folding in front of the scratch tip is suppressed in the case of PP/PA laminate (Figure IV-7). Instead, more material is folded on the tip side for this laminate and scratch deformation extends in the width direction. The experimental analysis shows that the model films and laminates have different responses to scratch test. It is demonstrated that PP/PA has better scratch performance than PA/PP. This is partially explained by the difference in their friction values. The difference in laminate structure is also expected to have a significant impact on the stress distribution, and thus on the scratch-induced deformation. We consider investigating the characteristics of the structures of the studied laminates and how they affect the scratch behavior.

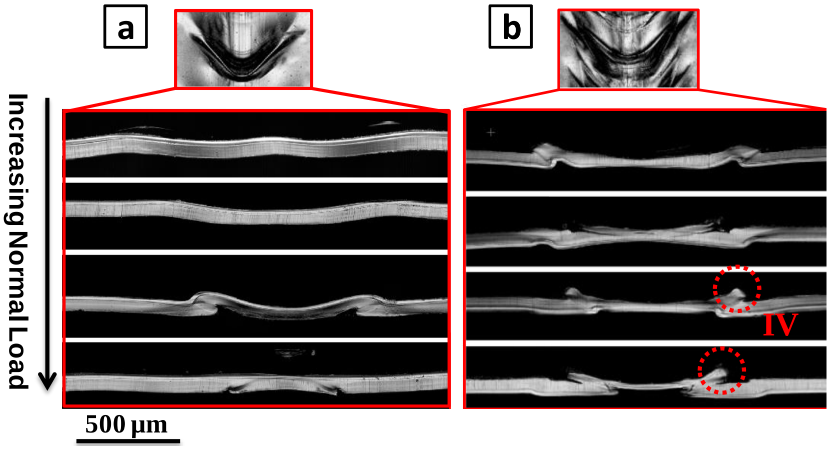

Figure IV-9. Cross-section images of the transitional region on (a) PA/PP (b) PP/PA.

IV.3.2.Graded Materials (GMs)

IV.3.2.1.Background and case study

Graded materials are non-homogeneous materials with a gradually changing property (*gradient*) usually in the thickness direction. They can be tailored by altering the volume fractions of their constituents either continuously or discontinuously. Continuous material gradation is performed according to a predetermined composition profile, resulting in a functionally graded material (FGM) [107]. Polymeric FGMs can be obtained by spatially changing their degree of crystallinity and/or molecular weight [108]. Discontinuous stepwise material gradation is made in a piecewise constant manner using bonded dissimilar homogeneous materials, resulting in a multi-layered medium [108]. Inspired by their presence in nature [108], researchers introduced GMs in a variety of engineering applications as diverse as microelectronics, magnetic storage media, bio-implants, load-bearing structures, protective coatings, and nano- and micro-electromechanical systems, to "blur" sharp interfaces and abrupt transitions in thermal, mechanical, and physical properties mismatch [109]. As a result, the overall properties are enhanced after grading.

GMs were initially introduced for thermal shielding applications to redistribute and reduce thermal stress [110-112]. The material gradient (i.e. changing property) in this case can be thermal expansion [112]. They were also used in biomechanical devices where biocompatible materials were gradually infiltrated into implants for a better biocompatibility [108]. Yet, the most common application of GMs currently is tribology. They are widely employed to improve resistance to tribological damages in high-performance components such as case-hardened gears and bearings used in jet and rocket engines [107, 113]. In this particular mechanical application, the material gradient consists of a mechanical property that can be either elastic (E, ν) or plastic (σ_y, h ...).

We consider examining the mechanical properties of the model laminates based on the FGM concept presented above. According to Table IV-1, several properties change gradually when the materials are ordered as PP, PA, then Al, i.e., in the case of PP/PA laminate on the Al backing. This observation is better presented in Figure IV-10.

Therefore, PP/PA laminate can be considered as elastic, plastic, and density-graded material. This is not the case for PA/PP laminate. This difference between the two laminates is expected to strongly affect their scratch performance. To have a better insight, we consider investigating the effect of each gradient, with other parameters kept the same, on the tribological performances.

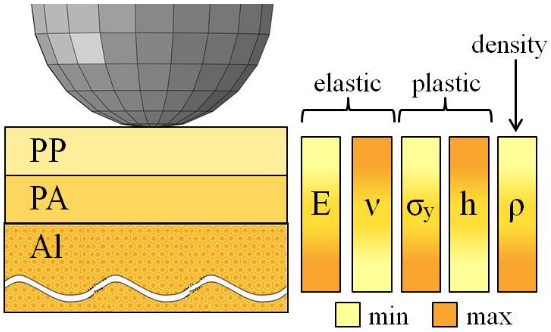

Figure IV-10. Gradients in the graded structure of PP/PA laminate on Al backing.

IV.3.2.2.Elastically GMs

It was demonstrated previously that mismatch in film-substrate modulus plays a significant role in film indentation failure [114]. Therefore, elastically GMs with blurred interfaces present a promising solution to overcome abrupt changes in modulus at interface. Several analytical approaches were adopted to approximate the modulus change with depth in such materials: the geomechanics community approximated the earth surface to an elastically graded surface using a power-law relation (Equation 1), where E_0 is the reference elastic modulus at the surface and k is the non-homogeneity parameter [115].

The same relation was later employed to characterize elastically GMs [115]. In other studies, the elastic modulus follows an exponential variation with depth (Equation 5), where α is a characteristic length [115, 116].

$$E = E_0\, z^k \quad 0 \leq k < 1 \qquad (4)$$

$$E = E_0\, e^{\alpha z} \qquad (5)$$

Using these analytical expressions, as well as numerical and experimental tests, previous studies compared elastically GMs with increasing modulus with depth (soft-to-stiff) to their corresponding homogeneous materials. Results demonstrate that they exhibit greatly enhanced resistance to indentation Hertzian crack damage [116-118], improved resistance to frictional sliding herringbone contact damage [119], and better fracture toughness [107] compared to their homogeneous counterparts. However, indentation resistance is decreased for elastically GMs with the opposite sequence, i.e., decreasing modulus with depth (stiff-to-soft) [116]. Also, it was found that the propensity for brittle crack formation and the onset of plastic flow decrease with increasing E with depth beneath the spherical indentation tip [120]. Therefore, it was concluded that, compared to homogeneous materials, the ‘‘*apparent*’’ ductility of elastically GMs beneath the indentation tip is enhanced when E increases with depth, and reduced when E decreases.

All these previous studies demonstrate that the tribological performances of homogeneous materials are enhanced in the corresponding elastically GMs with increasing stiffness along the depth. This is consistent with our experimental findings. In fact, our results show that PP/PA laminate on Al backing, considered as an elastically GM with increasing E with depth (Figure IV-10), has better scratch performance than PA/PP laminate, which is a non-graded material (Figure IV-4). As for Poisson's ratio gradation, it was previously demonstrated that the gradation of this parameter has little influence on GMs [116, 121]. Therefore, it will not be examined in our analysis.

IV.3.2.3.Plastically GMs

Plastically GMs are still relatively unexplored compared to elastically GMs. This is due to the challenging processing of materials with controlled plastic gradients and the complex characterization of plastic deformation over a region with varying plastic properties [108]. With regards to plastically GMs with changing yield stress, previous studies showed that when σ_y increases with depth, indentation stiffness increases and residual tensile stress is suppressed compared to similar homogeneous materials, vice versa is also true for the opposite case [108, 122]. Residual tensile stress is responsible for radial and lateral cracking, delamination, and excessive plastic deformation. As for strain hardening slope, Giannakopoulos conducted an analytical and experimental analysis on the indentation response of GMs with changing strain hardening slope [122]. Results show that when strain hardening slope decreases with depth, tensile stress near the contact boundary decreases. Therefore, indentation resistance increases and radial cracking at loading is suppressed [122]. These results are in good agreement with our experimental findings, as well. In fact, PP/PA laminate on Al backing, considered as a plastically GM with increasing yield stress and decreasing strain hardening with depth, has better scratch performances than non-graded PA/PP laminate.

IV.3.2.4.Density-graded foams (DGFs)

A few studies were also conducted on polymeric multilayered DGFs. These foams are frequently used as cushioning materials in automotive industries and core materials in lightweight sandwich structures to enhance energy absorption [123]. Studies were recently performed on polymeric multilayered DGFs with increasing density with depth. It was found that they have significantly higher energy absorption and load-bearing performances under compression compared to uniform foams [124, 125]. Also, they have better blast resistance [126], and relatively higher energy absorption under high applied loads (which is the case of our scratch test) [127] than polymeric multilayered DGFs with decreasing density with depth. These results were obtained for different polymeric multilayered DGFs, including PP foams as demonstrated in [128] where impact tests were conducted.

In our study, PP/PA laminate on Al substrate is considered as a multilayered density-graded system with increasing density with depth (Figure IV-10). According to the literature, this characteristic structure enhances energy absorption during the scratch test. The increase in energy absorption capabilities may explain the improvement of the scratch performance of this laminate. A better insight on the impact of material grading on scratch behavior, will be further gained using the FEM analysis.

IV.3.3.FEM Modeling

The main advantage of the FEM model is the ability to obtain stress and strain distributions on the surface and at the interface of the model laminates. Frictional stress (σ_F) and tensile stress (σ_N^T) are indicative parameters of surface damages involving increase in volume, such as crazing, cracking, voiding, debonding, etc [109]. Figure IV-11 presents the highest values of instantaneous σ_N^T and σ_F beneath the scratch tip for each applied scratch load. Stress values were obtained on the laminate surface (Figure IV-11a) and at the laminate-backing interface (Figure IV-11b) of PA/PP and PP/PA laminates.

IV.3.3.1.Stress analysis near surface

It is reported that σ_N^T plays an important role in tribological damages [109]. In our case, σ_N^T is responsible for laminate detachment from the backing material. Figure IV-11a shows that peak σ_N^T on the surface of PA/PP is much higher than that on PP/PA surface. Assuming perfect interfacial adhesion and infinite strength for PA and PP, then σ_N^T at the interface increases significantly to reach about 230 MPa by the end of the scratch test, while σ_N^T of PP/PA is almost constant across the scratch test and does not exceed 10 MPa.

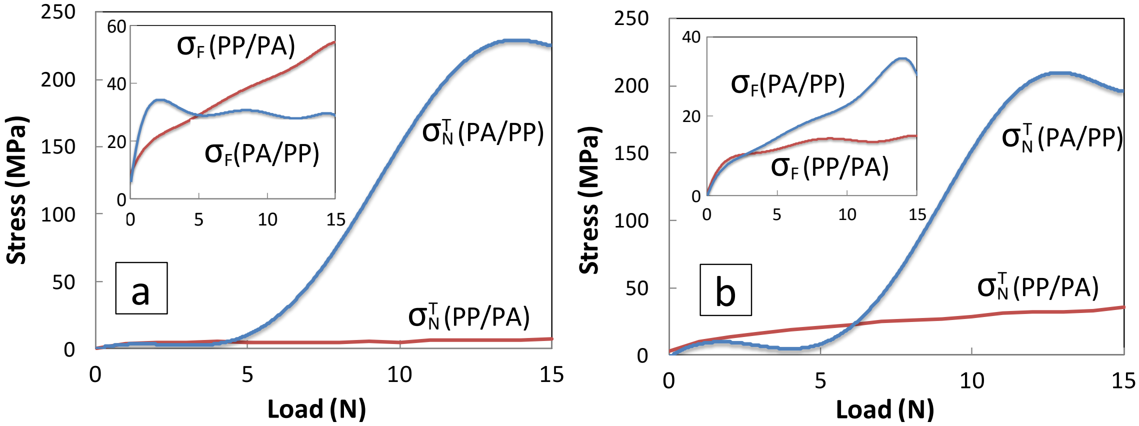

Figure IV-11. Peak frictional (σ_F) and tensile normal (σ_N^T) stress values of (blue) PA/PP and (red) PP/PA laminates (a) on the surface and (b) at the laminate-backing interface.

This difference in σ_N^T explains the significant scratch damage observed on PA/PP laminate. Peak σ_F also behaves differently on the top surfaces of the two laminates (Figure IV-11a). While σ_F of PA/PP quickly reaches a plateau of about 30 MPa, σ_F of PP/PA keeps increasing gradually and becomes higher at a load of approximately 6 N. This result is unexpected since PA surfaces have higher COF values (Figure IV-2). However, σ_F also increases with higher contact between the scratch tip and the film surface. The contact area between the scratch tip and the laminate surface is governed by the scratch groove dimensions, namely, groove shoulder height, depth, and width. To verify the difference in contact area between the two laminates, scratch dimensions beneath the scratch tip were measured (Figure IV-12). Results show that scratch groove shoulder height is larger on PA/PP for each applied normal load. This is consistent with our experimental findings where intensive stick-slip patterns (Figure IV-7 and Figure IV-8) and higher SCOF (Figure IV-5c) were obtained for this laminate. However, PP/PA has higher scratch width and depth. This result is also consistent with experimental width measurements at the transition scratch region (Figure IV-9). High PP/PA scratch groove dimensions are explained by the low modulus and yield strength values of the top PP layer (Table IV-1), making this latter more susceptible to fold as shown in Figure IV-6. Consequently, PP/PA laminate exhibits more significant scratch width and depth, thus a larger contact area. This explains the increase in σ_F on its surface (Figure IV-11a). It is also observed that the load at which scratch width and depth become higher for PP/PA is approximately 6 N (Figure IV-12). This is the same load at which σ_F becomes higher for this laminate (Figure IV-11a). This observation demonstrates the direct correlation between σ_F and contact area.

Also, at a sufficiently high load, the depth curve of PA/PP laminate shows severe fluctuations indicating stick-slip motion. This behavior is not observed in PP/PA depth curve. This difference in FEM depth curves is consistent with our experimental findings. For the same applied load, periodic stick-slip patterns were obtained for PA/PP (Figure IV-3c), while only ironing damage was observed on PP/PA (Figure IV-3d).

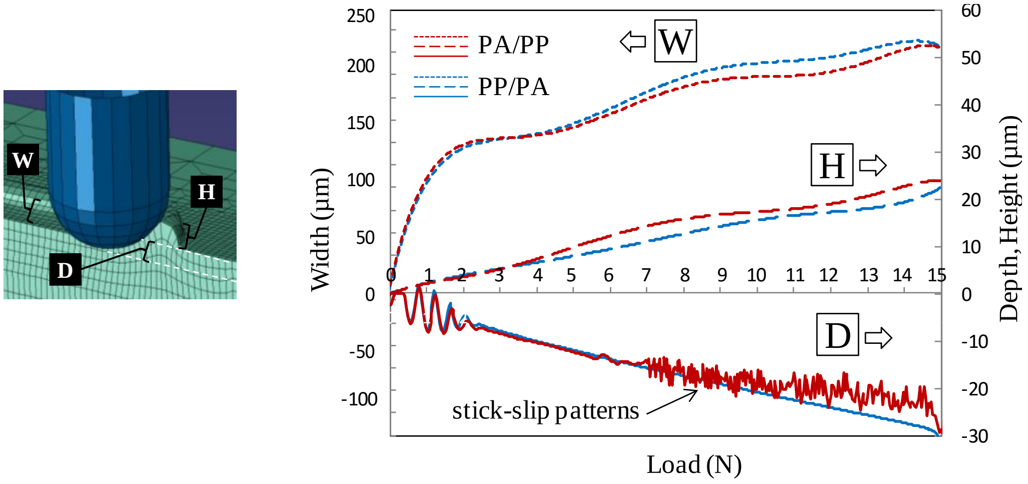

Figure IV-12. Scratch width (W), height (H), and depth (D) on PA/PP (red) and PP/PA (blue) laminates.

Other than peak stress values, it is crucial to examine stress and strain distributions to better understand scratch behavior. Figure IV-13 shows the distributions of maximum principal plastic strain (ε_{pp}^{max}), maximum principal stress (σ_{pp}^{max}), and normal stress (σ_N) on the surface of PA/PP and PP/PA laminates at the end of the scratch test before elastic and plastic recovery have taken place (L=15 N). The scratch tip was removed for a better visualization and its position is indicated by an arrow. Figure IV-13 clearly shows high and low ε_{pp}^{max} areas on the surface of PA/PP laminate reflecting stick-slip patterns observed experimentally. Stick and slip regions with high and low plastic strain, respectively, are highlighted in the zoomed area of this figure. However, ε_{pp}^{max} distribution is low, smooth, and continuous on PP/PA surface, indicating ironing damage. Therefore, the strain distribution on PA/PP and PP/PA laminates is consistent with scratch damage features observed experimentally. Similar observation is made for σ_{pp}^{max} and σ_N distributions.

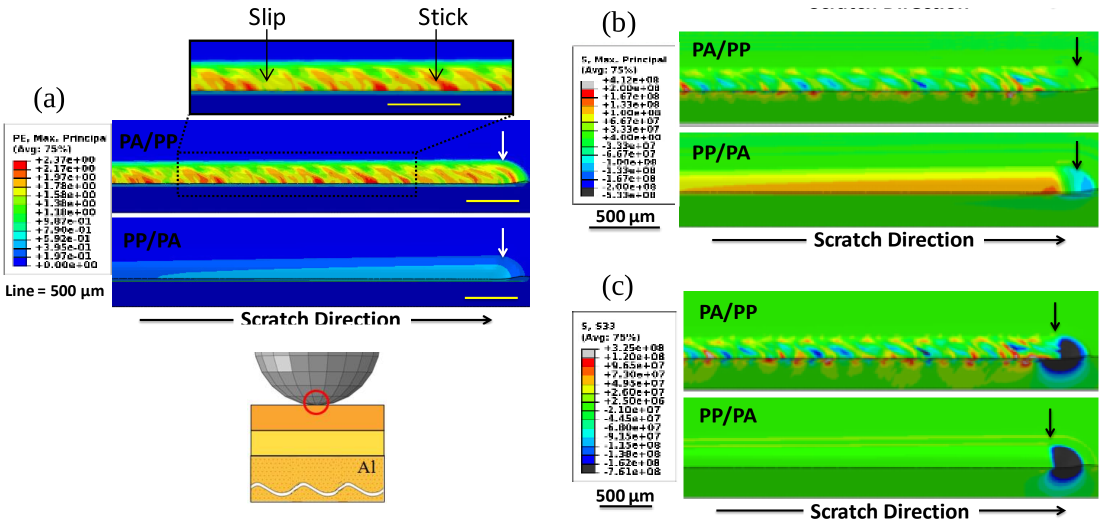

Figure IV-13. (a) ε_{pp}^{max} (b) σ_{pp}^{max} and (c) σ_N distributions on the surface of PA/PP and PP/PA laminates (L=15 N).

In sliding contact damages, a higher principal stress corresponds to a more severe damage [118, 129]. Although discontinuous, higher σ_{pp}^{max} values are obtained on the surface of PA/PP laminate. This is explained by the strong and stiff behavior of upper PA layer. This result is consistent with the experimental findings demonstrating significant scratch damage on this laminate. Similar results are obtained for σ_N, which is responsible for the laminate detachment from the backing material.

The surface analysis shows a good agreement between experimental and FEM results. Scratch features observed experimentally on the surface of the laminates, namely stick-slip and ironing damages, are well-captured using the FEM model. Severe damage on PA/PP surface is caused by high principal and normal stress magnitudes.

IV.3.3.2.Subsurface analysis

The contact between the laminate film and the backing aluminum plays a major role in scratch behavior. Previous studies demonstrated the importance of interfacial stresses on interfacial damage which is usually initiated at the interface and then propagated to the top surface [84-87]. This will be better determined by studying the subsurface stress and strain distributions. Figure IV-11b presents the instantaneous peak σ_F and σ_N^T values at the laminate-backing interface for a given applied scratch load. It is observed that σ_N^T is higher than shear stress at the interface, especially for PA/PP laminate. This result is consistent with a previous study on the interface failure of plastic packaging [130]. This study shows that interfacial debonding is mainly caused and controlled by interface normal stress which is much higher than interface shear stress [130]. Higher interfacial shear strength is explained by the role played by surface roughness for mechanical interlocking in shear loading [107, 130]. Also, a slight drop is observed in the σ_N^T curve of PA/PP at the beginning of scratch test. This drop may be related to stick-slip behavior on this laminate.

It is also observed in Figure IV-11b that PP/PA laminate has considerably lower interfacial σ_F than PA/PP. This is explained by the elastically and plastically graded structure of PP/PA. It was demonstrated previously that a subsurface with gradual and smooth stiffness has lower shear stress, lower strain energy, and better fracture toughness at the interface [107]. It was also shown that when plastically GMs are utilized, interfacial shear stress at critical locations is reduced in peak and in distribution and the onsets of plastic deformation and cracking are suppressed [110, 111].

To have a better insight on the difference in interfacial stress between the two laminates, von Mises stress distributions beneath the scratch tip are shown in Figure IV-14. Two different loads, L= 7 N (Figure IV-14a-b) and L = 15 N (Figure IV-14c-d), are considered for illustration. For a better visualization, the tip is removed and replaced by a black arrow, the laminate-backing interface is indicated by a white line, and cross-sectional views are shown for L=15 N (Figure IV-14e-f).

It is observed that areas with high stress concentration are transmitted to the laminate-backing interface in the case of PA/PP laminate (Figure IV-14a, Figure IV-14c, and Figure IV-14e). This increases the laminate-backing stress mismatch and facilitates laminate delamination. This observation explains previous PA/PP results showing the higher interface tearing and detachment (Zone I in Figure IV-7 and Figure IV-8) and lower scratch resistance (Figure IV-4) of this laminate. Therefore, in PP/PA laminate, PA layer shields the laminate-backing interface from high stress build-up. This is achieved thanks to the high modulus and yield stress values of PA (Table IV-1).

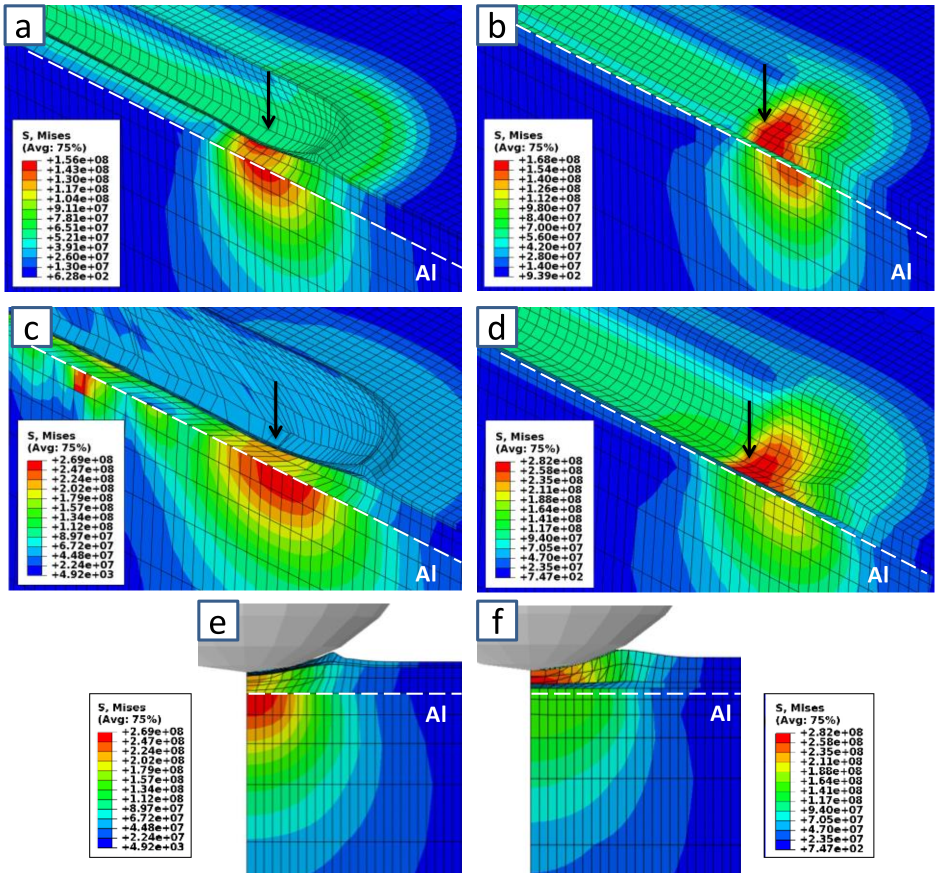

Figure IV-14. von Mises stress beneath the scratch tip (a) PA/PP [L = 7 N] (b) PP/PA [L = 7 N] (c) PA/PP [L = 15 N] (d) PP/PA [L = 15 N] (e) PA/PP [L = 15 N] (f) PP/PA [L = 15 N].

However, this is not the case for PP/PA laminate, where high stress concentration area is confined on the top surface. This laminate has higher surface deformation as shown in Figure IV-12. Also, the comparison of scratch grooves on the two laminates in Figure IV-14 shows that scratch deformation flattens quickly on PA/PP but more gradually and broadly on PP/PA. It is concluded that top PP layer in PP/PA, susceptible to higher stress and higher deformation, absorbs more scratch energy than top PA layer in PA/PP. Given PP/PA on the aluminum backing is considered as a density-graded material with increasing density along the depth, this observation is consistent with what has been observed in the ability of density-graded polymeric foams with increasing density along the depth to absorb more energy [123, 127, 128].

To better examine the shielding property of PA layer, we consider comparing stress distribution across the interfaces of PP and PP/PA systems (Figure IV-15). Figure IV-15a and Figure IV-15c show significant stress concentration area at the interface of PP-Al backing just beneath the scratch tip. This area is considerably reduced after the addition of PA layer between PP film and the backing (Figure IV-15b and Figure IV-15d). This result highlights the role played by PA layer in limiting high stress area to the surface and avoiding interfacial damage. It explains our experimental findings, where material detachment and folding in PP film (Figure IV-6) become considerably localized and suppressed in PP/PA (Figure IV-7c-d).

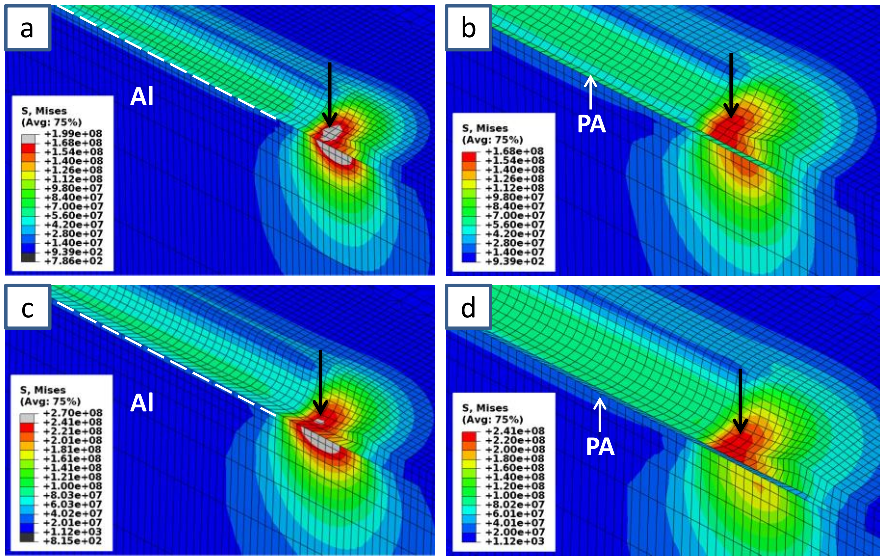

Figure IV-15. von Mises stress distribution beneath the scratch tip on (a) PP [L = 7 N] (b) PP/PA [L = 7 N] (c) PP [L = 12 N] (d) PP/PA [L = 12 N].

A surface cut was made exactly at the laminate-backing interface level to better visualize the distribution of interfacial σ_{pp}^{max} in both laminates (Figure IV-16). Scratch onset is indicated by a white arrow and tip position is indicated by a yellow arrow. Images with higher resolution are presented on the right side of the figure. Again, severe stress fluctuations are observed at the interface in the case of PA/PP laminate reflecting stick-slip behavior, while smooth, continuous, and low stress distribution is obtained for PP/PA indicating ironing damage. Also, high tensile σ_{pp}^{max} observed on PA/PP explains the quick detachment of this laminate from the backing material.

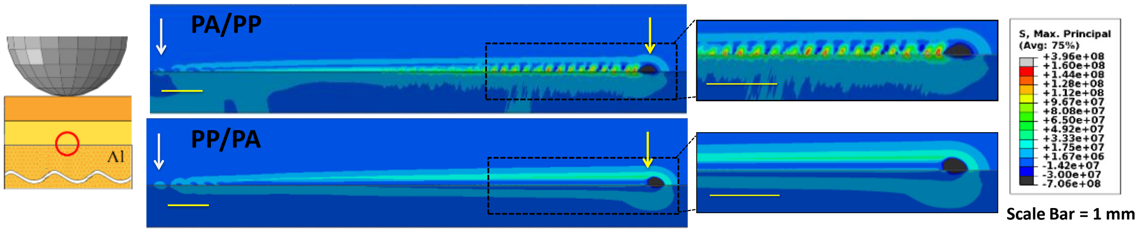

Figure IV-16. σ_{pp}^{max} distribution at the laminate-backing interface (L=15 N).

Also, PA-PP interlayer interface should be examined. Figure IV-17 presents a top view of interlayer σ_{pp}^{max} distribution at this interface. Again, σ_{pp}^{max} distribution is discontinuous in the case of PA/PP and smooth in the case of PP/PA. Also, tensile and compressive σ_{pp}^{max} between PA and PP layers are higher for PA/PP. Our experimental results show that, at the transitional region, interlayer damage area appears in PA/PP laminate but not PP/PA laminate (Zone III in Figure IV-8). Thus, experimental and FEM results are in good agreement.

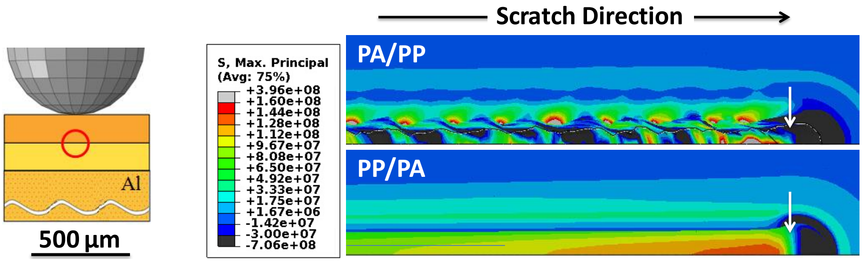

Figure IV-17. Top view of interlayer σ_{pp}^{max} distribution beneath the scratch tip (L=15 N).

The results presented in this chapter are directly related to different industrial applications where polymer laminates are extensively used. For instance, the scratch damages investigated here accurately simulate field scratch damages observed on labels and food and electronics packaging laminates. These real-case scenarios are studied thanks to the versatility and effectiveness of the scratch test that is able to accommodate different test conditions, obtain meaningful and repeatable results, and conduct a layer level analysis. Using this test, our study demonstrates that laminate structure plays a crucial role in altering stress distribution on the surface and most importantly throughout the laminate cross-section. Unlike bulk materials, when stress concentration area is transmitted from the surface to the inner part of a laminate-backing system, more interface damages take place. This can be avoided by decreasing the surface friction and introducing elastic, plastic, and density-graded structures. Considering these results in the design of polymeric laminates and selecting the appropriate laminate structure for each industrial application will significantly improve scratch resistance.

IV.4.CONCLUSION

In this chapter, we investigate the scratch behavior of a set of model polymeric films and laminates. The standardized ASTM/ISO test and numerical FEM modeling were employed to establish guidelines for preparing scratch-resistant laminated films for a variety of packaging applications. Results show that PA/PP has considerably lower scratch resistance than PP/PA. Microscopic observations show more severe material detachment and folding in PA/PP laminate. This result is attributed to the low friction of top PP surface in PP/PA laminate. Also, it is partially explained by its elastic, plastic, and density-graded structure. These experimental findings are supported by the FEM analysis. Scratch dimensions and patterns are well-captured using the FEM modeling. Good PP/PA scratch performance is explained by the ability of top PP layer to absorb scratch energy, and stronger bottom PA layer to shield the interface from stress build-up. The numerical results also demonstrate that frictional, normal, and maximum principal stresses on the surface and at the interface are significantly suppressed in PP/PA laminate. Better understanding on the scratch behavior of polymeric films and laminates is gained through this model systems study.

Chapter III and Chapter IV focus on the scratch behavior on polymeric films and laminates. With the current available capabilities of materials synthesis and processing, more avenues are open for the design of new polymeric films and laminates with appealing scratch performance. This can be achieved by increasing film orientation, lowering surface friction, improving interfacial strength, and employing graded structures. We consider now studying mar on bulk polymeric materials to gain a better insight on the behavior of this common subtle damage. The impact of major perceptual attributes, namely brightness, transparency, and color on mar visibility resistance is determined in Chapter V.

CHAPTER V

EFFECT OF PERCEPTUAL PROPERTIES ON MAR RESISTANCE

As highlighted in the literature review, studying the effect perceptual attributes on mar visibility resistance of polymeric systems is significantly valuable. The experimental results are more reliable when validated with psychophysical tests. For more consistent results, the analysis of these tests should be based on recognized statistical techniques, such as *multidimensional scaling (MDS)*. MDS is an exploratory data analysis technique designed to unveil the "hidden dimensions" in the organization of data. This technique displays the most important relationships and inferences in economical and visual fashion [131]. A detailed description of basic MDS concepts is presented in Appendix.

In this chapter, the impact of brightness, transparency, and color on mar perception is studied. Experimental tests were conducted on a series of model plastics with selected perceptual attributes. Psychophysical measurements were conducted based on pairwise comparison test and results were interpreted using MDS statistical approach. The usefulness of this study in quantifying mar visibility resistance and designing polymeric systems with better mar performance is discussed.

V.1.EXPERIMENTAL

The model material systems selected in this study consist in 13 commercialized polycarbonate (PC) stimuli frequently used in automotive and other industries. They were used to study the impact of three perception attributes, namely, brightness, transparency, and color. The composition and processing conditions of all samples were uniformly controlled. Only slight additive formulation to control their aesthetics was changed. Opaque samples have three colors, red (R), blue (B) and green (G), with three brightness levels, low (1), medium (2), and high (3) per color to study brightness effect. Color effect is mainly studied using medium-brightness samples where brightness level is moderate. Transparency samples (T) consist in four levels of transparency, low (T1), medium (T2), high (T3), and highest (T4). Red and transparency samples are shown in Figure V-1.

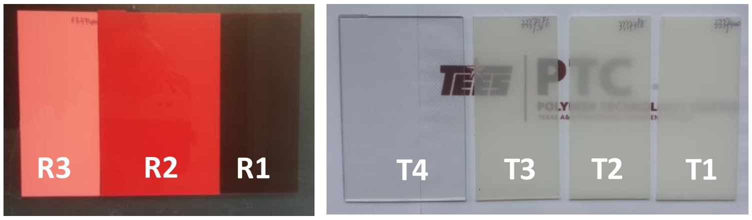

Figure V-1. Red and transparency model systems used for the present study.

To quantify the transparency level, the transmission UV-Vis spectra of the transparency samples were acquired using a UV-Vis-NIR spectrophotometer (Shimadzu, UV-3600). The wavelength range was set from 200 nm to 800 nm as shown in Figure V-2. The transmittance of highest-transparency sample (T4) is higher than 80 % in almost all the visible light region (400 nm to 800 nm). Then, it decreases with decreasing transparency level as illustrated in the figure. It has a significantly low value for the sample

T1 which has the lowest transparency. These results quantify and provide a better understanding of the transparency levels of transparency model systems.

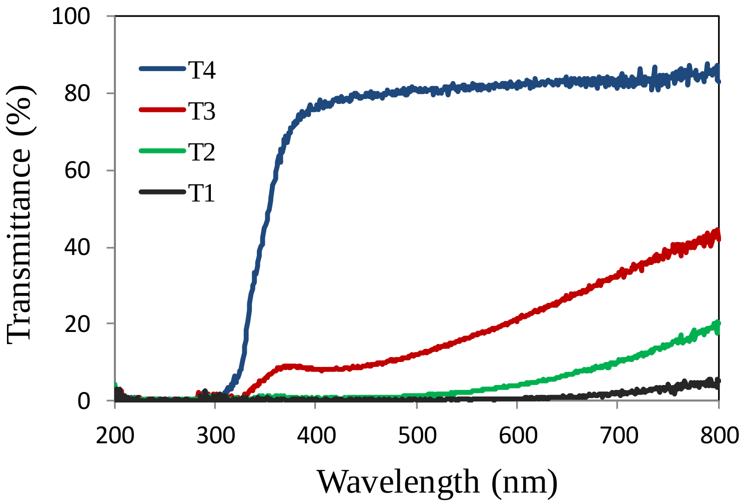

Figure V-2. UV-Vis transmittance spectra of transparency samples.

All model systems were kindly provided by SABIC. They were molded on a 260 ton on molding machine using a 15 cm x 20 cm variable thickness smooth mold (Society of Plastics Industry, SPI A-2 Finish). They were cut in half to make 10 cm x 15 cm plaques. They were then fixed in direct contact with the background of the setup, and tests were conducted on the smooth side of each sample. The white background of the samples is expected to affect mar visibility resistance of transparency samples. Mar tests were conducted with accordance to ASTM/ISO standard described previously. A 12 mm-wide barrel tip was used and the applied load linearly increased to 120 N. Tests were conducted in the flow direction to avoid scratch variation and consider worst-case scenario [26, 132].

V.2.PSYCHOPHYSICAL

The psychophysical test was conducted at least 24 hours after performing mar tests to account for the viscoelastic recovery of the samples. None of the authors was included in the psychophysical tests. A pairwise test based on MDS was conducted as follows:

V.2.1.Subjects

Since mar observation is trickier than scratch, 20 subjects were involved in this test for more statistically reliable results. They were from different backgrounds and they consist of 8 undergraduate students, 10 graduate students and 2 professionals with corrected to normal vision and aged between 19 and 35. They were unaware of the purpose of the experiment and the used MDS technique.

V.2.2.Test Condition

To achieve a better mar visualization, the psychophysical test was conducted in controlled conditions (Figure V-3). The experimental setup was in a dark room to avoid unwanted light reflections. Illumination and observation angles were fixed to 0° and 45° consecutively relative to normal, with a fixed distance between subjects and the samples. In other words, the light direction is perpendicular to the plan of the samples and forms always a 45° angle with the observation direction. A 940 lumens fluorescent light bulb was utilized on the top of the white surface with an area of almost 0.25 m^2.

Therefore, the light intensity of the bulb is around 3700 lux, which is believed to be a reasonable intensity. In fact, it is reported that the luminance of an overcast day is about 1000 lux and that of a full daylight starts from 10000 lux [133]. Therefore, a luminance of 3700 lux is sufficient to mimic real-life scenarios as shown in Figure V-3.

V.2.3.Pairwise Comparison Test

Subjects were first asked to look carefully at all the samples to familiarize themselves with mar damages. Then, they were given the following instructions of pairwise comparison test:

> *"Put two samples just below the indicated line in the middle* [to maintain the required 45° observation angle], *look at mar damages on both of them and record their ranking. Do not rate how visible the damages are, but rather how different they are from each other. The dissimilarity scale goes from 0 to 10, 0 means that mar damages look very similar between the two samples, and 10 means they are very different. Also, indicate which sample has more visible mar. Then, do the same process for each pair of all these samples."*

Figure V-3. Experimental conditions for mar MDS psychophysical test.

Each subject takes randomly two samples to compare, and keeps repeating the process until all possible pairs of samples are compared. The average test duration is about 90 minutes per subject.

V.2.4.Software

A widely used software package, *IBM SPSS Statistics,* was utilized for the MDS analysis of mar visibility resistance [134]. More details about basic MDS concepts used by IBM SPSS software can be found in Appendix. Particularly, Individual Differences Scaling (INDSCAL) algorithm implemented in SPSS is commonly used to conduct weighted Euclidean MDS [135, 136]. Individual proximity matrices of all the 20 subjects were uploaded to SPSS software. Tied ordinal weighted Euclidian MDS model based on monotone regression approach was conducted. Also, positive weights restriction was imposed and Kruskal stress (or Stress-1) was employed. To determine the optimal MDS space, Minkowski exponent r was changed from 1 to 4, and space dimension went from 2 to 6. Moreover, it is of computational significance to determine the most convenient number of iterations for each stress measurement. In ordinal MDS, the sufficient number of iterations is determined when Shepard diagrams of all the subjects show monotonic relationships [137]. This criterion will be considered in our analysis. Initially, a maximum of 30 iterations is considered.

V.3.RESULTS AND DISCUSSION

V.3.1.Optimal Minkowski Exponent

The first step consists in determining if mar perception space is Euclidian or not. In Figure V-4, *Stress-1* values are represented over Minkowski exponent for two-to-six-dimensional (2D to 6D) weighted composite spaces. For each dimensionality, optimal exponent ($r_{optimal}$), corresponding to the lowest stress values, is presented in Figure V-4.

Six and even five dimensions are considerably high for MDS analysis. Previous studies highly recommended the use of four, three or two-dimensional spaces [136, 138-140]. These are the dimensionalities considered by almost all the studies in the literature. While the optimal r value is equal to 2 for four-dimensional (4D) and three-dimensional (3D) spaces, it is equal to 1 for two-dimensional (2D) space with only 0.3% difference in stress from $r = 2$. Therefore, $r_{optimal} = 2$ is a reasonable optimal Minkowski exponent and mar perceptual space is considered as Euclidian.

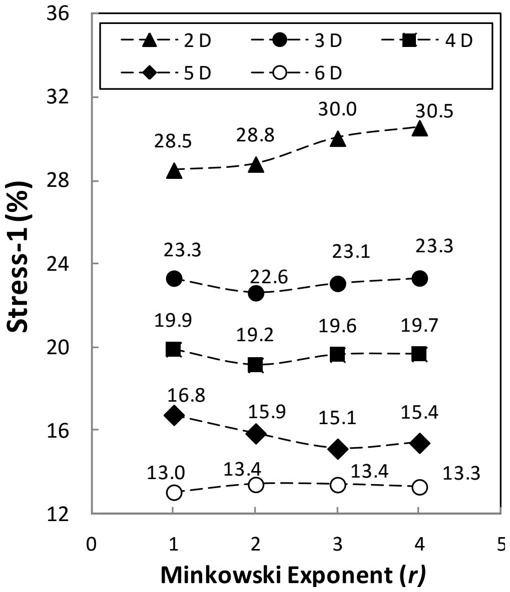

Figure V-4. The change in Kruskal stress over Minkowski exponent for two-to-six dimensional spaces.

Table V-1. Optimal Minkowski exponent and Kruskal stress values per dimension $\boldsymbol{m}$.

Dimensionality (m)	2	3	4	5	6
$r_{optimal}$	1	2	2	3	1
Stress-1 (%)	28.5	22.6	19.2	15.1	13

Previous studies highlighted the advantage of Euclidian MDS spaces. Shepard indicated that slow convergence and local minima problems are encountered only in non-Euclidean spaces [138]. Also, it was demonstrated that Euclidian space is beneficial to equally represent all the dimensions [141]. In fact, when $r = 1,$ all the dimensions are equally considered in the MDS map. As r increases, more importance is disproportionately given to the dimensions that have higher weights. Ultimately, when $r = \infty$ (known as *dominance distance*), MDS distances are determined only by the highest-weight dimension and the other dimensions are completely ignored. Consequently, it is recommended to consider Euclidian spaces if a small difference is obtained between the stress values of $r_{optimal}$ and $r = 2$.

V.3.2.Shepard Diagram

Before studying the structure of MDS maps, it is crucial to check the admissibility of the ordinal transformation used in our analysis. In weighted MDS, Shepard diagrams are generated for each individual proximity matrix separately. A representative Shepard diagram of all the subjects is presented in Figure V-5. As shown in the figure, the transformation is monotone and preserves the order of the proximities. This result was obtained for all the subjects, which indicates that the MDS transformation is admissible and a sufficient number of iterations was considered by the MDS algorithm.

V.3.3.Scree Plot

Scree plots are considered as the first and most straightforward diagram used to determine the space dimensionality. Figure V-6 shows a comparison between a typical scree plot and the empirical scree plot obtained in our analysis. Typically, an *elbow* is shown in the scree plot, indicating the appropriate space dimensionality. For instance, the MDS space is three-dimensional in Figure V-6a because an elbow is obtained when the dimension is equal to 3. However, in our study, like many previous studies [142-144], no clear elbow is observed and the stress decreases smoothly.

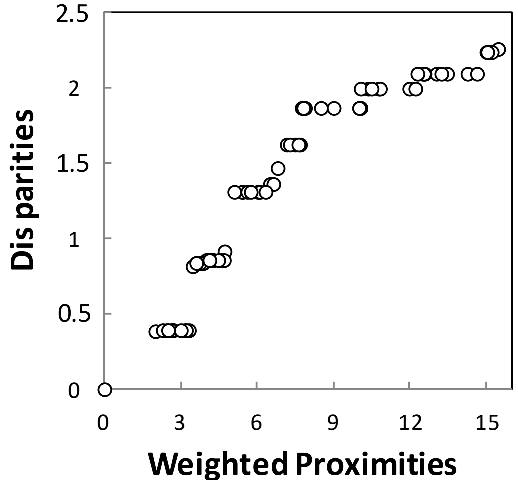

Figure V-5. A representative empirical Shepard diagram.

Therefore, more informative and practical tools should be considered, such as the interpretability of the solution itself [136, 138, 142]. In fact, if the *m*-dimensional space provides a satisfying interpretation and no further structure is revealed by the *(m+1)*-dimensional space, then *m* is the appropriate space dimensionality.

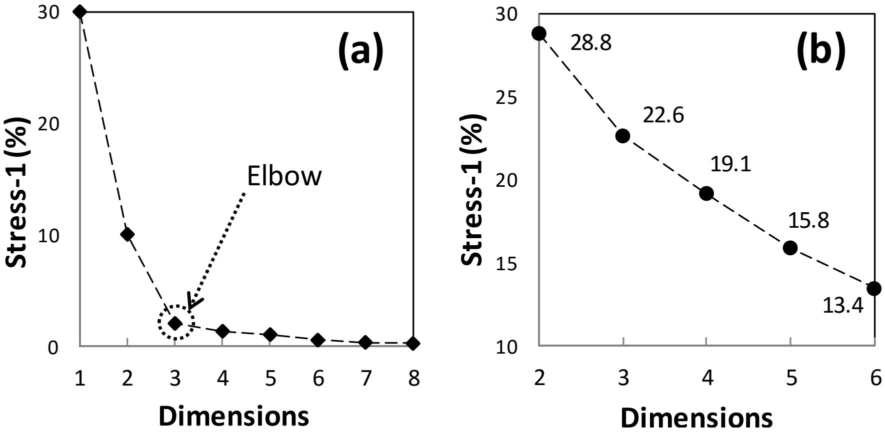

Figure V-6. (a) Typical and (b) Empirical scree plots.

V.3.4.Overall Weights of MDS Dimensions

Assessing the salience of the space dimensions is one of the major advantages of weighted Euclidian models. The overall weight of each dimension *w*, which reflects the importance of this dimension to all the 20 subjects, is given in Table V-2 for 2D and 3D MDS spaces. In 2D space, the weight of the first dimension is much higher compared to that of the second dimension ($w_1 = 0.536 > w_2 = 0.104$). Thereby, one of the attributes (brightness, transparency, or color) has more significant impact on the human assessment of mar perception than the second attribute. Similarly, in 3D space, the weight is high for the first dimension, lower for the second, and significantly low for the third dimension. Therefore, it is expected that one of the dimensions in 3D MDS space, and by extension one of the studied attributes, does not have a significant impact on mar visibility resistance. To verify the consistency of the overall weights with the individual weights of the subjects, *subject spaces* should be examined.

Table V-2. Overall dimensions weights in two and three-dimensional MDS spaces.

	2-Dimensional Space		3-Dimensional Space		
Dimension	1	2	1	2	3
Overall Weight	0.536	0.104	0.414	0.153	0.082

V.3.5.Subject Spaces

These plots provide a better visualization of the individual weights given by each subject. Subject spaces of 2D and 3D MDS spaces are shown in Figure V-7 and Figure V-8, respectively. They consist of representing each subject by a point with its individual weights to each of the dimensions as coordinates. For instance, in 2D MDS space (Figure V-7), the weights given by the fifth subject to the first and second dimensions are 0.28 and 0.71, respectively. The 45° bisector line in the figure indicates equal weights. Subject spaces can be used to know how accurate the averaged weights are in reflecting the individual weights. In Figure V-7, only Subject 5 weighted more the second dimension $(w_{15}, w_{25}) = (0.28, 0.71)$. For all the remaining subjects, the first dimension has higher weight, and thus more importance, than the second. Therefore, the overall weight of 2D MDS space in Table V-2 is consistent with the individual weights of the subjects.

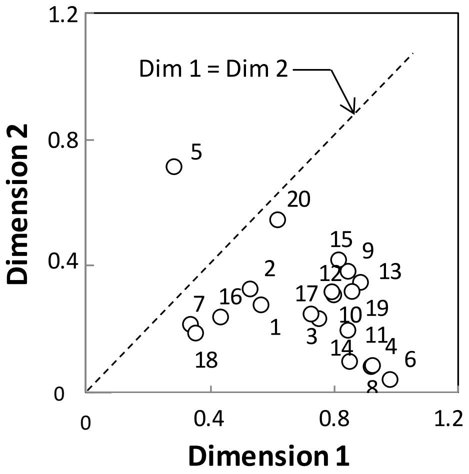

Figure V-7. Subject space of two-dimensional MDS configuration.

With regards to 3D MDS space, Figure V-8 indicates a slight decrease in the weights of the first dimension and a slight increase in the weights of the second and third dimensions. Yet, the first dimension is still more dominant and the weights of the third dimension are insignificant. Consequently, overall weights of 3D MDS space in Table V-2 are also in good coherence with the individual weights.

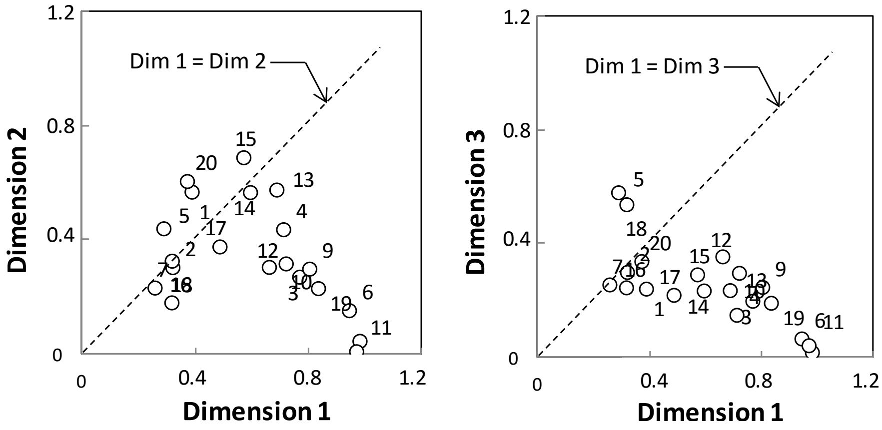

Figure V-8. Subject space of three-dimensional MDS configuration.

V.3.6.MDS Space Representation

Figure V-9a shows the 2D MDS space. The layout of the samples indicated in the experimental section is respected in the figure. Also, the color of each point reflects the color and brightness levels of the corresponding sample. As discussed earlier, it is crucial to verify if the 2D space provides a satisfying interpretation of the data. Therefore, 3D representation is considered to investigate possible new revealed structures (Figure V-9b).

Before identifying the different MDS dimensions, it is of significant importance to verify the presence of a common artifact encountered in 2D MDS spaces, namely *horseshoe effect* [145]. This effect consists in a horseshoe shape in MDS map, indicating that the second dimension is curved and twisted relative to the first dimension and does not represent a true independent dimension. As a result, an extra unnecessary dimension is added to the MDS space. This phenomenon can be avoided using non-metric (or ordinal) MDS techniques as explained by Minchin [146]. Ordinal MDS, explained in the appendix, was employed because our study is qualitative and based on rank-order. Therefore, horseshoe artifact is avoided.

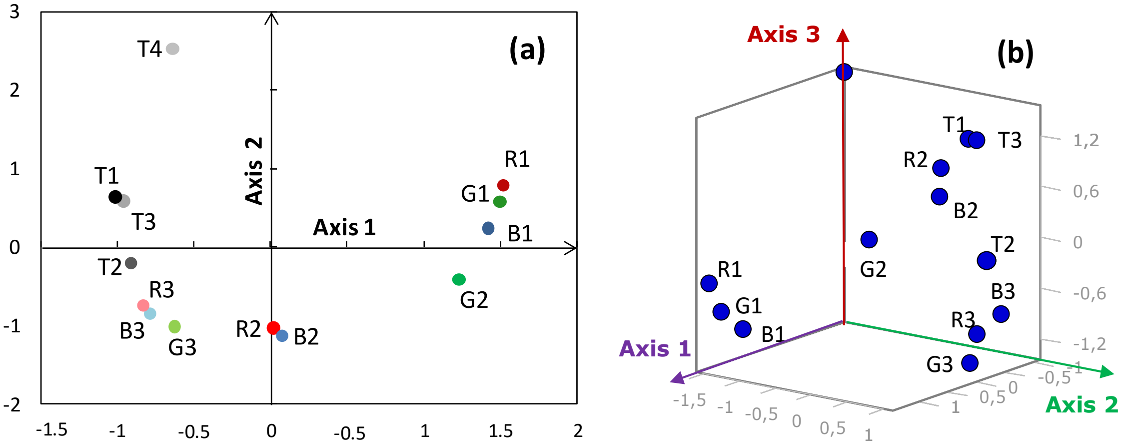

Figure V-9. MDS spaces obtained using INDSCAL weighted Euclidian distance model (a) Two-dimensional (b) Three-dimensional.

V.3.7.Dimensions

To determine the dimensions of mar perceptual space, the order of the attributes in the map should be examined. It is crucial to highlight that MDS techniques reveal information about relationships not particulars [136, 147]. Therefore, only attributes order matters, the layout of the dimensions in MDS representations is not important, and their unit is arbitrary. Also, it is important to emphasize the difference between MDS perceptual dimensions, determined through the ordering of the attributes, and the axes of the MDS map. For instance, MDS dimensions can be different from the horizontal and vertical map axes as found in previous studies [148].

V.3.7.1.First dimension

In Figure V-9a, low-brightness stimuli, R1, B1, and G1, are grouped together on the right side of the map. Then, R2, B2, and G2, lie in the middle of the map, followed by a cluster of high-brightness stimuli, R3, B3, and G3. This order demonstrates that the first dimension is indeed brightness. Moreover, transparency samples, T1, T2, and T3, are located on the left side after R3, B3, and G3. When transparency decreases, the samples are closer to white color. The sample T1 with the least transparency level is close to opaque white sample as shown in Figure V-1 and as indicated by transmittance spectra in Figure V-2. In brightness scale, white is considered as the highest level of brightness. Thus, the location of T1 after high-brightness samples, R3, B3, and G3, is consistent with the ordering of the samples on the brightness dimension. A previous study showed that the ordering across a dimension is related to its importance to the subjects [148]. Consequently, the good ordering of brightness stimuli across the first dimension is explained by its high weight in Table V-2 ($w_2 = 0.536$).

After identifying brightness as the first dimension, we consider determining how mar visibility resistance changes across this dimension based on the responses of the subjects. For red and blue stimuli, all the subjects indicated that R1 and B1 have the lowest overall mar visibility resistance. For green stimuli, 50 % of the subjects pointed out that G1 has the lowest overall mar visibility resistance, and 30 % indicated that it is G2. That is, 80% of the subjects indicated that G3 has the highest overall mar visibility resistance. Therefore, mar visibility resistance increases with higher brightness levels. This result is consistent with the brightness effect on scratch visibility resistance. Similar to scratch, this brightness effect on mar is explained by the hiddenness of whitening damage when brightness increases.

V.3.7.2.Second dimension

The stimuli T2, T3, and then T4 are vertically ordered in Figure V-9a. Therefore, transparency is considered as the second MDS dimension. However, T1 does not follow this ordering. The exclusion of this sample by the subjects in their assessment may be due to its high opacity level as shown by low T1 spectrum in Figure V-2. Similar to brightness dimension, the "goodness" of the ordering of the attributes across the transparency dimension is correlated with its weight [148]. In fact, the absence of a perfect ordering of transparency stimuli is related to the low weight of the second dimension in Table V-2 ($w_2 = 0.104$).

In an increasing overall mar visibility resistance scale, 85 % of the subjects ranked the stimuli as T2, T3, and then T4, while only 15 % ranked them as T3, T2, and then T4. It is concluded that mar visibility resistance increases with higher transparency levels. However, we found previously that scratch visibility resistance decreases with higher transparency levels. This difference in transparency effect on scratch and mar visibility resistance is explained by the difference in backgrounds. In fact, the setup used for mar observation has a white background (Figure V-3), while that used for scratch observation has a black background. Therefore, when transparency increases, whitening damage is more visible on black background (scratch case) and less visible on white background (mar case). Considering this difference in backgrounds, transparency effects on scratch and mar visibility resistance are in a good agreement.

V.3.7.3.Third dimension

We consider now investigating color effect on mar perception. In 2D MDS map (Figure V-9a) and even 3D MDS map (Figure V-9b), stimuli with the same color are not grouped together, and samples are not ordered according to their colors across a particular dimension. The absence of this ordering, and thus the absence a third dimension, is consistent with the significant low weight of this dimension in Table V-2 ($w_3 = 0.082$).

The same model systems were used to study the effects of color and brightness attributes. Therefore, these two attributes are described as *correlated* [148]. It is believed that high-weight brightness attribute dominated low-weight color attribute. To avoid brightness effect, only medium-brightness samples, R2, B2, and G2 are considered. According to 95 % of the subjects, green samples have the lowest overall mar visibility resistance. This may explain why G2 is a bit distanced from R2 and B2 in 2D and 3D MDS spaces in Figure V-9. This result is consistent with color effect on scratch visibility resistance. It is also explained by the luminous efficiency function in CIE 1978 standards [149], where a peak is reached at a wavelength of around 555 nm. The radiation at this wavelength is seen as a green light [150]. Yet, although mar on green samples is judged as most visible compared to blue and red samples, the difference between the three colors is not significant and color is not considered as a third MDS dimension in mar perceptual space.

In this chapter, we determined the impact of brightness, transparency, and color on mar visibility resistance of polymeric model systems. Our findings show that mar visibility resistance decreases with dark, less transparent, and green surfaces. MDS results show that brightness, transparency and color have a decreasing level of impact on mar perception. These results can be utilized to tailor the visual attributes of the developing polymeric products to improve their mar visibility resistance. Manufacturers are encouraged to consider brighter surfaces and avoid green color while designing their products. The transparency level is selected depending on the product background: It is recommended to use white or at least high-brightness backgrounds when mar damage is expected to occur on transparent surfaces. These parameters should be carefully considered to design polymeric products with good aesthetic properties and obtain the desired consumer impressions. Also, this approach paves the way for more studies on the impact of other perceptual and non-perceptual attributes on mar visibility resistance of both polymeric and non-polymeric products.

V.4.CONCLUSION

In this chapter, the impact of surface brightness, transparency, and color on mar visibility resistance in polymers is investigated. Mar tests were conducted according to ASTM/ISO standard. Mar perception was acquired via psychophysical tests and studied using MDS statistical technique. A tied ordinal weighted Euclidian model based on monotone regression approach was developed to characterize the perceptual space of mar damage. Also, positive weights were considered and Kruskal stress function was utilized. The main features of the present data are reasonably well captured by a two-dimensional space. Our findings indicate that mar visibility resistance decreases with green and dark surfaces. This is explained by the human eye being most sensitive to green color, and the whitening damage in mar being more apparent on dark surfaces. Also, MDS analysis shows that brightness, transparency, and color have respectively considerable, moderate, and insignificant weights. Even if mar is most visible on green samples, no significant difference in subjects' assessment is obtained between the three colors. The same MDS-based model reported in this chapter can be used to investigate the effect of other attributes on mar visibility resistance. This study offers a new avenue for the characterization of mar visibility resistance in polymers.

Other than perceptual attributes, mar is highly sensitive to surface properties. In the next chapter, we consider determining the effect of surface friction and texture on mar behavior. Friction was modified by adding fatty amide slip agent to the polymer matrix. Also, a stress analysis was conducted using the FEM model to gain a mechanistic insight on mar behavior.

CHAPTER VI

EXPERIMENTAL AND FEM ANALYSIS OF MAR BEHAVIOR *

Subtle damage in mar is highly sensitive to surface properties. After studying the impact of perceptual attributes on mar visibility resistance, we consider investigating the effect of surface friction and texture on mar behavior. The friction of the polymeric systems was changed by adding fatty amide slip agents. Also, a stress analysis of mar behavior is presented to gain a mechanistic understanding.

VI.1.EXPERIMENTAL

VI.1.1.Model Systems

To study the effect of friction on mar behavior, 20% talc-filled TPO model systems were provided by Advanced Composites. They are injection molded of 150x100x3 mm in size, and consist of four different colors (bright red, dark red, green, and black). For each color, neat and slip-agent-modified samples were provided. To investigate texture effect, two injection molded systems, A (PP + talc) and B (PP + slip agent), were provided by Japan Polypropylene. Smooth and textured animal-skin-patterned samples were provided for each system. System B allows the investigation of both texture and slip agents.

---

* Part of this chapter was reprinted from Materials and Design, 83, Hamdi, M., and Sue, H-J, Effect of color, gloss, and surface texture perception on scratch and mar visibility in polymers, 528-535. Copyright (2015), with permission from Elsevier.

VI.1.2.Mar Visualization

The scanner technique employed in conventional scratch visualization method has low resolution and a perpendicular incident light to the surface of the sample. This makes it unable to reliably capture mar damage and thus analyze it using ASV software. Therefore, a new setup was designed to overcome the limited capabilities of the conventional technique. This setup is shown in Figure VI-1. A black box was employed to isolate the sample from the ambient light interference. Two circumferential light rings, halogen and fluorescent, were tested. The validation test demonstrated that they reliably simulate the natural light, which was expected since their wavelength curves are close to CIE D65 standard. The fluorescent bulb was chosen to avoid the heat generated by the halogen bulb.

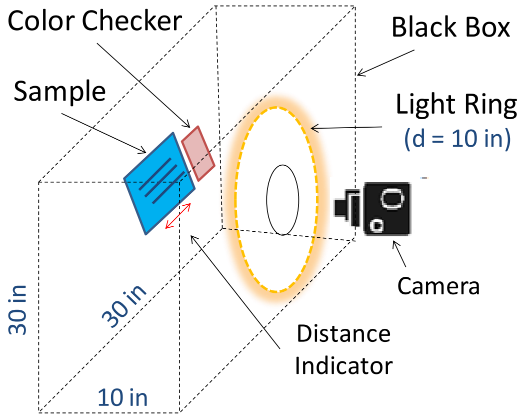

Figure VI-1. Schematic of the standardized light box used for scratch and mar observation.

A high resolution CanonT3i camera was used to capture images of scratch and mar damage. In this fashion, 45° illumination and 0° visualization angles were maintained through the dimensions of the box and the light ring and the position of the camera as highlighted in the figure. Finally, a Munsell Color X-Rite color checker was used to normalize the colors of the samples for better contrast measurements, and a 20 mm distance indicator was drawn for image calibration. Then, captured images were uploaded to ASV software for mar visibility analysis. Then, the consistency of ASV results was validated using psychophysical tests. Trained subjects determined both mar visibility onset and overall mar visibility.

VI.1.3.FTIR-ATR Characterization

Fourier-Transform Infrared Attenuated Total Reflectance (FTIR-ATR) characterization was conducted to determine the composition of the sample surfaces. Spectra were acquired using Nicolet 380 (Thermo Fisher Scientific) in conjunction with an ATR accessory (AVATAR OMNI Sampler, Germanium crystal) under ambient conditions. Samples used in this analysis were first ultrasonicated for 1 hour to clean their surfaces from any adhering particles.

VI.2.RESULTS AND DISCUSSION

VI.2.1.Consistency of the New Method

Mar damage has a wider area than scratch, and is more dependent on the surface properties. Consequently, less contrast is needed to render it visible. Psychophysical assessments showed that the contrast value in ASV software should be adjusted from 3% to 0.5% to better simulate the human observation of mar. Figure VI-2 presents a comparison between the psychophysical test, the standardized light box (with 0.5% contrast criterion), and the conventional scanner approach. Light box results are more self-consistent and consistent with the psychophysical test than scanner results. These results demonstrate the reliability of the new light box methodology in simulating the human perception of mar damages.

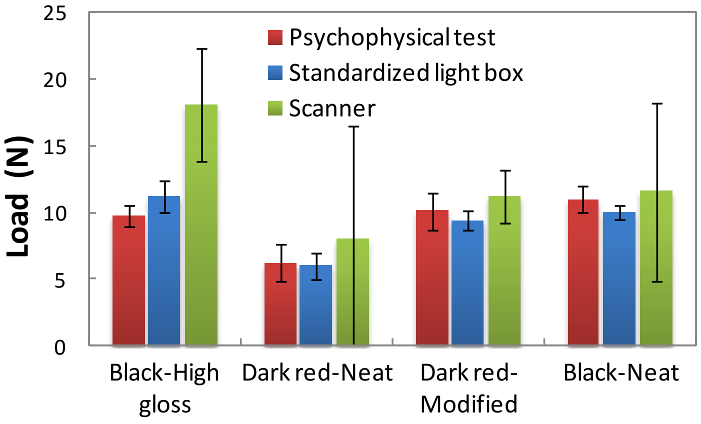

Figure VI-2. Mar visibility onset load of some model systems, comparison of psychophysical test with new and conventional methodologies.

VI.2.2.Slip Agent Effect

Figure VI-3 presents mar visibility onset of colored neat and modified samples. Results are self-consistent and in good agreement with human observation. Mar visibility onset did not change considerably with slip agent modifiers. Therefore, visibility onset might be an insufficient parameter to quantify mar visibility resistance.

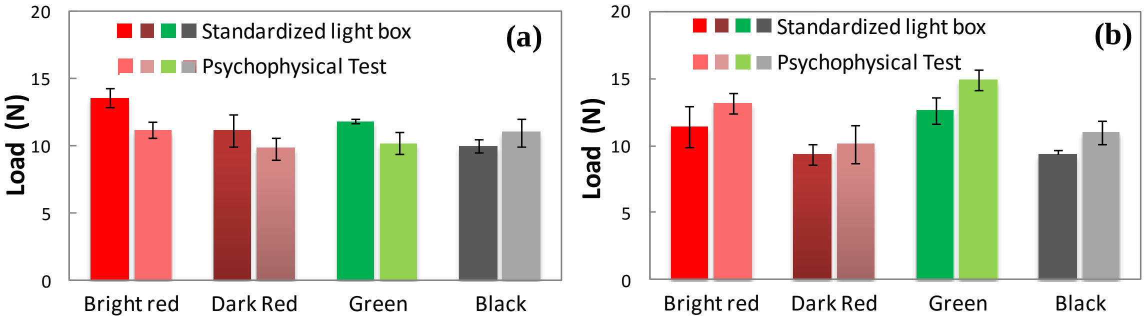

Figure VI-3. Mar visibility onset load of colored samples (a) neat and (b) modified.

To better quantify mar visibility resistance, other factors, such as the overall area of mar damage, should be considered. Total mar visibility can be more informative than just mar visibility onset. This parameter is measured using the contrast curve of the whole mar path obtained by ASV software. In Figure VI-4, mean contrast curves of colored neat and modified samples are plotted in terms of the applied normal load. For each sample, this curve is the average of the contrast curves of three mar tests. The color of the curve in this figure corresponds to the color of the sample. Dashed and continuous curves correspond to neat and modified samples, respectively. Contrast curves of neat and modified samples have different tendencies. At low normal load, both curves steadily increase in the same fashion. At higher loads, curves of neat samples reach a peak at around 70 N load and start decreasing dramatically, while those of the modified samples keep increasing to reach almost a constant plateau by the end of mar test. This observation was made for all the four examined colors. Understanding the role played by the fatty amide slip agents in changing the total contrast is crucial. This can be addressed from two different perspectives: surface composition and frictional behavior.

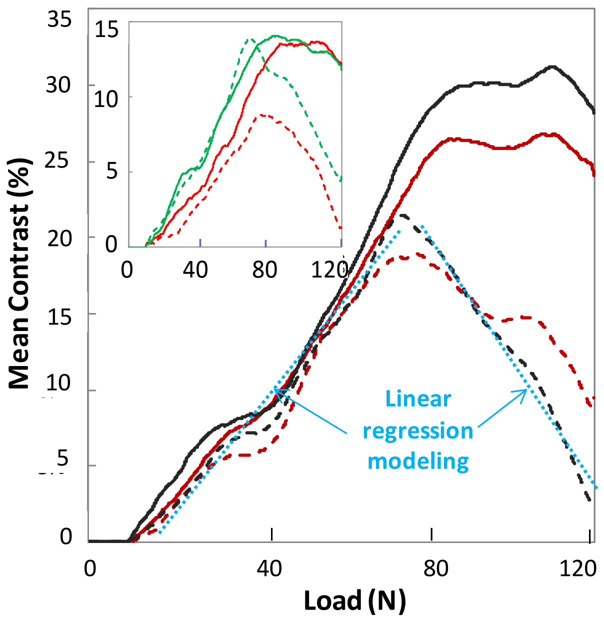

Figure VI-4. Mean contrast curves of mar damage on neat (dashed) and modified (continuous) samples. The color of the curve reflects the color of the sample.

VI.2.2.1.Surface Composition

Polymer matrix and slip agent that migrated to the surface interact differently with light. As a result, the distribution of slip agent on the surface can significantly affect the contrast of mar damage with the background. An FTIR-ATR analysis was conducted to characterize the slip agent molecules on the surface of the samples (Figure VI-5). This analysis was used first for virgin neat samples (Figure VI-5a) and virgin modified samples (Figure VI-5b). This will allow us to determine the spectra that correspond to the slip agent particles on the surface of the modified samples. Then, FTIR-ATR was employed on the mar area of the modified samples to evaluate the presence of slip agent particles after conducting mar test (Figure VI-5c). This analysis was made for each of the colored samples as shown in the figure. Three peaks were not present in the spectra of virgin neat samples, and appeared in those of virgin modified samples. The first peak is centered at 1648 cm^{-1} and corresponds to the symmetric vibration of the primary and secondary amines (R-NH2, R-NH-R') (δ_s ~ 1590 cm^{-1}) slightly shifted by the amide group (C=O) [151]. The two other peaks were centered at 3200 cm^{-1} and 3400 cm^{-1}. They correspond to symmetric (ν_s) and asymmetric (ν_{as}) stretch absorptions of primary and secondary amines, also shifted by the amide group (C=O) [151]. Thus, the three peaks correspond to the fatty amide slip agent. These peaks were mostly diminished in the spectra obtained from the damaged mar area on the modified samples (Figure VI-5c). This strong evidence suggests that fatty amide molecules were wiped from the surface of the samples during mar test. As a result, the contrast between the sample background, with fatty amide, and mar damage area, without or with diminished fatty amide, increases. These findings explain the increase of the contrast value of the modified samples at higher loads in Figure VI-4.

VI.2.2.2.Frictional behavior

Figure VI-6a shows typical normal and tangential load curves of neat and modified surfaces of the four colored samples. The tangential load of modified surface is low and smooth. However, that of neat surface is high and exhibits three distinct regions, similar to the ones observed previously [152].

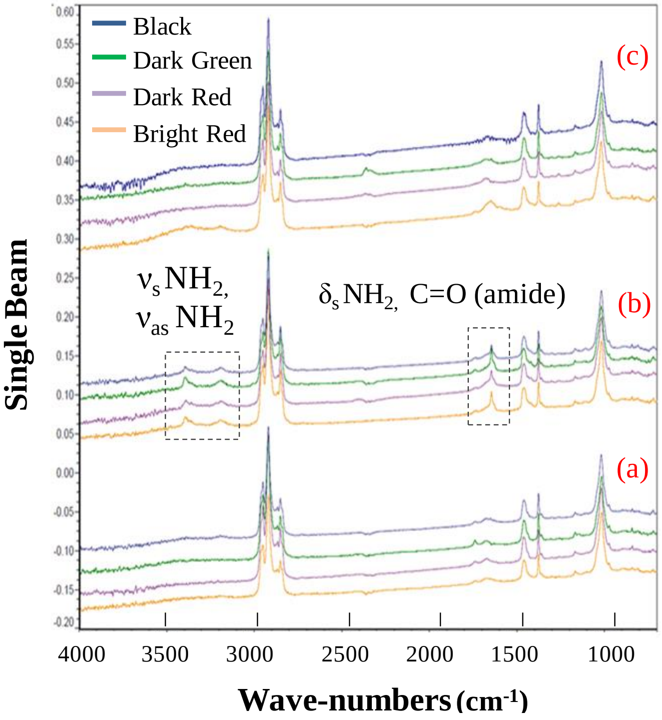

Figure VI-5. Infrared spectra of (a) neat samples, (b) modified samples, and (c) damaged modified samples on the end of the mar region.

First, it increases smoothly in a linear fashion (R1). Then, severe fluctuations occur suddenly (R2). They indicate a tremendous increase in the frictional force due to the imposed normal load and tip movement. Finally, a repetitive discontinuous sliding motion takes place mainly in the tangential load curve, but to a lower extent in the normal load curve (R3). During this motion, the tip sticks to high friction surface (Zone II) until there is a sudden break followed by a rapid slip (Zone I). It is known as *stick-slip motion* or *self-excited frictional vibration* [152-155]. This motion is due to high surface friction of the neat samples caused by the absence of slip agents. However, it depends not only on surface properties, but also on test conditions such as normal load, tip geometry, tip material, sliding velocity, and test temperature.

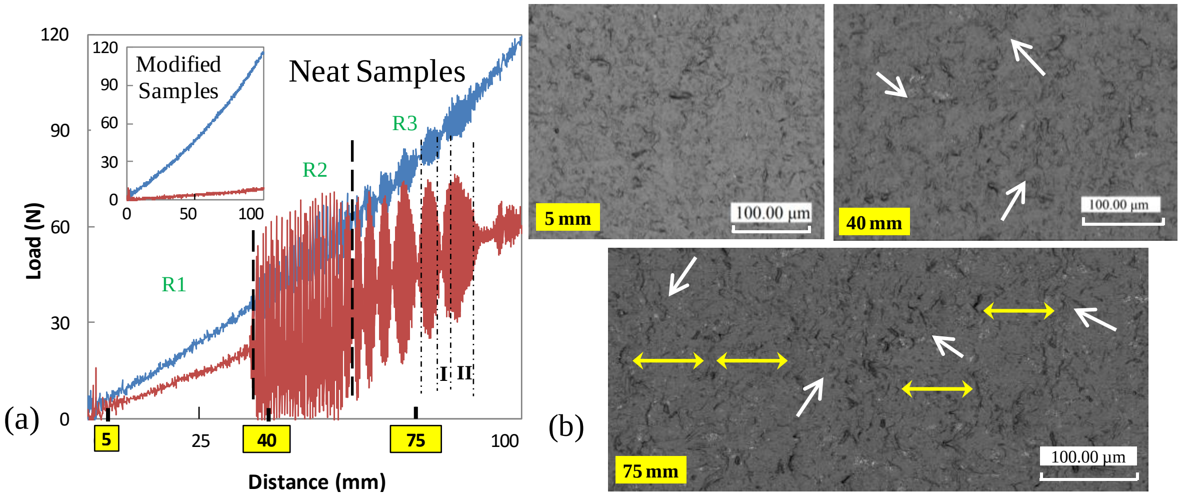

Figure VI-6. (a) Typical patterns of mar test loads on neat and modified surfaces: (blue) normal (red) tangential. (b) LSCM of mar damage features on neat sample at 5 mm, 40 mm, and 75 mm locations. White and yellow arrows refer to microcracks and periodic stick-slip patterns, respectively.

A laser confocal microscope was employed to visualize the surface features throughout the mar path. Observations were made in each of the three regions, at 5 mm, 40 mm, and 75 mm locations from the mar path (Figure VI-6b). During the mar damage, microcracks start appearing and become more frequent as the applied normal load increases (white arrows). It is believed that they are perpendicular to the mar test direction, and caused by the stress concentration behind the mar tip, just like the microcracks created in scratch damage [9, 40, 152]. Finally, series of periodic stick-slip patterns, indicated by yellow arrows, are formed at the end of the damage. The same periodic patterns were also observed in previous study [152]. Also, it was observed for all neat samples that the region R3 begins at a normal load of approximately 70 N (Figure VI-6a). At almost the same load, total contrast curves of these samples reach a peak and start decaying (Figure VI-4). Consequently, it is believed that this decay is caused by stick-slip motion. In fact, during the slip zone, mar tip jumps and less contact takes place on the surface of the sample, reducing the contrast of the remaining mar.

After investigating the effect of slip agent on the mar behavior and contrast curves, we need to explicitly determine its impact on overall mar visibility. In a new psychophysical test, four subjects were asked to look at the whole mar damage of neat and modified samples and assess their overall mar visibility. This test was conducted for every examined color. Over 90% of the observations showed that neat samples have higher mar visibility, i.e., less mar resistance. Understanding the reasons behind the above finding and identifying a new parameter that can reliably quantify mar visibility resistance is highly desirable. This parameter is thus proposed as follows.

VI.2.3.Proposed Parameter for Mar Visibility Quantification

In Figure VI-4, neat samples contrast curves reach a peak and start decreasing significantly. Thus, they have higher slope variation than the modified samples. It is believed that slope variation is a reliable parameter to quantify mar visibility resistance. For a contrast curve with slopes $S_1, \dots, S_n$, slope variation ($\Delta Slope$) is written as:

$$\Delta Slope = |S_1 - S_2| + |S_2 - S_3| + \cdots + |S_{n-1} - S_n| = \sum_{i=2}^{n} |S_i - S_{i-1}| \qquad (6)$$

All $\Delta Slope$ values are expressed in $(kN)^{-1}$ in this chapter. To precisely determine the slopes of mar contrast curves, *linear regression approach* has been utilized. Linear lines that best fit the curve were plotted using "*Trendline*" option integrated in Microsoft Excel software. For instance, blue lines in Figure VI-4 show the linear approximations of the contrast curve of neat black sample. This approach allows a more confident investigation of any correlation that might exist between slope change and mar visibility resistance. Results of neat and modified samples are summarized in Table VI-1. Neat samples, having a higher mar visibility, exhibit higher slope variation than modified samples for each of the investigated colors. This observation will be assessed for color, gloss, and texture attributes.

Table VI-1 $\Delta Slope\ in\ (kN)^{-1}$ of neat and modified samples.

	Bright Red	Green	Dark Red	Black
Neat	3.78	4.64	5.14	7.57
Modified	2.02	2.69	3.56	3.71

VI.2.4.Texture Effect

We consider now examining the contrast curves of smooth and textured surfaces. Results of neat system A and modified system B are shown in Figure VI-7a. Also, a representative image of mar damage on each surface is shown in Figure VI-7b. Smooth samples have higher mar visibility and higher $\Delta Slope$ than textured samples. Similarly, for smooth and textured surfaces, system A, with higher mar visibility, has higher $\Delta Slope$

than system B. Consequently, the correlation between $\Delta Slope$ and overall mar visibility resistance is also valid for texture analysis samples. Particularly, for textured slip-agent modified surface of system B, the flat contrast curve with low slope variation (dashed blue curve in Figure VI-7a) reflects the highly invisible mar on this sample (Figure VI-7b). This observation demonstrates that texture effect on mar visibility resistance is more significant when coupled with slip agent. Similar result was previously found for scratch.

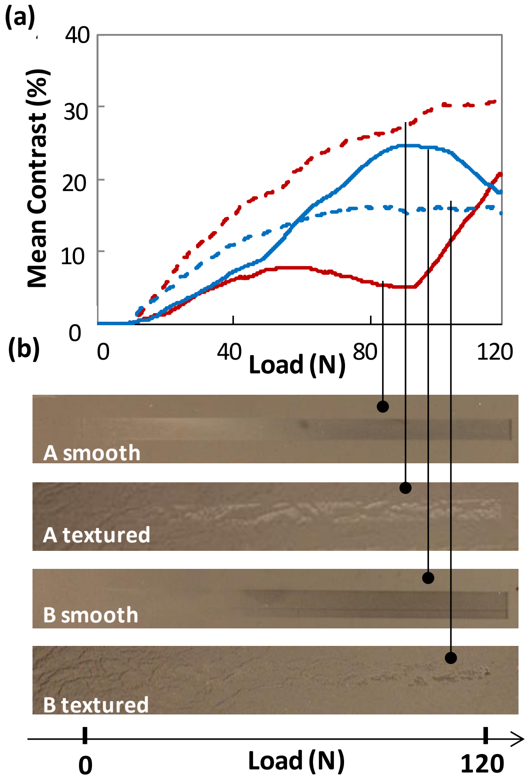

Figure VI-7. (a) Mean contrast curves of mar damage on smooth (continuous) and textured (dashed) surfaces in Systems A (red) and System B (blue). (b) Representative mar images.

In this study, a correlation was found between the slope change of mar contrast curve and the overall mar visibility. Our results demonstrate that curves with higher slope variation correspond to mar damages with less visibility resistance. Slope variation reflects the "*rate*" of contrast change within the mar damage itself. The physical interpretation of this correlation is that mar visibility is caused by both the contrast change throughout the mar region itself and the contrast between mar and the background of sample.

In a recent research Kim et al. [156] found that the main cause of gloss perception is not the bright side high specular reflections on the surface, but rather the dark side low specular reflections. The presence of dark sides next to bright sides increases significantly the contrast change throughout the surface. This boosts the human perception of gloss as a consequence. Similarly, the human perception of mar is boosted by high contrast change within the mar damage. In neat samples contrast curves, the high-contrast mar area just before the peak is followed by low-contrast mar area after the peak (dashed curves in Figure VI-4). This leads to the increase of the visibility of high-contrast area to our eyes.

More insight will be gained on these experimental findings by investigating mar behavior from a mechanistic perspective. This can be achieved by performing a stress analysis of mar damage. The FEM model presented previously was modified to simulate mar and determine the stress distribution across the mar path.

VI.3.FEM ANALYSIS

VI.3.1.FEM Model

The modified FEM model used to simulate mar damage is shown in Figure VI-8. As shown in the figure, the model dimensions are 20 mm x 4 mm x 2 mm. The barrel tip was modeled as a rigid cylindrical surface with 3 mm in length. To minimize the edge effect, a spherical edge with 1 mm in diameter was considered. Several tip designs were made previously to avoid the edge effect by increasing the edge curvature. However, the contact area between the tip and the model system increases significantly across the mar distance for high edge curvatures. As a result, the correlation between the applied load and the distributed stress across the mar damage is no longer valid. Therefore, using the spherical edge and increasing the tip length is found to be the optimal tip shape to avoid the edge effect on mar damage. Then, mar tip follows indentation, sliding, and removal steps similar test was simulated similar to scratch steps in Chapter III and Chapter IV.

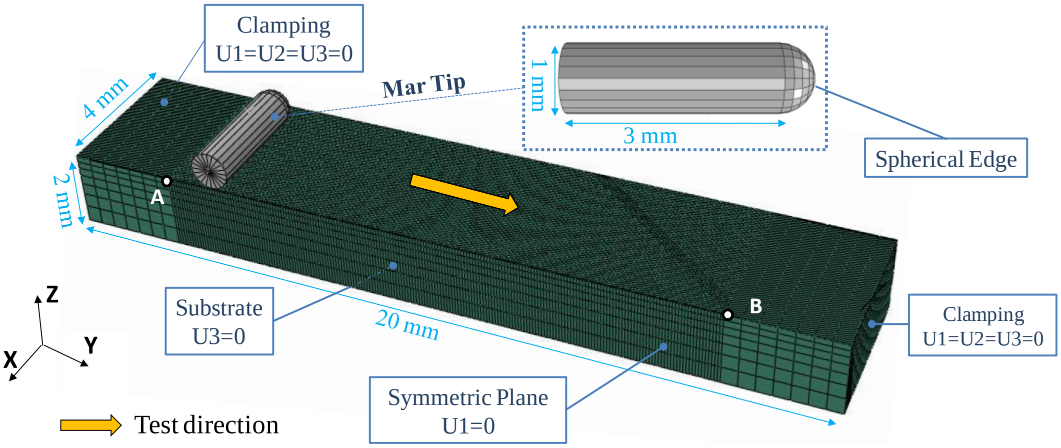

Figure VI-8. FEM model.

VI.3.2.Constitutive Parameters

Similar to the previous chapters, piecewise linear elastic–plastic stress–strain curves were employed to simulate the constitutive behavior of polymeric systems. Representative constitutive and physical parameters were introduced to the FEM model (Table VI-2). In this table, μ, E, ν, σ_y, s, h, and ρ refer to COF, elastic modulus, Poisson's ratio, yield stress, softening coefficient, hardening coefficient, and material density.

Table VI-2. Constitutive parameters introduced in the FEM model.

μ	E (GPa)	ν	σ_y (MPa)	s (MPa)	h (MPa)	ρ (g/cm^3)
0.5	1	0.4	30	250	47.3	0.905

The effect of these parameters on mar behavior will be investigated in the parametric analysis. This analysis is performed by changing only the studied parameter, and keeping the remaining parameters constant as shown in in Table VI-2.

VI.3.3.Conversion Analysis

Before performing the stress analysis, it is crucial to conduct a convergence study to assess the numerical accuracy of the adopted mesh and the acceptance of the computational cost. The number of nodes of the critical distance AB was changed from 45 to 256 to determine the optimal mesh design. The different meshing cases are summarized in Table VI-3. Also, Mesh A and Mesh E cases are presented in Figure VI-9.

Table VI-3. Mesh designs considered for the convergence study.

Mesh	Number of Elements Across Critical Edge AB
Mesh A	45
Mesh B	90
Mesh C	180
Mesh D	220
Mesh E	256

A purely elastic material is considered in this convergence study with elastic and friction properties as presented in Table VI-3. Therefore, a full recovery is expected in the wake of the mar damage. The mesh accuracy is verified through the depth profile of the edge containing AB at the end of the mar process. The computational cost is verified through the meshing CPU time.

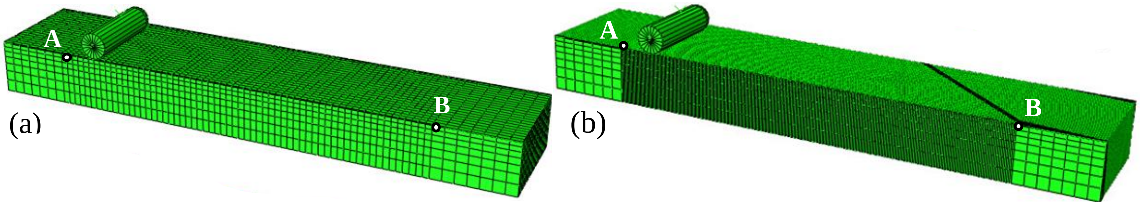

Figure VI-9. (a) Mesh A (b) Mesh E.

Depth profiles and CPU times of meshing A-E are presented in Figure VI-10. Mesh A and Mesh B present some fluctuations and do not converge to the zero level at the end of mar process. Therefore, they cannot be used in our analysis. Starting from Mesh C, the profile convergence to zero level is good and no significant difference is found in depth profiles between meshes C, D, and E. Also, the figure shows that CPU time increases considerably from one meshing to another. It increases from 45.01 hours in the case of Mesh C, to 67.56 and 90.71 hours for Mesh D and E, respectively. Consequently, the convergence study suggests that Mesh C with 180 nodes across the critical distance AB is an optimal meshing design that shows good accuracy and maintains reasonable computational time. Mesh C is the mesh shown in Figure VI-8. It has been considered for mar stress and parametric analysis.

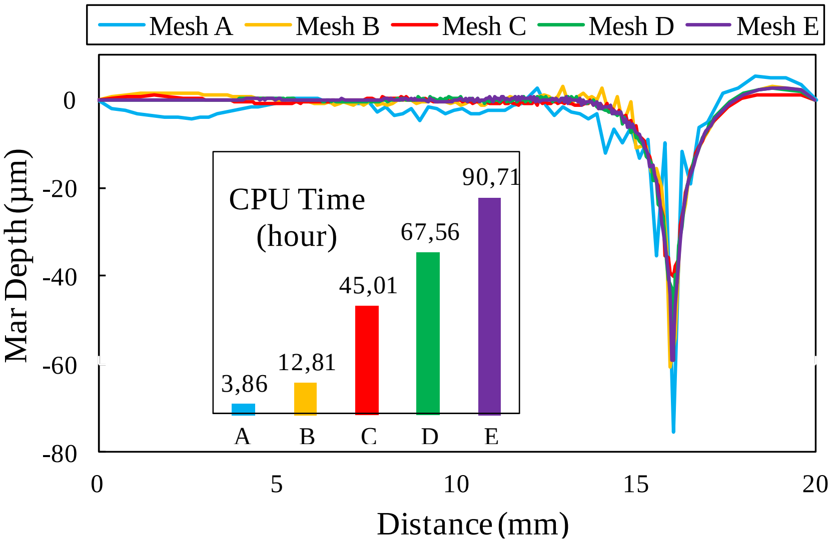

Figure VI-10. Scratch depth profiles and CPU time for meshes A – E at the end of the mar process.

VI.3.4.Stress Analysis

Unlike the spherical scratch tip, the edge of the mar tip is expected to significantly change mar-induced stress (Figure VI-8). Figure VI-11 shows the development of the maximum principal stress (σ_{pp}^{max}) as the applied mar load increases. For a better visualization, the mar tip is removed, and tip position and mar direction are indicated by black and yellow arrows, respectively. Figure VI-11a shows that high stress is first generated at the tip edge (Region A). As this load increases, Region A increases and propagates towards the inner part of mar area (Figure VI-11b and Figure VI-11c). The direction of σ_{pp}^{max}, thus damage features, in the mar area is indicated by back arrows. Then, σ_{pp}^{max} decreases significantly (Figure VI-11d) until reaching its lowest value (Region B in Figure VI-11e) and a new stress cycle begins (Figure VI-11g). This cyclic stress distribution reflects mar stick-slip oscillations observed experimentally [105]: Region A corresponds to high-stress stick motion, while Region B is associated with low-stress slip motion. Also, compressive stress is developed in front of the mar tip at sufficiently high load (Region C in Figure VI-11e and Figure VI-11g). However, this region is still insignificant compared to scratch due to low mar-induced deformation.

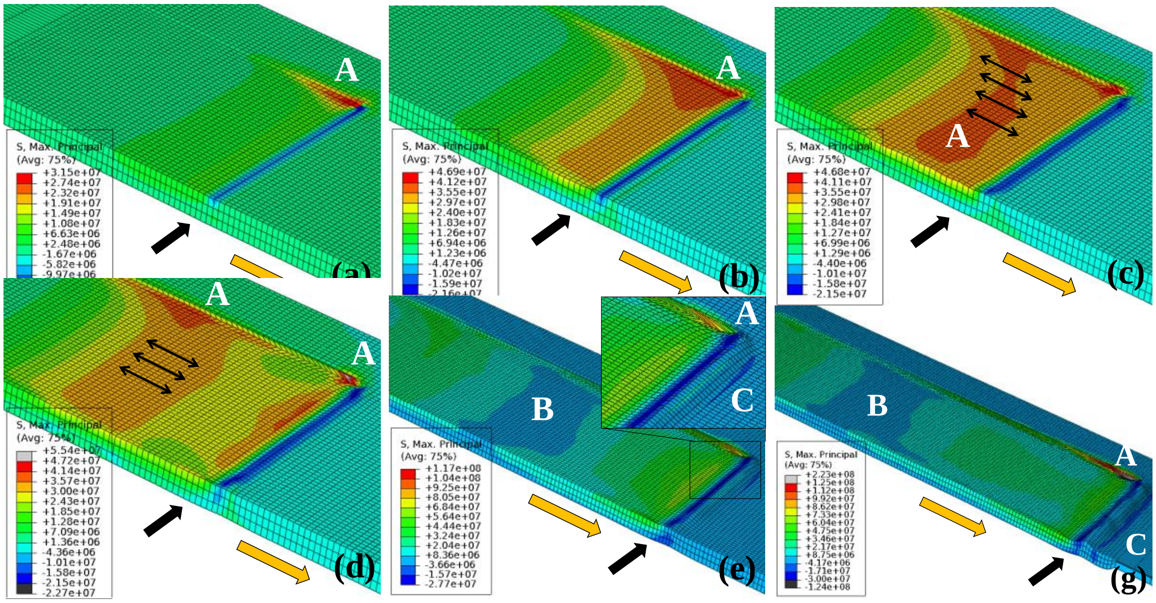

Figure VI-11. Mar-induced σ_{pp}^{max} at mar loads of (a) 20 N (b) 33.33 N (c) 40 N (d) 46.66 N (e) 80 N (g) 100 N. Tip position and test direction are indicated by black and yellow arrows, respectively.

VI.3.5.Parametric Analysis

VI.3.5.1.Effect of COF on mar behavior

Longitudinal and surface views of mar-induced von Mises stress on surfaces with different COF values are presented in Figure VI-12. It is shown that stress in the wake of mar damage and beneath the mar tip increases significantly with higher COF. This result is in agreement with previous studies demonstrating the localization of stress concentration on surfaces with higher COF [157-159]. It also explains significant mar damage on surfaces with high COF as was found previously [105].

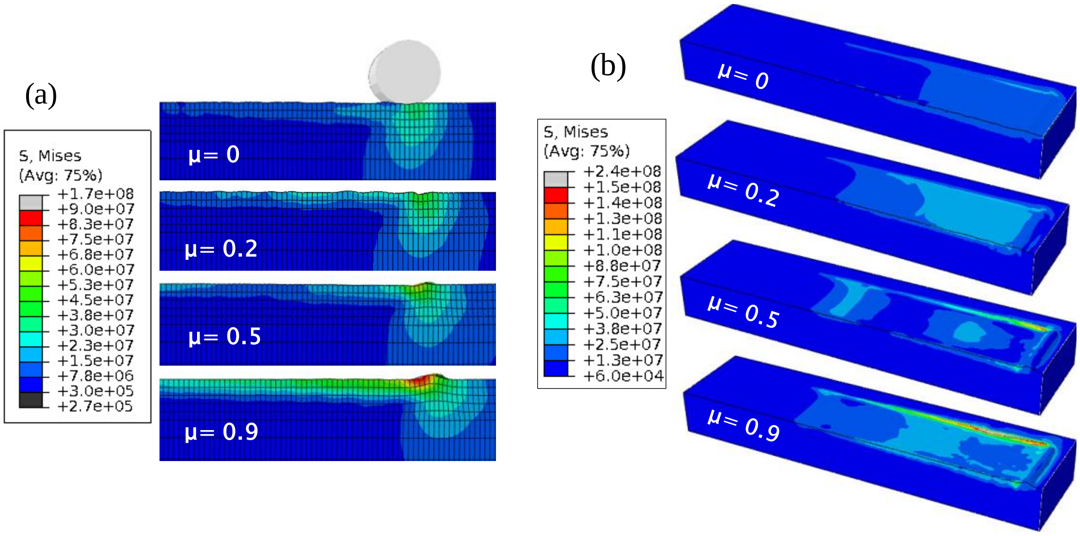

Figure VI-12. von Mises stress distribution (a) longitudinal view [L=67 N] (b) surface view [L=100 N].

Previous numerical and experimental studies showed that plastic strain reflects the nature of surface contact mechanisms [7, 88, 160-162]. In our analysis, maximum principal plastic strain (ε_{pp}^{max}) is employed to assess mar behavior. A better insight is gained using average maximum principal strain (ε_{avr}^{max}) as demonstrated previously [158, 159, 163, 164]. The value of ε_{avr}^{max} over a plastically deformed volume V_p is defined in Equation 2 where ε_i^{max}, ΔV_i, and m refer to the maximum principal plastic strain in element i, the volume of the centroid of element i, and total number of elements, respectively.

$$\varepsilon_{avr}^{max} = \frac{1}{V_p} \sum_1^m \varepsilon_i^{max} \Delta V_i \quad ; \quad V_p = \sum_1^m \Delta V_i \qquad (7)$$

The effect of surface COF on ε_{pp}^{max} and ε_{avr}^{max} is presented in Figure VI-13. It is found that higher COF leads to higher ε_{pp}^{max} and ε_{avr}^{max}. This result is consistent with previous investigations [157-159, 161, 162].

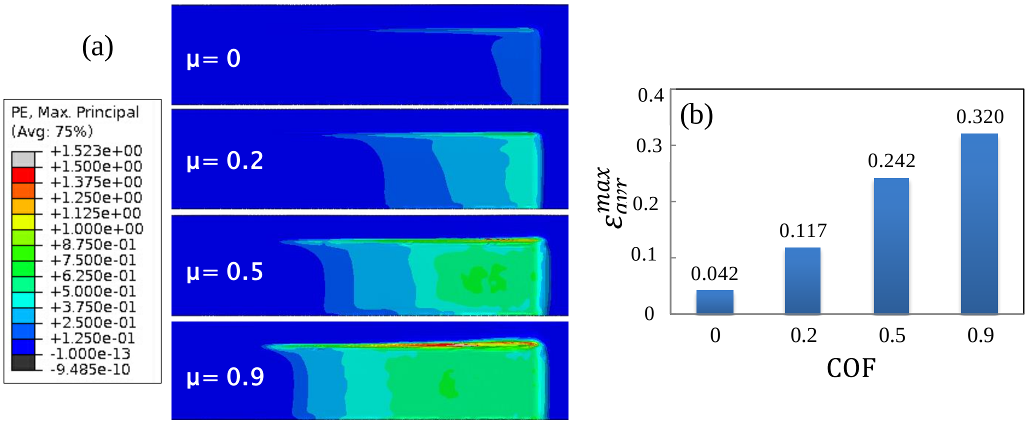

Figure VI-13. Effect of surface COF on (a) ε_{pp}^{max} (b) ε_{avr}^{max} [L = 100 N].

VI.3.5.2.Effect of Young's modulus on mar behavior

Similarly, the impact of the elastic modulus on ε_{pp}^{max} and ε_{avr}^{max} is presented in Figure VI-14a. The increase of material elastic modulus causes a gradual increase in ε_{avr}^{max} indicating higher plastic deformation on rigid surfaces. However, modulus effect is much less significant than that of COF. This results suggests that mar resistance is slightly improved with lower modulus values. It is in aligned with a recent study showing that the scratch resistance of thin polymeric films increases with lower film modulus [44].

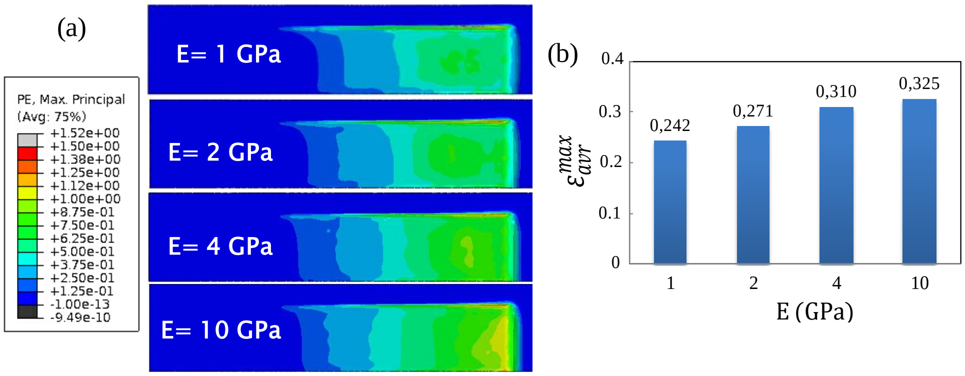

Figure VI-14. Effect of Young's modulus on (a) ε_{pp}^{max} (b) ε_{avr}^{max} [L = 100 N].

VI.3.5.3.Effect of yield stress on mar behavior

Figure VI-15a shows the effect of material yield stress on plastic strain. The value of ε_{avr}^{max} decreased dramatically from 0.242 to 0.048 as the yield stress increased from 50 MPa to 70 MPa.

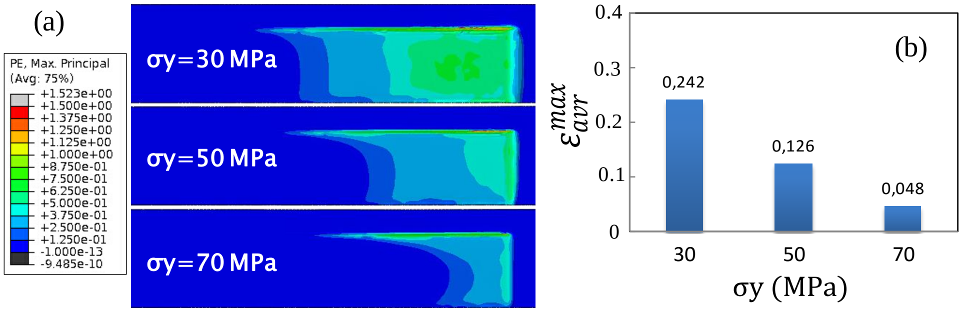

Figure VI-15. Effect of yield stress on (a) ε_{pp}^{max} (b) ε_{avr}^{max} [L = 100 N].

This result demonstrates that σ_y is a key parameter in improving mar visibility resistance. It is also consistent with σ_y effect on scratch resistance [44, 54].

VI.3.5.4.Effect of hardening slope on mar behavior

In Figure VI-16b, ε_{avr}^{max} decreases with higher hardening slope. This suggests that mar resistance is improved with higher hardening slope. Similar correlation was found between the hardening slope and scratch resistance in previous experimental and numerical studies [44, 54, 88]. However, it is observed that the hardening effect on mar damage is still insignificant compared to that of COF and yield stress.

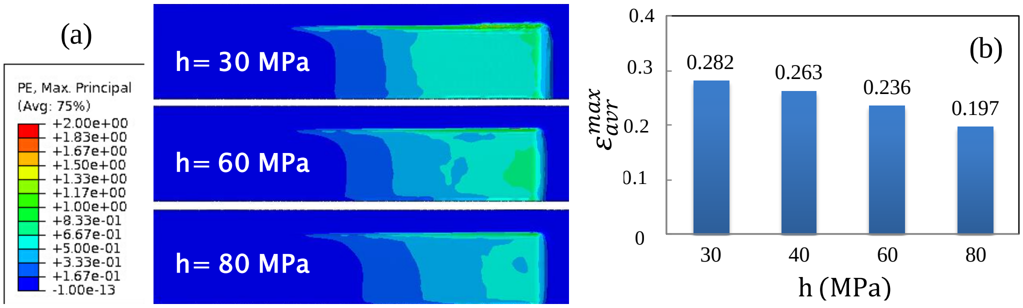

Figure VI-16. Effect of strain hardening slope on (a) ε_{pp}^{max} (b) ε_{avr}^{max} [L = 100 N].

VI.3.5.5.Effect of softening slope on mar behavior

Figure VI-17a presents the effect of strain softening slope on ε_{pp}^{max} and ε_{avr}^{max} strains. It is found that the softening slope of the studied materials has an insignificant impact. This result is in good agreement with the effect of this parameter on scratch visibility resistance [54].

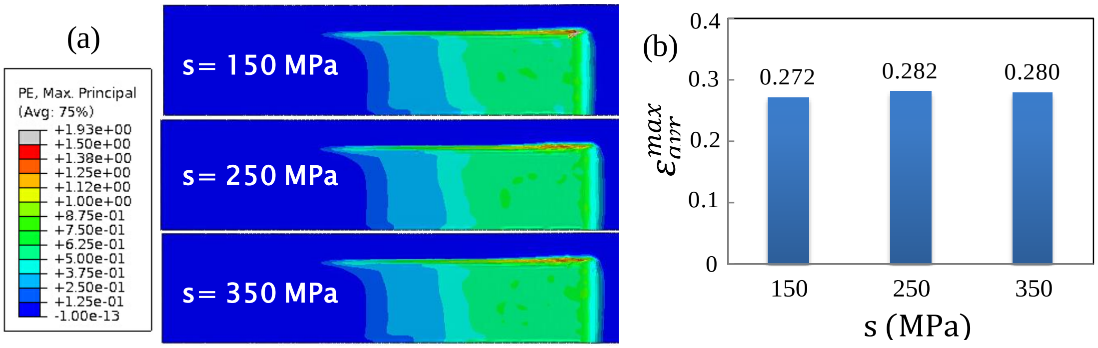

Figure VI-17. Effect of softening slope on (a) ε_{pp}^{max} (b) ε_{avr}^{max} [L = 100 N].

The parametric study shows, although they all improve mar resistance, COF, yield stress, and strain hardening slope have decreasing impact on mar, consecutively. Also, mar resistance is insensitive to strain hardening slope, but decreased with higher modulus values. These results are consistent with previous studies from the literature.

VI.4.CONCLUSION

In this chapter, a new setup was employed to study mar behavior in polymers and investigate the effect of surface friction, modified by the addition of fatty amide slip agents, and texture on mar resistance. Our findings indicate that mar visibility resistance can be consistently quantified using overall mar contrast slope. An FTIR-ATR analysis showed that slip agent additives were removed by the mar tip, which increased the contrast between the mar area and the sample background. The scratch FEM model was modified to simulate mar damage and provide a more mechanistic characterization. It is found that stress concentration is generated at the edge of mar tip, then propagates towards inner section of mar area in a repetitive fashion. This variation in stress is associated with experimental stick-slip oscillations developed during mar test. A parametric analysis was performed using the FEM model to investigate the effect of physical and constitutive parameters on mar behavior. It is found that, although they all improve mar resistance, COF, yield stress, and strain hardening slope have decreasing impact on mar, consecutively. Also, mar resistance is insensitive to strain hardening slope, but decreased with higher modulus values. These findings are consistent with previous experimental and numerical studies. The results presented in this chapter serve as a practical tool to effectively design polymeric systems with better mar performance.

CHAPTER VII

CONCLUSIONS AND FUTURE RESEARCH PLANS

VII.1.SUMMARY OF THE PRESENT RESEARCH

This dissertation research investigates scratch behavior on polymeric films and laminates, and mar behavior on bulk polymers. Fundamental, experimental, numerical, psychophysical, and statistical approaches were followed to conduct the presented studies. The experimental tests are mainly based on ASTM/ISO scratch test standard, but also on other microscopic, spectroscopic, and mechanical tools. A modified FEM model was employed to provide a mechanistic insight on scratch and mar behavior. It was used to perform a parametric study and determine the stress distribution. The psychophysical test is an effective tool to determine the human perception of scratch and mar damages and validate the experimental results. Finally, the statistical analysis was conducted based on MDS methodology to analyze the human observation results.

VII.1.1.Scratch Behavior on Polymeric Films and Laminates

Model films and laminates extensively used in the industry were utilized to conduct the experimental tests. First, the effect of molecular architecture, modified through the incorporation of ethylene comonomer, and orientation on the scratch resistance of PP-based films was investigated. Results show that film tensile properties increase with higher orientation and lower ethylene comonomer, improving scratch resistance. The FEM analysis demonstrates that this improvement is associated with a shift in stress concentration from the interface toward the surface. Also, a parametric analysis was conducted to determine the constitutive parameters with higher effect on scratch resistance. Results show that scratch resistance is improved mainly due to higher yield stress and higher strain hardening.

After examining single-layered films, the scratch performance of polymeric laminates was investigated. Experimental tests were conducted in accordance to ASTM/ISO standards on four model polyamide (PA), polypropylene (PP), PA/PP, and PP/PA systems. Results show that PP/PA laminate has better scratch performance than PA/PP. This is attributed to its low surface friction, characteristic constitutive behavior, and graded structure. Also, the numerical results were in good agreement with the experimental findings. Experimentally observed scratch deformation and damage were well-captured using the FEM model. The low scratch resistance of PA/PP is explained by its concentrated stress near the surface and at the laminate-backing interface. As for PP/PA laminate, it is observed that PP layer absorbs scratch energy more evenly while hard and stiff PA layer plays a shielding role to distribute stresses away from the interface. As a result, interfacial damages are prevented.

VII.1.2.Mar Behavior on Polymeric Materials

The second objective of the dissertation consists in conducting an in-depth analysis of mar behavior on commercialized polymeric systems frequently used in automotive industry. Mar perception on model polymeric materials with different perceptual properties, namely brightness, transparency, and color was investigated. Twenty subjects were involved in a psychophysical test based on pairwise comparison. Results were then treated using MDS analysis. Mar perception was reasonably conceptualized by a two-dimensional MDS space. Results show that brightness, transparency, and color have a decreasing level of impact on mar perception. Also, mar visibility resistance decreased with dark, less transparent, and green stimuli. However, transparency effect is still dependent on the background of the sample. To the best of our knowledge, this is the first study that applied MDS technique to analyze perception of mar on polymeric surfaces, or any other surface damage in general. The presented MDS-based model can also be utilized to study the effect of other attributes.

After investigating the perceptual attributes, experimental tests were performed to determine the effect of surface properties on mar resistance using model systems with low and high friction values. Samples with low COF were obtained by adding fatty amide slip agents to the polymeric blend. Experimental tests show that mar resistance improved with lower surface friction. The FTIR-ATR analysis suggests that the slip agent was removed from surface by the mar tip. Thus, the contrast between mar area and the background of the sample increased. Also, tangential load curves demonstrate that stick-slip motion disappears after adding slip-agent modifiers. As a result, the decrease of mar contrast caused by stick-slip oscillations did not take place on the modified samples. This study also found that overall visibility throughout the entire damage path is a better indicator for ranking mar damage. It is demonstrated that contrast slope variation parameter can consistently quantify mar visibility and simulate human perception. These experimental findings were supported by a numerical simulation of mar behavior. A stress analysis of mar damage was conducted using the FEM model. It is demonstrated that stick-slip motion observed experimentally is associated with a cyclic stress distribution that starts at the edge and propagates to the inner part of mar area. Numerical results also show that although they all improve mar resistance, COF, yield stress, and strain hardening slope have decreasing impact on mar, consecutively. Also, mar resistance is insensitive to strain hardening slope, but decreased with higher modulus values.

It is believed that fundamental understanding of scratch and mar behavior is gained in the presented research studies. They pave the way for the design of new polymeric systems with improved scratch and mar performance. This can be achieved by controlling the investigated surface, mechanical, and perceptual properties. Based on these results, further research avenues can be followed and other research studies can be conducted.

VII.2.FUTURE RESEARCH DIRECTIONS

VII.2.1.FEM Model

Consistent results were obtained using the current FEM model. However, this model can be improved in future studies by considering the true stress-strain constitutive behavior and the viscoelastic and viscoplastic properties of the examined materials. Also, more realistic results can be obtained by including the failure criteria and the thermal history of the modeled systems. Taking all these parameters into account will allow us to conduct more accurate and sophisticated FEM analysis.

VII.2.2.Scratch Behavior on Polymeric Laminates

Better insight on scratch behavior on polymeric laminates can be gained by investigating the impact of other surface and structural properties. For instance, the scratch performance of three-layered sandwich film can be investigated following the same experimental and FEM procedures presented in Chapter IV. Also, the effect of laminate interface, which highly affects its mechanical response, on scratch behavior can be investigated. The quality of this interface can be controlled using a variety of processing techniques, such as increasing the number of layers introduced to the feed block or decreasing the channel wall friction to reduce interface defects as demonstrated recently [165].

VII.2.3.Mar Behavior on Polymeric Films and Laminates

Mar behavior on polymeric films and laminates can be investigated using the same experimental and numerical techniques applied previously for scratch analysis. This study is expected to have significant impact on many industrial applications where mar damage is frequently encountered such as the automotive, packaging, and label industries.

VII.2.4.Towards a Standardized Mar Test

The experimental and psychophysical studies discussed throughout this dissertation report pave the way for the design of a standardized mar test. However, more model systems should be studied before establishing a generic method to quantitatively determine mar visibility resistance.

REFERENCES

1. Decher, G. and J.B. Schlenoff, *Multilayer thin films: sequential assembly of nanocomposite materials*. 2006: John Wiley & Sons.
2. Bekele, S. and M.D. Esakov, *Polyamide multilayer film*. 2012, U.S. Patent No. 8,206,818.
3. Puntous, T., S. Pavan, D. Delafosse, M. Jourlin, and J. Rech, *Ability of quality controllers to detect standard scratches on polished surfaces.* Precision Engineering, 2013. **37**(4): p. 924-928.
4. Fernholz, K., *Quantifying the visibility of surface distortions in class "A" automotive exterior body panels.* Journal of Manufacturing Science and Engineering, 2013. **135**(1): p. 01-11.
5. Klecka, M. and G. Subhash, *Grain size dependence of scratch-induced damage in alumina ceramics.* Wear, 2008. **265**(5): p. 612-619.
6. Dumpala, R., N. Kumar, C. Kumaran, S. Dash, B. Ramamoorthy, and M.R. Rao, *Adhesion characteristics of nano-and micro-crystalline diamond coatings: Raman stress mapping of the scratch tracks.* Diamond and Related Materials, 2014. **44**: p. 71-77.
7. Kermouche, G., N. Aleksy, J. Loubet, and J. Bergheau, *Finite element modeling of the scratch response of a coated time-dependent solid.* Wear, 2009. **267**(11): p. 1945-1953.

8. Browning, R., G.-T. Lim, A. Moyse, H.-J. Sue, H. Chen, and J. Earls, *Quantitative evaluation of scratch resistance of polymeric coatings based on a standardized progressive load scratch test.* Surface and Coatings Technology, 2006. **201**(6): p. 2970-2976.

9. Jiang, H., R. Browning, J. Whitcomb, M. Ito, M. Shimouse, T. Chang, and H.-J. Sue, *Mechanical modeling of scratch behavior of polymeric coatings on hard and soft substrates.* Tribology Letters, 2010. **37**(2): p. 159-167.

10. Nitta, K.-H., Y.-W. Shin, H. Hashiguchi, S. Tanimoto, and M. Terano, *Morphology and mechanical properties in the binary blends of isotactic polypropylene and novel propylene-co-olefin random copolymers with isotactic propylene sequence 1. Ethylene–propylene copolymers.* Polymer, 2005. **46**(3): p. 965-975.

11. Zhang, X. and A. Ajji, *Oriented structure of PP/LLDPE multilayer and blends films.* Polymer, 2005. **46**(10): p. 3385-3393.

12. Yang, Y.-H., M. Haile, Y.T. Park, F.A. Malek, and J.C. Grunlan, *Super gas barrier of all-polymer multilayer thin films.* Macromolecules, 2011. **44**(6): p. 1450-1459.

13. Affinito, J., P. Martin, M. Gross, C. Coronado, and E. Greenwell, *Vacuum deposited polymer/metal multilayer films for optical application.* Thin Solid Films, 1995. **270**(1): p. 43-48.

14. Guo, T.-F., S. Pyo, S.-C. Chang, and Y. Yang, *High performance polymer light-emitting diodes fabricated by a low temperature lamination process.* Advanced Functional Materials, 2001. **11**(5): p. 339-343.

15. De Cock, L.J., S. De Koker, B.G. De Geest, J. Grooten, C. Vervaet, J.P. Remon, G.B. Sukhorukov, and M.N. Antipina, *Polymeric multilayer capsules in drug delivery.* Angewandte Chemie International Edition, 2010. **49**(39): p. 6954-6973.
16. Chua, P.-H., K.-G. Neoh, E.-T. Kang, and W. Wang, *Surface functionalization of titanium with hyaluronic acid/chitosan polyelectrolyte multilayers and RGD for promoting osteoblast functions and inhibiting bacterial adhesion.* Biomaterials, 2008. **29**(10): p. 1412-1421.
17. Han, J.H., *Antimicrobial food packaging*. Novel Food Packaging Techniques. 2003, Cambridge, England: Woodhead Publishing Limited. 50-70.
18. Hiller, J.A., J.D. Mendelsohn, and M.F. Rubner, *Reversibly erasable nanoporous anti-reflection coatings from polyelectrolyte multilayers.* Nature Materials, 2002. **1**(1): p. 59-63.
19. Keränen, K., J.-T. Mäkinen, M. Heikkinen, M. Hiltunen, M. Koponen, M. Lahti, A. Sunnari, and K. Rönkä, *Hot laminated multilayer polymer illumination structure based on embedded LED chips.* Components, Packaging and Manufacturing Technology, IEEE Transactions on, 2012. **2**(12): p. 1965-1972.
20. Gourevich, I., L.M. Field, Z. Wei, C. Paquet, A. Petukhova, A. Alteheld, E. Kumacheva, J.J. Saarinen, and J. Sipe, *Polymer multilayer particles: A route to spherical dielectric resonators.* Macromolecules, 2006. **39**(4): p. 1449-1454.
21. Li, Y.C., S. Mannen, A.B. Morgan, S. Chang, Y.H. Yang, B. Condon, and J.C. Grunlan, *Intumescent All‐Polymer Multilayer Nanocoating Capable of Extinguishing Flame on Fabric.* Advanced Materials, 2011. **23**(34): p. 3926-3931.

22. Chang, M.-C.O. and K.R. Hansford, *Sound absorbing non-woven material, sound absorbing multilayer film, and laminates made thereof*. 2012, U.S. Patent Application No. 14/368,220.

23. Pawlik, A., M. Wielpuetz, and H. Haeger, *Multilayer film having polyamide and polypropylene layers*. 2012, U.S. Patent Application No. 13/649,379.

24. Wang, T.C., R.E. Cohen, and M.F. Rubner, *Metallodielectric photonic structures based on polyelectrolyte multilayers.* Advanced Materials, 2002. **14**(21): p. 1534-1537.

25. Schubert, E. and R. Schumacher, *Multilayer film for label production*. 2003, U.S. Patent Application No. 10/724,639.

26. Moghbelli, E., R. Browning, W.-J. Boo, S. Hahn, L. Feick, and H.-J. Sue, *Effects of molecular weight and thermal history on scratch behavior of polypropylene thin sheets.* Tribology International, 2008. **41**(5): p. 425-433.

27. Bertrand-Lambotte, P., J. Loubet, C. Verpy, and S. Pavan, *Understanding of automotive clearcoats scratch resistance.* Thin Solid Films, 2002. **420**: p. 281-286.

28. Ranjbar, Z. and S. Rastegar, *Evaluation of mar/scratch resistance of a two component automotive clear coat via nano-indenter.* Progress in Organic Coatings, 2009. **64**(4): p. 387-391.

29. Schulz, U., V. Wachtendorf, T. Klimmasch, and P. Alers, *The influence of weathering on scratches and on scratch and mar resistance of automotive coatings.* Progress in Organic Coatings, 2001. **42**(1): p. 38-48.

30. Osterhold, M. and G. Wagner, *Methods for characterizing the mar resistance.* Progress in organic coatings, 2002. **45**(4): p. 365-371.

31. Gregorovich, B. and I. Hazan, *Environmental etch performance, and scratch and mar of automotive clearcoats.* Progress in Organic Coatings, 1994. **24**(1): p. 131-146.

32. Courter, J.L., *Mar resistance of automotive clearcoats: I. Relationship to coating mechanical properties.* JCT, Journal of Coatings Technology, 1997. **69**(866): p. 57-63.

33. Wong, M., A. Moyse, F. Lee, and H.-J. Sue, *Study of surface damage of polypropylene under progressive loading.* Journal of Materials Science, 2004. **39**(10): p. 3293-3308.

34. R.L. Browning, A.M., and H.-J. Sue, *Mar behavior of thermoplastic olefins - A preliminary study*. Society of Plastics Engineers ANTEC Conference, 2007.

35. Shokrieh, M., M. Hosseinkhani, M. Naimi-Jamal, and H. Tourani, *Nanoindentation and nanoscratch investigations on graphene-based nanocomposites.* Polymer Testing, 2013. **32**(1): p. 45-51.

36. Chu, J., L. Rumao, and B. Coleman, *Scratch and mar resistance of filled polypropylene materials.* Polymer Engineering & Science, 1998. **38**(11): p. 1906-1914.

37. *ASTM D7027– 13 Standard test method for evaluation of scratch resistance of polymeric coatings and plastics using an instrumented scratch machine.* West Conshohocken, Pennsylvania: ASTM International, 2013.

38. *ISO 19252:2008, Annual Book of ISO Standards.* International Organization for Standardization 2008.

39. Friedrich, K., H. Sue, P. Liu, and A. Almajid, *Scratch resistance of high performance polymers.* Tribology International, 2011. **44**(9): p. 1032-1046.

40. Jiang, H., R. Browning, and H.-J. Sue, *Understanding of scratch-induced damage mechanisms in polymers.* Polymer, 2009. **50**(16): p. 4056-4065.

41. Hare, B.A., A. Moyse, and H.-J. Sue, *Analysis of scratch-induced damages in multi-layer packaging film systems.* Journal of Materials Science, 2012. **47**(3): p. 1389-1398.

42. Hare, B.A., H.J. Sue, L.Y. Liang, and P. Kinigakis, *Scratch behavior of extrusion and adhesive laminated multilayer food packaging films.* Polymer Engineering & Science, 2014. **54**(1): p. 71-77.

43. ABAQUS^{TM} 6.9 DassaultSystèmesSimulia Corp, *Abaqus 6.9 user manual.* Providence, RI, USA:, 2009.

44. Hamdi, M., M. Puopolo, H. Pham, and H.-J. Sue, *Experimental and FEM analysis of scratch behavior on polypropylene thin films: Effect of film orientation and ethylene monomer content.* Tribology International, 2016.

45. Hossain, M.M., E. Moghbelli, E. Jahnke, P. Boeckmann, S. Guriyanova, R. Sander, R. Minkwitz, and H.-J. Sue, *Rubber particle size and type effects on scratch behavior of styrenic-based copolymers.* Polymer, 2015. **63**: p. 71-81.

46. Kim, B.-C., H.-J. Kim, B.-H. Choi, and H.-S. Lee, *An experimental study of the scratch properties of poly (methyl methacrylate) as a function of the concentration of added slip agent.* Tribology International, 2011. **44**(12): p. 2035-2041.

47. Browning, R., G.T. Lim, A. Moyse, L. Sun, and H.J. Sue, *Effects of slip agent and talc surface-treatment on the scratch behavior of thermoplastic olefins.* Polymer Engineering & Science, 2006. **46**(5): p. 601-608.

48. Wong, M.H., *The development of scratch test methodology and characterization of surface damage of polypropylene*, in *Thesis*. 2004, Texas A&M University: Texas, USA.

49. Jiang, H., R. Browning, J. Fincher, A. Gasbarro, S. Jones, and H.-J. Sue, *Influence of surface roughness and contact load on friction coefficient and scratch behavior of thermoplastic olefins.* Applied Surface Science, 2008. **254**(15): p. 4494-4499.

50. Browning, R., H.J. Sue, R. Minkwitz, and P. Charoensirisomboon, *Effects of acrylonitrile content and molecular weight on the scratch behavior of styrene-acrylonitrile random copolymers.* Polymer Engineering & Science, 2011. **51**(11): p. 2282-2294.

51. Browning, R.L., H. Jiang, A. Moyse, H.-J. Sue, Y. Iseki, K. Ohtani, and Y. Ijichi, *Scratch behavior of soft thermoplastic olefins: effects of ethylene content and testing rate.* Journal of Materials Science, 2008. **43**(4): p. 1357-1365.

52. Browning, R., R. Minkwitz, P. Charoensirisomboon, and H.-J. Sue, *Influence of humidity on the scratch behavior of polystyrene–acrylonitrile random copolymers.* Journal of Materials Science, 2011. **46**(17): p. 5790-5797.

53. Jiang, H., G. Lim, J. Reddy, J. Whitcomb, and H.J. Sue, *Finite element method parametric study on scratch behavior of polymers*. Journal of Polymer Science Part B: Polymer Physics, 2007. **45**(12): p. 1435-1447.

54. Hossain, M.M., H. Jiang, and H.-J. Sue, *Effect of constitutive behavior on scratch visibility resistance of polymers—A finite element method parametric study*. Wear, 2011. **270**(11): p. 751-759.

55. Ni, B. and A. Le Faou, *Scratching behaviour of polymer films using blunt spherical styli*. Journal of Materials Science, 1996. **31**(15): p. 3955-3963.

56. Hare, B.A., A. Moyse, and H.J. Sue, *Evaluation of Packaging Film Mechanical Integrity Using a Standardized Scratch Test Instrument.* Packaging Technology and Science, 2012. **25**(2): p. 85-96.

57. Browning, R., M.M. Hossain, J. Li, S. Jones, and H.-J. Sue, *Contrast-based evaluation of mar resistance of thermoplastic olefins*. Tribology International, 2011. **44**(9): p. 1024-1031.

58. Browning, R.L., *Mar Evaluation of Polymers: Challenges and Accomplishments.* Scratch Behavior of Polymers Semi-annual Meeting, 2007.

59. Weon, J.-I., S.-Y. Song, K.-Y. Choi, S.-G. Lee, and J. Lee, *Quantitative determination of scratch-induced damage visibility on polymer surfaces*. Journal of Materials Science, 2010. **45**(10): p. 2649-2654.

60. Rangarajan, P., M. Sinha, V. Watkins, K. Harding, and J. Sparks, *Scratch visibility of polymers measured using optical imaging*. Polymer Engineering & Science, 2003. **43**(3): p. 749-758.

61. Jiang, H., R.L. Browning, M.M. Hossain, H.-J. Sue, and M. Fujiwara, *Quantitative evaluation of scratch visibility resistance of polymers.* Applied Surface Science, 2010. **256**(21): p. 6324-6329.

62. Michelson, A.A., *Studies in optics*. 1995, New York: Dover Publications.

63. Breil, J., *Oriented film technology.* Multilayer Flexible Packaging: Technology and Applications for the Food, Personal Care, and Over-the-Counter Pharmaceutical Industries, 2009. **5**: p. 119.

64. Tabatabaei, S.H., P.J. Carreau, and A. Ajji, *Effect of processing on the crystalline orientation, morphology, and mechanical properties of polypropylene cast films and microporous membrane formation.* Polymer, 2009. **50**(17): p. 4228-4240.

65. Mirabella, F.M., *Surface orientation of polypropylene. II. Determination for uniaxially and biaxially oriented films using internal reflection spectroscopy.* Journal of Polymer Science: Polymer Physics Edition, 1984. **22**(7): p. 1293-1304.

66. Ajji, A. and K. Cole, *Orientation characterization in polypropylene*, in *Polypropylene: An A-Z Reference*, J. Karger-Kocsis, Editor. 1999, Kluwer Academic Publishers: Dordrecht. p. 561-568.

67. De Vries, A., *Structure and properties of uni-and biaxially oriented polypropylene films: part 2-mechanical and other end-use properties.* Pure and Applied Chemistry, 1982. **54**(3): p. 647-670.

68. Vlassov, S. and V. Kuleznev, *Oriental drawing of polypropylene and its blends*, in *Polypropylene Structure, Blends and Composites*, J. Karger-Kocsis, Editor. 1995, Springer: London. p. 141-161.

69. Elias, M.B., R. Machado, and S.V. Canevarolo, *Thermal and dynamic-mechanical characterization of uni-and biaxially oriented polypropylene films.* Journal of Thermal Analysis and Calorimetry, 2000. **59**(1-2): p. 143-155.

70. Laihonen, S., U.W. Gedde, P.E. Werner, and J. Martinez-Salazar, *Crystallization kinetics and morphology of poly(propylene-stat-ethylene) fractions.* Polymer, 1997. **38**(2): p. 361-369.

71. Laihonen, S., U.W. Gedde, P.E. Werner, M. Westdahl, P. Jääskeläinen, and J. Martinez-Salazar, *Crystal structure and morphology of melt-crystallized poly(propylene-stat-ethylene) fractions.* Polymer, 1997. **38**(2): p. 371-377.

72. Reiter, G. and L. Vidal, *Crystal growth rates of diblock copolymers in thin films: Influence of film thickness.* The European Physical Journal E, 2003. **12**(3): p. 497-505.

73. Hossain, M.M., R. Minkwitz, and H.J. Sue, *Minimization of surface friction effect on scratch-induced deformation in polymers.* Polymer Engineering & Science, 2013. **53**(7): p. 1405-1413.

74. *ASTM D1708-13 Standard test method for tensile properties of plastics by use of microtensile specimens.* West Conshohocken, Pennsylvania: ASTM International, 2013.

75. McDanels, D.L., *Analysis of stress-strain, fracture, and ductility behavior of aluminum matrix composites containing discontinuous silicon carbide reinforcement.* Metallurgical Transactions A, 1985. **16**(6): p. 1105-1115.

76. Kontou, E. and P. Farasoglou, *Determination of the true stress–strain behaviour of polypropylene.* Journal of Materials Science, 1998. **33**(1): p. 147-153.

77. Amoedo, J. and D. Lee, *Modeling the uniaxial rate and temperature dependent behavior of amorphous and semicrystalline polymers.* Polymer Engineering & Science, 1992. **32**(16): p. 1055-1065.

78. Moseley, W.W., *The measurement of molecular orientation in fibers by acoustic methods.* Journal of Applied Polymer Science, 1960. **3**(9): p. 266-276.

79. Ward, I., *The correlation of molecular orientation parameters derived from optical birefringence and sonic velocity methods.* Textile Research Journal, 1964. **34**(9): p. 806-807.

80. Wang, Y., Q. Fu, Q. Li, G. Zhang, K. Shen, and Y.Z. Wang, *Ductile–brittle-transition phenomenon in polypropylene/ ethylene-propylene-diene rubber blends obtained by dynamic packing injection molding: A new understanding of the rubber-toughening mechanism.* Journal of Polymer Science Part B: Polymer Physics, 2002. **40**(18): p. 2086-2097.

81. Shinozaki, D. and G. Groves, *The plastic deformation of oriented polypropylene and polyethylene: deformation mechanisms.* Journal of Materials Science, 1973. **8**(7): p. 1012-1022.

82. Duckett, R., *Anisotropic yield behaviour*, in *Structure and Properties of Oriented Polymers*, I.M.Ward, Editor. 1997, Chapman & Hall: Dordrecht. p. 377-422.

83. Zhang, X., S. Elkoun, A. Ajji, and M. Huneault, *Oriented structure and anisotropy properties of polymer blown films: HDPE, LLDPE and LDPE.* Polymer, 2004. **45**(1): p. 217-229.

84. Alaca, B.E., M. Saif, and H. Sehitoglu, *On the interface debond at the edge of a thin film on a thick substrate.* Acta Materialia, 2002. **50**(5): p. 1197-1209.

85. Feng, X., Y. Huang, and A. Rosakis, *On the Stoney formula for a thin film/substrate system with nonuniform substrate thickness.* Journal of Applied Mechanics, 2007. **74**(6): p. 1276-1281.

86. Pindera, M.-J., J. Aboudi, and S.M. Arnold, *The effect of interface roughness and oxide film thickness on the inelastic response of thermal barrier coatings to thermal cycling.* Materials Science and Engineering: A, 2000. **284**(1): p. 158-175.

87. Evans, A., J. Hutchinson, and M. He, *Micromechanics model for the detachment of residually compressed brittle films and coatings.* Acta Materialia, 1999. **47**(5): p. 1513-1522.

88. Bucaille, J.-L., C. Gauthier, E. Felder, and R. Schirrer, *The influence of strain hardening of polymers on the piling-up phenomenon in scratch tests: experiments and numerical modelling.* Wear, 2006. **260**(7): p. 803-814.

89. Burnett, P. and D. Rickerby, *The relationship between hardness and scratch adhession.* Thin Solid Films, 1987. **154**(1-2): p. 403-416.

90. Akkapeddi, M.K. and B.A. Lynch, *Delamination resistant multilayer containers*. 2014, U.S. Patent No. 8,822,001.

91. Chomik, R.S., R. Knuth, C. Yeager, and M. Yoho, *Odor transmission-resistant polymeric film*. 2013, U.S. Patent No. 8,440,316.

92. Holzbauer, T.J., A. Sadik, M.-C.O. Chang, and G.J. Cisko Jr, *Multi-layer catheter tubes with odor barrier*. 2015, U.S. Patent No. 8,936,583.

93. Peduto, N. and F. Speroni, *Multilayer structure based on polyamides and tube or conduit with multilayer structure*. 2012, U.S. Patent No. 8,153,215.

94. Kerschbaumer, F., *Multi-layered tubes having impact resistance-modified polyamide layers*. 1993, U.S. Patent No. 5,219,003.

95. Félix, J.S., J.E. Manzoli, M. Padula, and M. Monteiro, *Evaluation of Different Conditions of Contact for Caprolactam Migration from Multilayer Polyamide Films into Food Simulants.* Packaging Technology and Science, 2014. **27**(6): p. 457-466.

96. Reddy, N., D. Nama, and Y. Yang, *Polylactic acid/polypropylene polyblend fibers for better resistance to degradation.* Polymer Degradation and Stability, 2008. **93**(1): p. 233-241.

97. Horas, J. and M. Rizzotto, *Gas diffusion in and through polypropylene*, in *Polypropylene: An A-Z Reference*, J. Karger-Kocsis, Editor. 1999, Kluwer Academic Publishers: Dordrecht. p. 273-276.

98. Tews, W. and M. Heck, *Polypropylene film for electron-beam hardening applications*. 2014, U.S. Patent No. 8,641,854.

99. Hadal, R. and R. Misra, *Scratch deformation behavior of thermoplastic materials with significant differences in ductility.* Materials Science and Engineering: A, 2005. **398**(1): p. 252-261.

100. Fornes, T. and D. Paul, *Modeling properties of nylon 6/clay nanocomposites using composite theories.* Polymer, 2003. **44**(17): p. 4993-5013.

101. Chavarria, F. and D. Paul, *Comparison of nanocomposites based on nylon 6 and nylon 66.* Polymer, 2004. **45**(25): p. 8501-8515.

102. Choi, H., G. Kwon, G. Lee, and D. Bae, *Reinforcement with carbon nanotubes in aluminum matrix composites.* Scripta Materialia, 2008. **59**(3): p. 360-363.

103. Chawla, N., V. Ganesh, and B. Wunsch, *Three-dimensional (3D) microstructure visualization and finite element modeling of the mechanical behavior of SiC particle reinforced aluminum composites.* Scripta Materialia, 2004. **51**(2): p. 161-165.

104. Pinto, G. and A. Jiménez-Martín, *Conducting aluminum-filled nylon 6 composites.* Polymer Composites, 2001. **22**(1): p. 65-70.

105. Hamdi, M. and H.-J. Sue, *Effect of color, gloss, and surface texture perception on scratch and mar visibility in polymers.* Materials & Design, 2015. **83**: p. 528-535.

106. Jiang, H., Q. Cheng, C. Jiang, J. Zhang, and L. Yonghua, *Effect of stick-slip on the scratch performance of polypropylene.* Tribology International, 2015. **91**: p. 1-5.

107. Erdogan, F., *Fracture mechanics of functionally graded materials.* Composites Engineering, 1995. **5**(7): p. 753-770.

108. Suresh, S., *Graded materials for resistance to contact deformation and damage.* Science, 2001. **292**(5526): p. 2447-2451.

109. Freund, L.B. and S. Suresh, *Thin Film Materials: Stress, Defect Formation and Surface Evolution*. 2004, Cambridge: Cambridge University Press.

110. Williamson, R., B. Rabin, and J. Drake, *Finite element analysis of thermal residual stresses at graded ceramic-metal interfaces. Part I. Model description and geometrical effects.* Journal of Applied Physics, 1993. **74**(2): p. 1310-1320.

111. Drake, J., R. Williamson, and B. Rabin, *Finite element analysis of thermal residual stresses at graded ceramic-metal interfaces. Part II. Interface optimization for residual stress reduction.* Journal of Applied Physics, 1993. **74**(2): p. 1321-1326.

112. Giannakopoulos, A., S. Suresh, M. Finot, and M. Olsson, *Elastoplastic analysis of thermal cycling: layered materials with compositional gradients.* Acta Metallurgica et Materialia, 1995. **43**(4): p. 1335-1354.

113. Branch, N.A., N.K. Arakere, G. Subhash, and M.A. Klecka, *Determination of constitutive response of plastically graded materials.* International Journal of Plasticity, 2011. **27**(5): p. 728-738.

114. Karimi, A., Y. Wang, T. Cselle, and M. Morstein, *Fracture mechanisms in nanoscale layered hard thin films.* Thin Solid Films, 2002. **420**: p. 275-280.

115. Giannakopoulos, A. and S. Suresh, *Indentation of solids with gradients in elastic properties: Part I. Point force.* International Journal of Solids and Structures, 1997. **34**(19): p. 2357-2392.

116. Giannakopoulos, A. and S. Suresh, *Indentation of solids with gradients in elastic properties: Part II. Axisymmetric indentors.* International Journal of Solids and Structures, 1997. **34**(19): p. 2393-2428.

117. Pender, D., N. Padture, A. Giannakopoulos, and S. Suresh, *Gradients in elastic modulus for improved contact-damage resistance. Part I: The silicon nitride–oxynitride glass system.* Acta Materialia, 2001. **49**(16): p. 3255-3262.

118. Jitcharoen, J., N.P. Padture, A.E. Giannakopoulos, and S. Suresh, *Hertzian-Crack Suppression in Ceramics with Elastic-Modulus-Graded Surfaces.* Journal of the American Ceramic Society, 1998. **81**(9): p. 2301-2308.

119. Suresh, S., M. Olsson, A. Giannakopoulos, N. Padture, and J. Jitcharoen, *Engineering the resistance to sliding-contact damage through controlled gradients in elastic properties at contact surfaces.* Acta Materialia, 1999. **47**(14): p. 3915-3926.

120. Suresh, S., A. Giannakopoulos, and J. Alcala, *Spherical indentation of compositionally graded materials: theory and experiments.* Acta Materialia, 1997. **45**(4): p. 1307-1321.

121. Lambros, J., M. Santare, H. Li, and G. Sapna III, *A novel technique for the fabrication of laboratory scale model functionally graded materials.* Experimental Mechanics, 1999. **39**(3): p. 184-190.

122. Giannakopoulos, A., *Indentation of plastically graded substrates by sharp indentors.* International Journal of Solids and Structures, 2002. **39**(9): p. 2495-2515.

123. Rueda, M.F., L. Cui, and M. Gilchrist, *Optimisation of energy absorbing liner for equestrian helmets. Part I: Layered foam liner.* Materials & Design, 2009. **30**(9): p. 3405-3413.

124. Gupta, N., *A functionally graded syntactic foam material for high energy absorption under compression.* Materials Letters, 2007. **61**(4): p. 979-982.

125. Koohbor, B. and A. Kidane, *Design optimization of continuously and discretely graded foam materials for efficient energy absorption.* Materials & Design, 2016. **102**: p. 151-161.

126. Wang, E., N. Gardner, and A. Shukla, *The blast resistance of sandwich composites with stepwise graded cores.* International Journal of Solids and Structures, 2009. **46**(18): p. 3492-3502.

127. Chen, Y., F. Chen, W. Zhang, Z. Du, and H. Hua, *Transient underwater shock response of sacrificed coating with continuous density graded foam core.* Composites Part B: Engineering, 2016. **98**: p. 297-307.

128. Maheo, L. and P. Viot, *Impact on multi-layered polypropylene foams.* International Journal of Impact Engineering, 2013. **53**: p. 84-93.

129. Lawn, B., *Fracture of Brittle Solids*. 2nd Edition ed. Cambridge Solid State Science Series. 1993, Cambridge: Cambridge university press.

130. Szeto, W., M. Xie, J. Kim, M. Yuen, P. Tong, and S. Yi. *Interface failure criterion of button shear test as a means of interface adhesion measurement in plastic packages*. in *Electronic Materials and Packaging, 2000.(EMAP 2000). International Symposium on*. 2000. IEEE.

131. Young, F.W., *Multidimensional scaling: History, theory, and applications*. 2013, Hillsdale, New Jersey: Psychology Press.

132. Bermúdez, M.D., W. Brostow, F.J. Carrión-Vilches, and J. Sanes, *Scratch resistance of polycarbonate containing ZnO nanoparticles: effects of sliding direction.* Journal of Nanoscience and Nanotechnology, 2010. **10**(10): p. 6683-6689.

133. Hwajeong, S., C. Jongseok, K. Hyunjin, P. Taehwan, and K. Howon. *Short paper: Surveillance system with light sensor*. in *Internet of Things (WF-IoT), 2014 IEEE World Forum on*. 2014.

134. SPSS, I., *IBM SPSS statistics base 20.* Chicago, IL: SPSS Inc, 2011.

135. Borg, I. and P.J. Groenen, *Modern Multidimensional Scaling: Theory and Applications*. Springer Series in Statistics, ed. P.D. P. Bickel, S. Fienberg, U. Gather, I. Olkin, S. Zeger. 2005, New York: Springer Science & Business Media.

136. Hout, M.C., M.H. Papesh, and S.D. Goldinger, *Multidimensional scaling.* WIREs Cogn Sci, 2013. **4**(1): p. 93-103.

137. Giguère, G., *Collecting and analyzing data in multidimensional scaling experiments: A guide for psychologists using SPSS.* Tutorials in Quantitative Methods for Psychology, 2006. **2**(1): p. 26-37.

138. Shepard, R.N., *Representation of structure in similarity data: Problems and prospects.* Psychometrika, 1974. **39**(4): p. 373-421.

139. Shepard, R.N., *Multidimensional scaling, tree-fitting, and clustering.* Science, 1980. **210**(4468): p. 390-398.

140. Lew, J.S., *Some counterexamples in multidimensional scaling.* Journal of Mathematical Psychology, 1978. **17**(3): p. 247-254.

141. Cross, D.V., *Metric Properties of Multidimensional Stimulus Control*, in *Thesis* 1965, University of Michigan: Michigan, USA.

142. Kruskal, J.B., *Multidimensional scaling by optimizing goodness of fit to a nonmetric hypothesis.* Psychometrika, 1964. **29**(1): p. 1-27.

143. Holliins, M., R. Faldowski, S. Rao, and F. Young, *Perceptual dimensions of tactile surface texture: A multidimensional scaling analysis.* Perception & Psychophysics, 1993. **54**(6): p. 697-705.

144. Hollins, M., S. Bensmaïa, K. Karlof, and F. Young, *Individual differences in perceptual space for tactile textures: Evidence from multidimensional scaling.* Perception & Psychophysics, 2000. **62**(8): p. 1534-1544.

145. Diaconis, P., S. Goel, and S. Holmes, *Horseshoes in multidimensional scaling and local kernel methods.* The Annals of Applied Statistics, 2008: p. 777-807.

146. Minchin, P.R., *An evaluation of the relative robustness of techniques for ecological ordination*, in *Theory and Models in Vegetation Science*. 1987, Springer Netherlands: Dordrecht. p. 89-107.

147. Jaworska, N. and A. Chupetlovska-Anastasova, *A review of multidimensional scaling (MDS) and its utility in various psychological domains.* Tutorials in Quantitative Methods for Psychology, 2009. **5**(1): p. 1-10.

148. Bergmann Tiest, W.M. and A.M. Kappers, *Analysis of haptic perception of materials by multidimensional scaling and physical measurements of roughness and compressibility.* Acta Psychologica, 2006. **121**(1): p. 1-20.

149. CIE, *Light as a True Visual Quantity: Principles of Measurement*, in *CIE 041-(TC 1.4)*. 1978: Bureau Central de la CIE, Paris.

150. *Colorimetry: understanding the CIE system*, ed. J. Schanda. 2007, New Jersey, USA: John Wiley & Sons Publications.

151. Choukourov, A., H. Biederman, I. Kholodkov, D. Slavinska, M. Trchova, and A. Hollander, *Properties of amine-containing coatings prepared by plasma polymerization.* Journal of Applied Polymer Science, 2004. **92**(2): p. 979-990.

152. Fukahori, Y. and H. Yamazaki, *Mechanism of rubber abrasion. Part I: Abrasion pattern formation in natural rubber vulcanizate.* Wear, 1994. **171**(1): p. 195-202.

153. Fukahori, Y. and H. Yamazaki, *Mechanism of rubber abrasion: Part 2. General rule in abrasion pattern formation in rubber-like materials.* Wear, 1994. **178**(1): p. 109-116.

154. Fukahori, Y. and H. Yamazaki, *Mechanism of rubber abrasion part 3: how is friction linked to fracture in rubber abrasion?* Wear, 1995. **188**(1): p. 19-26.

155. Zhang, S. and J. Li, *Slip process of stick–slip motion in the scratching of a polymer.* Materials Science and Engineering: A, 2003. **344**(1): p. 182-189.

156. Kim, J., P.J. Marlow, and B.L. Anderson, *The dark side of gloss.* Nature Neuroscience, 2012. **15**(11): p. 1590-1595.

157. Hamilton, G. and L. Goodman, *The stress field created by a circular sliding contact.* Journal of Applied Mechanics, 1966. **33**(2): p. 371-376.

158. Pelletier, H., C. Gauthier, and R. Schirrer, *Influence of the friction coefficient on the contact geometry during scratch onto amorphous polymers.* Wear, 2010. **268**(9): p. 1157-1169.

159. Pelletier, H., C. Gauthier, and R. Schirrer, *Strain and stress fields during scratch tests on amorphous polymers: influence of the local friction.* Tribology Letters, 2008. **32**(2): p. 109-116.

160. Felder, E. and J.-L. Bucaille, *Mechanical analysis of the scratching of metals and polymers with conical indenters at moderate and large strains.* Tribology International, 2006. **39**(2): p. 70-87.

161. Pelletier, H., A.-L. Durier, C. Gauthier, and R. Schirrer, *Viscoelastic and elastic–plastic behaviors of amorphous polymeric surfaces during scratch.* Tribology International, 2008. **41**(11): p. 975-984.

162. Pelletier, H., C. Gauthier, and R. Schirrer, *Experimental and finite-element analysis of scratches on amorphous polymeric surfaces.* Proceedings of the Institution of Mechanical Engineers, Part J: Journal of Engineering Tribology, 2008. **222**(3): p. 221-230.

163. Jayaraman, S., G. Hahn, W. Oliver, C. Rubin, and P. Bastias, *Determination of monotonic stress-strain curve of hard materials from ultra-low-load indentation tests.* International Journal of Solids and Structures, 1998. **35**(5): p. 365-381.

164. Bucaille, J., E. Felder, and G. Hochstetter, *Mechanical analysis of the scratch test on elastic and perfectly plastic materials with the three-dimensional finite element modeling.* Wear, 2001. **249**(5): p. 422-432.

165. Huntington, B., E. Chabert, S. Rahal, J. Patz, J. Silva, P. Harris, J. Maia, and R. Bonnecaze, *Distortion of interfaces in a multilayer polymer co-extrusion feedblock.* International Polymer Processing, 2013. **28**(3): p. 274-280.

166. Indow, T., *Multidimensional studies of Munsell color solid.* Psychological Review, 1988. **95**(4): p. 456-470.

167. Wills, J., S. Agarwal, D. Kriegman, and S. Belongie, *Toward a perceptual space for gloss.* ACM Transactions on Graphics (TOG), 2009. **28**(4): p. 103.

168. Shepard, R.N., *The analysis of proximities: Multidimensional scaling with an unknown distance function. I.* Psychometrika, 1962. **27**(2): p. 125-140.

169. Shepard, R.N., *The analysis of proximities: Multidimensional scaling with an unknown distance function. II.* Psychometrika, 1962. **27**(3): p. 219-246.

170. Gregson, R., *Representation of taste mixture cross-modal matching in a Minkowski r-metric.* Australian Journal of Psychology, 1965. **17**(3): p. 195-204.

171. Ashby, F.G., W.T. Maddox, and W.W. Lee, *On the dangers of averaging across subjects when using multidimensional scaling or the similarity-choice model.* Psychological Science, 1994. **5**(3): p. 144-151.

172. Vermeesch, P. and E. Garzanti, *Making geological sense of 'Big Data'in sedimentary provenance analysis.* Chemical Geology, 2015. **409**: p. 20-27.

173. Rutherford, K.M., R.D. Donald, A.B. Lawrence, and F. Wemelsfelder, *Qualitative behavioural assessment of emotionality in pigs.* Applied Animal Behaviour Science, 2012. **139**(3): p. 218-224.

APPENDIX

THEORETICAL BACKGROUND OF MDS

A.1.INTRODUCTION

MDS analysis is frequently employed to represent measurements of dissimilarities among pairs of objects as distances between points in a low-dimensional space [135]. Instead of dissimilarities, the experimental measurements can be other various expressions of distances like similarities, probabilities, interaction rates between groups, correlation coefficients, or any other measure of proximity or dissociation [142]. MDS was utilized in a wide range of applications. Particularly, it was used to study the human assessment of surface perceptual attributes, such as color and brightness [166], gloss [167], as well as other properties like haptic perception [148]. A broad review of MDS technique and its utility in different psychological domains is provided by Jaworska et.al [147].

A.2.BASIC CONCEPTS

A.2.1.MDS Space

Measurements used for MDS analysis are known as *proximities* (p_{ij}) given for a pair (i, j) of n *objects* (or *stimuli*). They are collected in a table known as a *proximity matrix.* Then, using a particular *transformation*, they are transformed to approximated distances, or *disparities* $\hat{d}_{ij}$. An MDS algorithm represents the disparities in an m-dimensional configuration, **X,** known as *MDS space*. The distance $d_{ij}(X)$ between points

i and j in the MDS map is approximated by the corresponding disparity $\hat{d}_{ij}\ (X)$ between objects i and j. To be admissible, the transformation should hold a monotone relation between proximities and disparities [168, 169]. This admissibility criterion can be verified using several tools such as *Shepard diagram* [135]. This diagram exhibits the proximities plotted against the corresponding disparities as shown in Figure V-5.

A.2.2.Metric and Ordinal MDS

Metric MDS models use a specific continuous function to transform the proximities to disparities [167]. However, in social sciences, only a qualitative representation based on the rank-order of the proximities is sufficiently meaningful and informative. This is the case of *ordinal* or *non-metric* MDS, introduced first by Shepard [168, 169]. In non-metric MDS, merely the relative ordering of the input proximities should be properly reflected [135]:

$$p_{ij} < p_{kl} \quad Then \quad \hat{d}_{ij} \leq \hat{d}_{kl} \tag{8}$$

In our study, ordinal MDS model with a dissimilarity scale and monotone regression method was employed. One of the major benefits of this model is to avoid horseshoe artifact as explained previously [145, 146]. In the case of tied proximities ($p_{ij} = p_{kl}$), tied disparities ($\hat{d}_{ij} = \hat{d}_{kl}$) were considered to assign a different proximity value for every stimulus pair as recommended previously [135].

A.2.3.Stress Function

MDS algorithms always encounter some empirical errors while mapping disparities into distances. The *stress function* is a statistical parameter used to assess the mismatch between disparities and distances. Ideally, a perfect consistency between the two is reflected by a zero stress value. To measure the goodness of fit in an MDS model, Kruskal normalized squared error and defined *Kruskal stress* or *Stress-1* given below [142]. This is a widely used stress function because of its accuracy and simplicity, especially in qualitative MDS [147]. Since our mar perception analysis is based on qualitative ordinal MDS, *Stress-1* was considered.

$$Stress - 1 = \sqrt{\frac{\sum[\hat{d}_{ij}(X) - d_{ij}(X)]^2}{\sum d_{ij}^2(X)}} \qquad (9)$$

A.2.4.Dimensionality and Scree Plots

The *dimensionality m* of an MDS configuration **X** corresponds to the number of attributes that are significantly affecting the judgment of the subjects. The dimensions of an MDS space are not necessarily similar to the axes of the MDS map. When the dimensionality decreases, the readability of the data and the interpretation of the results are improved, but the stress function increases [136]. Consequently, the optimal dimensionality is the one that gives an interpretable representation with a reasonably low stress [142, 147].

Scree plot is one of the most straightforward techniques used to determine the dimensionality. It is the representation of stress value in terms of the dimension (Figure V-6). If the added dimension has a significant effect on the MDS solution, the stress value decreases considerably. Otherwise, it decreases slightly. Ideally, the scree plot exhibits an "elbow" pointing to the optimal space dimensionality. However, in many cases the stress decreases smoothly and no clear elbow is shown [142-144]. Therefore, other tools can be employed depending on the MDS model, such as the interpretability of the solution itself [136, 138, 142].

A.2.5.Minkowski R-Metrics

In an *m*-dimensional space, the general expression of *Minkowski distance* between two points $x = (x_1, x_2, \dots, x_m)$ and $y = (y_1, y_2, \dots, y_m)$ is given by [168, 169]:

$$d_r(x, y) = \left[\sum_{i=1}^{m} |x_i - y_i|^{r} \right]^{\frac{1}{r}} \qquad r \geq 1 \qquad (10)$$

The distance, and thus the space, is *Euclidian* when $r = 2$. In MDS representation, the distance is typically Euclidian, but does not necessarily have to be so. Besides the change in stress function, Euclidian and non-Euclidian MDS spaces have other major differences. For instance, unlike non-Euclidian distances, Euclidian distance is independent on coordinate axis and geometric rotations between disparities and MDS configuration [142, 170]. To determine the optimal distance, the stress of the best-fitting configuration should be plotted in terms of *r* values (as illustrated in Figure V-4). Optimal *r* value is determined by the least stress value [142]. This parameter was determined in our study to better characterize mar perception MDS space.

A.2.6.Weighted Euclidean Model

Many subjects are usually involved in MDS tests and a *composite MDS matrix* is determined by averaging over all the individual proximity matrices to safeguard the model against noisy individual measurements [136, 167]. However, this fundamentally changes the psychophysical structure of the data [171]. In fact, it artificially increases the amount of data symmetry, inaccurately gives better fit, and shows little information about the importance of the dimensions to each subject. This problem can be overcome by studying subjects separately, which is impractical, or using more sophisticated MDS models.

Weighted Euclidean model is commonly employed to combine data from many subjects and analyze inter-subjects differences in making judgments [131]. In addition to the composite matrix of all subjects, it provides the relative salience, known as *weight* (w_{ik}) of the dimension i to the individual *k*. If this dimension is completely ignored by the individual, then $w_{ik} = 0$. A higher weight means that the subject gave more importance to the dimension. This will be reflected by stretching this dimension in MDS space using a *weighted Euclidian distance* $d_k(x, y)$ instead of the regular distance in equation (3) [137]:

$$d_k(x, y) = \left[\, \sum_{i=1}^{m} w_{ik}\, |x_i - y_i|^{\,2} \,\right]^{\frac{1}{2}} \qquad 0 \le w_{ik} \le 1 \qquad (11)$$

Weighted Euclidian model was considered in our study because it leads to more meaningful interpretation of our results. However, there are other powerful statistical methods that can be considered to study individual MDS configurations such as *Procrustes analysis* [172, 173]. This method consists in finding an arrangement that resembles each individual MDS map by a combination of stretching, translation, reflection and rotation.